1-1-1994

Signal Subspace Techniques for Source Localization with Circular Sensor Arrays

Cherian P. Mathews
Purdue University School of Electrical Engineering

Michael D. Zoltowski
Purdue University School of Electrical Engineering

Signal Subspace Techniques for Source Localization with Circular Sensor Arrays

Cherian P. Mathews
Michael D. Zoltowski

TR-EE 94-3
JANUARY 1994

School of Electrical Engineering
Purdue University
West Lafayette, Indiana 47907-1285

Signal Subspace Techniques for Source Localization with Circular Sensor Arrays [1]

Cherian P. Mathews and Michael D. Zoltowski

School of Electrical Engineering

1285 Electrical Engineering Building

Purdue University

West Lafayette, IN 47907-1285

[1]This work was supported by AFOSR under contract no. F49620-92-5-0198 in conjunction with Wright Laboratories.

TABLE OF CONTENTS

Page

LIST OF TABLES vii

LIST OF FIGURES ix

ABSTRACT xi

1. INTRODUCTION 1

1.1 Introduction 1
1.2 Overview of the Report 3
1.2.1 Features of UCA-RB-MUSIC 4
1.2.2 Features of UCA-ESPRIT 5
1.2.3 Mutual Coupling Effects and the use of Directional Antenna Elements 6
1.2.4 Performance Analysis Results 6
1.3 Literature Review 8
1.3.1 Signal Subspace Techniques for 1D Angle Estimation 8
1.3.2 2D Angle Estimation Algorithms 9
1.3.3 Performance Analysis of Signal Subspace DOA Estimators . . 10
1.4 Organization of the Report 10
1.5 Notational Conventions 11

2. BACKGROUND: ARRAY PROCESSING FOR ARRIVAL ANGLE ESTIMATION 13

2.1 Propagating Plane Waves 13
2.2 Complex Envelope Representation of Band-Pass Signals 15
2.3 Array Manifold Vectors 17
2.4 Array Data Model 20
2.5 Beamforming and Array Patterns 22
2.6 The MUSIC Algorithm 25
2.6.1 Element Space MUSIC 26
2.6.2 Beamspace MUSIC 27
2.6.3 Root-MUSIC 29

Page

3. BEAMFORMING FOR CIRCULAR RING ARRAYS / APERTURES 31

3.1 Uniform Circular Array Geometry **32**
3.2 Cophasal Excitation of Circular Arrays/Apertures **33**
3.2.1 Circular Ring Aperture: Cophasal Excitation **33**
3.2.2 Uniform Circular Array: Cophasal Excitation **34**
3.3 Phase Mode Excitation of Circular Arrays/Apertures **35**
3.3.1 Circular Ring Aperture: Phase Mode Excitation **36**
3.3.2 Uniform Circular Array: Phase Mode Excitation **38**

4. DEVELOPMENT OF UCA-RB-MUSIC AND UCA-ESPRIT . . 41

4.1 Beamforming Matrices for UCA-RB-MUSIC and UCA-ESPRIT . . . 41
4.2 Development of UCA-RB-MUSIC 44
4.2.1 Advantages of UCA-RB-MUSIC 46
4.2.2 UCA-RB-MUSIC: Algorithm Summary 48
4.2.3 Previous Work on Application of ULA Techniques with UCAs 49
4.3 Development of UCA-ESPRIT 50
4.3.1 UCA-ESPRIT: Algorithm Summary 54
4.4 Mutual Coupling Effects 55
4.4.1 Incorporation of Mutual Coupling Effects: Algorithm Summary 57
4.5 Extensions for Directional Elements 57

5. PERFORMANCE ANALYSIS 61

5.1 Performance of MUSIC for 2D Angle Estimation 62
5.2 Performance Analysis of UCA-RB-MUSIC 64
5.3 Performance Analysis of UCA-ESPRIT 68
5.4 The Cramer-Rao Bound 71
5.5 Study of Theoretical Performance for the One and Two Source Cases 72
5.5.1 The Deterministic CRB 73
5.5.2 Performance of Element Space MUSIC 74
5.5.3 Performance of UCA-RB-MUSIC 77
5.5.4 Performance of UCA-ESPRIT 77
5.6 Results of Computer Simulations 79
5.6.1 Simulation Example **1** 81
5.6.2 Simulation Example **2** 82
5.6.3 Simulation Example **3** 85

Page

6. CONCLUSIONS 89

6.1 Summary of Results 89
6.2 Directions for Future Research 91
6.2.1 Adaptation of UCA-RB-MUSIC and UCA-ESPRIT for Filled Circular Arrays 91
6.2.2 Adaptation of UCA-ESPRIT for Concentric Ring Arrays . . . 92

BIBLIOGRAPHY.. 95

APPENDICES

Appendix A: Phase Mode Excitation of Circular Arrays/Apertures: Expressions for Far-Field Patterns 101
Appendix B: Phase Mode Excitation Based Pattern Synthesis for UCAs . 103
Appendix C: Properties of UCA-ESPRIT 105
Appendix D: Study of Theoretical Estimator Performance. 107

LIST OF TABLES

Table Page

3.1 Maximum residual term contribution as a function of N for a UCA with $r = \lambda$ and $M = 6$. **39**

LIST OF FIGURES

Figure		Page
2.1	Spherical coordinate system	**14**
2.2	Band-pass signals: (a) Amplitude spectrum of signal. (b) Amplitude spectrum of pre-envelope. (c) Amplitude spectrum of complex envelope.	**16**
2.3	Arbitrary array geometry	**18**
2.4	Array pattern for a **10** element ULA	**23**
3.1	Uniform circular array geometry.	**32**
3.2	Bessel functions.	**37**
5.1	UCA-ESPRIT eigenvalue error.	**71**
5.2	Theoretical performance of element space MUSIC and UCA-RB-MUSIC as a function of u.	**76**
5.3	Theoretical performance of UCA-ESPRIT for the single source case. . .	**78**
5.4	Performance of UCA-RB-MUSIC and UCA-ESPRIT as a function of ν.	**80**
5.5	Performance of UCA-RB-MUSIC and UCA-ESPRIT as a function of the common source SNR.	**83**
5.6	Plot of UCA-ESPRIT eigenvalues.	**84**
5.7	Performance of UCA-RB-MUSIC and UCA-ESPRIT as a function of the correlation coefficient phase.	**86**

ABSTRACT

Estimating the directions-of-arrival (DOAs) of propagating plane waves is a problem of interest in a variety of applications including radar, mobile communications, sonar, and seismology. The widely studied uniform linear array (ULA) can only provide estimates of source bearings relative to the array axis. A planar array is required if estimates of source azimuth and elevation are required (2D angle estimation). Uniform circular arrays (UCAs) have several properties that make them attractive for 2D angle estimation; e.g., directional patterns synthesized with UCAs can be electronically rotated in the plane of the array without significant change of beam shape. Two signal subspace algorithms for 2D angle estimation with UCAs have been developed. Both algorithms operate in beamspace and employ phase mode excitation based beamformers. The first algorithm, UCA-RB-MUSIC, offers numerous advantages over element space MUSIC. These advantages include reduced computation due to the ability to compute subspace estimates via a real-valued eigenvalue decomposition and the applicability of ULA techniques such as Root-MUSIC. The second algorithm, UCA-ESPRIT, represents a significant advance in the area of 2D angle estimation. It is a novel closed-form algorithm that provides automatically paired source azimuth and elevation angle estimates via the eigenvalues of a matrix. The eigenvalues have the form $\mu = \sin\theta e^{j\phi}$, where θ and ϕ are the elevation and azimuth angles, respectively. UCA-ESPRIT avoids expensive search procedures and is thus superior to existing 2D angle estimation algorithms with respect to computational complexity. The statistical performance of element space MUSIC, UCA-RB-MUSIC, and UCA-ESPRIT has been analyzed. Computer simulations that demonstrate the efficacy of the algorithms and validate the performance analysis results are presented.

1. INTRODUCTION

1.1 Introduction

Array processing deals with the processing of signals carried by propagating wave phenomena. An array of sensors located at different points in space in the field of interest receives the incident signals. The aim of array processing [Hay85] is to extract useful information about the incident field e.g., its direction, speed of propagation, signature, etc. The problem of interest to us is direction-of-arrival (DOA) estimation using an array of sensors . Multiple propagating plane waves that are co-located in frequency are incident on the array, and additive noise corrupts the received signals. The goal is to estimate the azimuth and elevation angles (2D angle estimation) of each source. DOA estimation is a relevant problem in a number of areas including radar, sonar, mobile communications, non-cooperative electronic communication, and direction finding.

Let us briefly look at the use of antenna arrays in mobile communications. The mobile communication channel is characterized by severe multipath fading. Due to multiple propagation paths and the time varying nature of the channel, the signal power received by a given antenna element has a wide dynamic range. The spatial diversity introduced by employing several spatially separated antennas helps combat multipath signal fading. The antenna array can also discriminate between signals co-located in frequency provided they arrive from different directions. Antenna arrays can perform spatial filtering; a signal arriving from a desired direction can be received, while supressing undesired signals from other directions. DOA estimation is an important aspect in mobile communications. The DOAs of the desired and interfering signals (possibly from neighboring cell sites) need to be determined. The

array can then be steered to receive the desired signal, while placing a null in the direction of the interferer.

In this report, we assume that the signals incident on the array are narrow-band, i.e., the signals waveforms do not change appreciably in the time taken for the wavefront to propagate across the aperture of the array. The complex envelope representation is extremely convenient for representing narrow-band signals; the signal received at each antenna element is thus represented by its complex envelope. The 'array response vector' or 'array manifold vector' characterizes the response of the array to a narrow-band plane wave arrival from a given direction. For an array of identical, omnidirectional elements, the array response vector consists of just phase factors corresponding to the time differences between the instants the wavefront reaches the different antenna elements. A simple data model [Hay85] in terms of array response vectors describes the array output in the multiple source/additive noise scenario. This data model, which is all-pervasive in the DOA estimation literature, is the one employed in this report.

The classical method for DOA estimation with sensor arrays is 'beamforming'. Beamforming is essentally a spatial filtering operation that 'steers' the array to a desired direction in space [Pil89]. The output of the beamformer is large when a source arrives from the direction to which the array is steered. Conventional beamforming cannot resolve sources that are spaced less than a beamwidth ('the width of the main-lobe of the spatial filter) apart [Hay85]. Other conventional methods for DOA estimation that have better resolution capabilities than beamforming are Capon's minimum variance method, and linear prediction (see [Pil89]). Algorithms that can resolve sources that are spaced less than a beamwidth apart are called 'superresolution' algorithms. The 'signal subspace' or 'eigenstructure' techniques are superresolution methods that rely on an eigenvalue decomposition (EVD) of the array output covariance matrix. MUSIC (Multiple SIgnal Classification) [Sch86] and ESPRIT (Estimation of Signal Parameters via Rotational Invariance Techniques) [RK89] are among the most well known signal subspace algorithms.

The widely studied uniform linear array (ULA) can only provide estimates of source bearings with respect to the array axis (1D angle estimates). The structure of the ULA (the ULA manifold vectors are Vandermonde) has led to the development of powerful techniques such as Spatial Smoothing [SWK85, PK89a], and Root-MUSIC [Bar83] that are specific to ULAs. A planar array is required if estimates of both azimuth and elevation angle are required. Our interest is in high resolution 2D angle estimation, and we choose to employ the Uniform Circular Array (UCA) configuration. This is because UCAs possess a number of attractive properties as discussed below.

UCAs provide 360° azimuthal coverage, and also provide information on source elevation angles. In addition, directional patterns synthesized with UCAs can be electronically rotated in the plane of the array without significant change of beam shape. ULAs in contrast provide only 180° coverage, and beams formed with ULAs broaden as the array is steered away from boresight. Phase mode excitation of UCAs, which essentially is Fourier analysis of the array excitation function, was studied by researchers in the early 1960s [THN61, LCD67]. This theory led to a powerful pattern synthesis technique for UCAs [Dav83]. Davies [Dav65] showed how the simple phasing techniques normally associated with ULAs (Butler beamforming matrices) could be used to provide the necessary phasing for pattern rotation with UCAs. These attractive features led to the development of experimental systems that employed phase mode excitation for pattern synthesis with UCAs [Dav65, GD83]. These systems however employed the beamforming principle to obtain DOA estimates; as mentioned earlier, beamforming cannot provide superresolution.

1.2 Overview of the Report

This report presents the development and statistical performance analysis of two superresolution algorithms [MZ93a, MZ93b] for DOA estimation with UCAs. Both algorithms employ phase mode excitation based beamforming in conjunction with subspace techniques to provide high resolution DOA estimates. The first algorithm,

UCA-RB (Real-Beamspace) MUSIC, is a beamspace MUSIC algorithm that offers many advantages over element space MUSIC. The second algorithm is named UCA-ESPRIT because the steps involved in the algorithm are similar to those of TLS-ESPRIT [RK89]. We note that the applicability of the ESPRIT principle in conjunction with rotationally invariant arrays (such as UCAs) was studied in [Swi92]. It was shown that such techniques cannot provide unique DOA estimates when more than one source is present. Although this is true in element space, the phase mode excitation based transformation from element space to beamspace induces a beamspace manifold whose structure can be exploited to develop an ESPRIT like algorithm, UCA-ESPRIT.

1.2.1 Features of UCA-RB-MUSIC

The UCA-RB-MUSIC algorithm offers numerous advantages over element space MUSIC. These advantages include the ability to compute subspace estimates via real-valued eigenvalue decompositions (EVDs), improved estimator performance in correlated source scenarios due to an inherent Forward/Backward (FB) average [PK89a], and the ability to employ Root-MUSIC to obtain azimuth estimates of sources at a given elevation. UCA-RB-MUSIC requires a two-dimensional spectral search to obtain the DOA estimates. However, the computational complexity is lower than for element space MUSIC, since samples of the 2D beamspace MUSIC spectrum corresponding to a given elevation can be obtained via an FFT. In contrast, element space MUSIC requires a complex-valued EVD for computing subspace estimates, and ULA techniques such as Root-MUSIC cannot be employed. Averaging similar to FB averaging can be performed in element space with UCAs, but only when the number of array elements, N, is even. It was shown in [SN91] that beamspace MUSIC estimators can never outperform the corresponding element space MUSIC estimators. While this is generally true, UCA-RB-MUSIC can outperform element space MUSIC in correlated source scenarios when N is odd. This is due to the decorrelating effect of the FB average inherent in UCA-RB-MUSIC, but not available in element space

for odd N. Previous work on the application of ULA techniques with UCAs include that of Tewfik and Hong [TH92], and Friedlander and Weiss [FW92]. Comparisons between their approaches and UCA-RB-MUSIC are made in Section 4.2.

1.2.2 Features of UCA-ESPRIT

UCA-ESPRIT is a novel algorithm that represents a significant advance in the area of 2D angle estimation. It is a closed-form algorithm that provides automatically paired azimuth and elevation estimates for each source. The term 'closed-form' connotes that the algorithm dispenses with the search/optimization procedures that are characteristic of one class of 2D angle estimation algorithms. MUSIC, for example, requires a two-dimensional spectral search to obtain the DOA estimates. Maximum likelihood approaches [CS91] require even more expensive multidimensional search procedures. The other class of 2D angle estimation algorithms, ESPRIT based algorithms, [RK89, ZS89] require arrays that contain subarrays possessing displacement invariances in two dimensions. These algorithms do not require search procedures, and provide closed-form estimates of source direction cosines with respect to each displacement axis. However, they require a pairing procedure (usually ad-hoc) to properly associate the independently obtained direction cosine estimates. The ESPRIT based algorithm for arrays with regular geometries described in [SK93] does provide automatically paired angle estimates; the algorithm however requires a multidimensional search for optimality.

Unlike the existing 2D angle estimation algorithms, UCA-ESPRIT provides automatically paired source azimuth and elevation estimates via the eigenvalues of a matrix (that is derived from the least squares solution to an overdetermined system of equations). The eigenvalues have the form $\mu_i = \sin\theta_i e^{j\phi_i}$, where 0; and ϕ_i are respectively the elevation and azimuth angles of the ith source. Note also that $\mu_i = u_i + \text{jv};$, where u; and v; are respectively the direction cosines with respect to the x and y axes. UCA-ESPRIT is clearly superior to the existing 2D angle estimation algorithms in terms of computational complexity. Another factor that that reduces

the computational burden of UCA-ESPRIT is that the algorithm can be implemented with just real-valued EVDs. It should be pointed out that the UCA-RB-MUSIC estimator has a lower variance than the UCA-ESPRIT estimator. For improved estimator performance, the azimuth and elevation estimates from UCA-ESPRIT can be used as starting points for localized Newton searches of the two-dimensional UCA-RB-MUSIC spectrum.

1.2.3 Mutual Coupling Effects and the use of Directional Antenna Elements

The effects of mutual coupling on the structure of the UCA element space manifold are studied. It is shown that the general structure of the original beamspace manifold (in the absence of mutual coupling) is retained even when mutual coupling effects apply. The only difference is the introduction of gain and phase factors in the original beamspace manifold. Consequently, minor modifications enable UCA-RB-MUSIC and UCA-ESPRIT to cope with mutual coupling effects. Acounting for mutual coupling effects is much simpler with UCAs than with other array configurations.

The effects of employing directional antenna elements in the UCA are also investigated. Both UCA-RB-MUSIC and UCA-ESPRIT are applicable if the individual element patterns are omnidirectional in azimuth. UCA-ESPRIT cannot be employed if this condition on element patterns is not met. However, a beamspace algorithm possessing many of the features of UCA-RB-MUSIC is still applicable.

1.2.4 Performance Analysis Results

Asymptotic expressions for the variances/covariances of the MUSIC estimator for the 1D angle estimation problem are available in [SN89]. The MUSIC spectrum in the 2D angle estimation problem is a function of two variables (azimuth and elevation), and results on the performance of MUSIC in the 2D scenario are not available in the literature. Such asymptotic results (applicable to arbitrary array configurations)

are derived herein; the derivation is along the lines of the work in [SN89]. Asymptotic expressions for the variances/covariances of the UCA-RB-MUSIC estimators are also derived. UCA-RB-MUSIC works with real-valued signal and noise subspace eigenvectors. In contrast, the signal and noise subspace eigenvectors corresponding to element space MUSIC are complex-valued. The analysis of UCA-RB-MUSIC differs from that of element space MUSIC in that the statistics of the eigenvectors of the sample covariance matrix are different. The asymptotic performance of the UCA-ESPRIT algorithm is also analyzed. The analysis employs techniques used in [RH89a] to study the performance of the ESPRIT algorithm for 1D angle estimation. All the performance analysis results are verified by computer simulations.

The asymptotic behavior of the direction cosine estimators corresponding to element space MUSIC, UCA-RB-MUSIC, and the Cramer-Rao bound (CRB) is investigated in some detail for the one and two source scenarios. Closed-form expressions are obtained for the element space MUSIC direction cosine estimator variances in these scenarios. The performance study reveals that both the element space MUSIC estimator variances and the CRB are constants (independent of the DOA) in the single source case. The UCA thus favors sources from all directions equally. In the two source case, the DOA dependence of the element space MUSIC estimator variance and the CRB is only through the distance between the source locations, and the orientation of the line joining the source locations in direction cosine space. In other words, the direction cosine estimator variances depend on the source DOAs only through the position of one source relative to the other. The above properties are due to the circular symmetry of the UCA; arbitrary array geometries do not in general possess such properties. Although closed-form expressions for the UCA-RB-MUSIC estimator variances cannot be obtained, their behavior is shown to closely follow that of element space MUSIC and the CRB.

1.3 Literature Review

References to pertinent articles in the literature were made in the overview of Section 1.2. This section is devoted to a brief survey of signal subspace techniques, previous work on 2D angle estimation, and work on performance analysis.

1.3.1 Signal Subspace Techniques for 1D Angle Estimation

As discussed in Section 1.1, signal subspace or eigenvector techniques for DOA estimation rely on an EVD of the array output covariance matrix. The eigenvectors are partitioned into the 'signal space' and 'noise space' eigenvectors. Subspace techniques exploit the properties of the signal and noise subspaces to extract information on the source DOAs. Eigenvector methods were first employed by Pisarenko [Pis73] to retrieve harmonics embedded in a time series. There has been subsequent interest in applying eigenvector techniques to time series analysis (see [KT82] and the references therein). The MUSIC algorithm [Sch86] for DOA estimation with antenna arrays was developed by Schmidt in the late 1970s. This work generated a lot of interest in subspace techniques for DOA estimation, and a number of modifications to MUSIC such as the minimum-norm approach [KT83], and Root-MUSIC [Bar83] were proposed. Beamformer preprocessing was proposed in [BK84] as a modification of MUSIC for sector-wise searches for sources. A lot of work on such Beamspace MUSIC algorithms has since been done (see [ZKS93] and accompanying references). All the MUSIC based approaches (except for Root-MUSIC) require a search for peaks in the MUSIC spectrum. When Root-MUSIC is employed with a ULA, the spectral search is replaced by a polynomial rooting procedure.

The ESPRIT approach that was initially proposed by Paulraj et al. [PRK86] requires an array of matched doublets, whose elements are translationlly separated by a constant displacement vector. A refinement of the algorithm, TLS-ESPRIT [RK89], avoids some of the numerical problems of the original approach. ESPRIT provides closed-form estimates of source DOAs via the eigenvalues of a matrix that is essentially a subspace rotation operator. ESPRIT thus avoids the search procedures

associated with MUSIC. Other matrix pencil based approaches based on the ESPRIT ideas include PRO-ESPRIT [ZS89] and the direct matrix pencil algorithm [HS90].

The weighted subspace fitting algorithm [VO91] is another signal subspace technique for DOA estimation. The algorithm is optimal (minimum variance), but requires an expensive multidimensional search procedure. It is interesting to note that TLS-ESPRIT and even the deterministic maximum likelihood algorithm [SN89] fall into the subspace fitting framework.

1.3.2 2D Angle Estimation Algorithms

Both MUSIC and ESPRIT can be employed for 2D angle estimation. MUSIC can be employed with arbitrary array geometries, but requires a two-dimensional spectral search. Arrays with displacement invariances in two dimensions are required when ESPRIT is employed for 2D angle estimation. ESPRIT applied independently to the two subarray pairs provides independent estimates of source direction cosines with respect to the two displacement axes (see [ZS89]). A procedure (which is usually ad-hoc) for pairing the independently obtained direction cosine estimates is thus required. There are further complications if two of the sources share a common bearing with respect to one of the displacement axes. The algorithm [SK93] applicable to certain arrays with regular geometries provides automatically paired direction cosine estimates. However, it requires a multidimensional search for optimality (a suboptimal closed-form procedure for obtaining DOA estimates was presented). The algorithm for rectangular arrays [Hua92] can cope with the case where two sources share a common spatial frequency component; however, the algorithm still requires a pairing procedure. Several other techniques proposed for rectangular arrays include a state-space approach [KAR83], a matrix approximation approach [SK88], and a maximum likelihood approach [CS91]. All these approaches fail if two sources share a common spatial frequency component. In the light of this review of 2D angle estimation algorithms, it is clear that UCA-ESPRIT is unique in that it provides automatically paired 2D angle estimates via a closed-form procedure.

1.3.3 Performance Analysis of Signal Subspace DOA Estimators

Asymptotic (large number of snapshots of array data) expressions for the variances of the MUSIC [SN89], ESPRIT [RH89a], and TLS-ESPRIT [OVK91] estimators are available in the literature. The statistics of the eigenvectors of the array output covariance matrix (which is complex Wishart distributed when the noise is complex Gaussian) are required for the analysis. These eigenvector statistics were obtained in [Gup65, Bri81, JF85, KB86] for the complex Gaussian noise case. The Forward/Backward (FB) spatial smoothing scheme [PK89a] enables subspace techniques for ULAs to cope with coherent signal arrivals. The performance of the MUSIC algorithm with spatial smoothing was analyzed by Pillai and Kwon [PK89b]. Zoltowski and Kautz [ZKS93] showed that a real-valued EVD is sufficient when operating in beamspace with a ULA (employing centro-Hermitian beamformers). They also showed that working with the real part of the beamspace covariance matrix is equivalent to performing a FB average. Based on the work in [PK89b], they derived the statistics of the corresponding real-valued eigenvectors [ZK92]. These statistics are employed here to analyze the UCA-RB-MUSIC algorithm.

Li and Vaccaro employed perturbation analysis to analyze the performance of MUSIC and ESPRIT [LV90]. They obtained estimator variance expressions for the finite sample case, under the assumption of high SNR (signal to noise ratio). Expressions for the Cramer-Rao bound on estimator variances/covariances for the 1D angle estimation problem have been derived in [SN89] and [SN90] for both the deterministic and stochastic signal models. The deterministic CRB derivation was extended in [YB92] for the two (or higher) dimensional case.

1.4 Organization of the Report

The organization of this report is as follows: Chapter 2 provides some of the background material on array processing for DOA estimation. Chapter 3 introduces beamforming techniques for circular apertures and arrays; cophasal beamforming and phase mode excitation based beamforming are studied. The UCA-RB-MUSIC

and UCA-ESPRIT algorithms are developed in Chapter 4. Chapter 5 addresses the performance analysis of the algorithms. Results of computer simulations of UCA-RB-MUSIC and UCA-ESPRIT are also presented in this chapter. Finally, Chapter 6 provides a summary of the results, and discusses directions for future research.

1.5 Notational Conventions

The notational conventions employed in this report are as follows: bold face lower case letters are used to denote column vectors, and bold face upper case letters denote matrices. An asterisk is used to denote the complex conjugate operation e.g., $\mathbf{A}^*$. The transpose and Hermitian transpose operations are respectively denoted by superscripts T and H e.g., G^T, G^H. Hats are used to denote estimated values of quantities e.g., $\hat{\mathbf{S}}$. The same symbol is used to denote similar quantities in element space and beamspace; the element space quantities are distinguished by underbars e.g., $\mathbf{S}$ and $\underline{\mathbf{S}}$ respectively span the beamspace and element space signal subspaces. Other notational conventions employed will be specified as and when necessary.

2. BACKGROUND: ARRAY PROCESSING FOR ARRIVAL ANGLE ESTIMATION

This chapter presents background material that is relevant for DOA estimation with antenna arrays. The signals incident on the antenna array (from different directions, but co-located in frequency) are assumed to be narrow-band propagating plane waves. Section 2.1 provides a mathematical description for propagating plane waves. The array output signals are represented in terms of their complex envelopes. Section 2.2 thus reviews the complex envelope representation of band-pass signals. The concept of the array response vector (or manifold vector), is elucidated in Section 2.3. The array manifold vector provides a description of the array output when a narrow-band signal from a given direction impinges on it. The data model most commonly used to model the array output in a narrow-band, multiple source scenario is introduced in Section 2.4. Section 2.5 discusses the beamforming operation, and the concept of antenna array patterns. Finally, Section 2.6 reviews the popular MUSIC algorithm for estimating the arrival directions of multiple sources. The Beamspace MUSIC and Root-MUSIC variations of MUSIC are also discussed.

2.1 Propagating Plane Waves

A plane wave propagating in space can be represented by the following equation:

$$s(t,\vec{p}) = g\left(t - \frac{\hat{v}\cdot\vec{p}}{v}\right), \qquad [2.1]$$

where $s(t,\vec{p})$ is the signal amplitude at time t at the location $\vec{p}$ (position vector), g is the function specifying the shape of the wave, v is the speed of propagation, and $\hat{v}$ is the unit vector in the direction of propagation. At any given time, the signal amplitude is constant on any plane perpendicular to the direction of propagation.

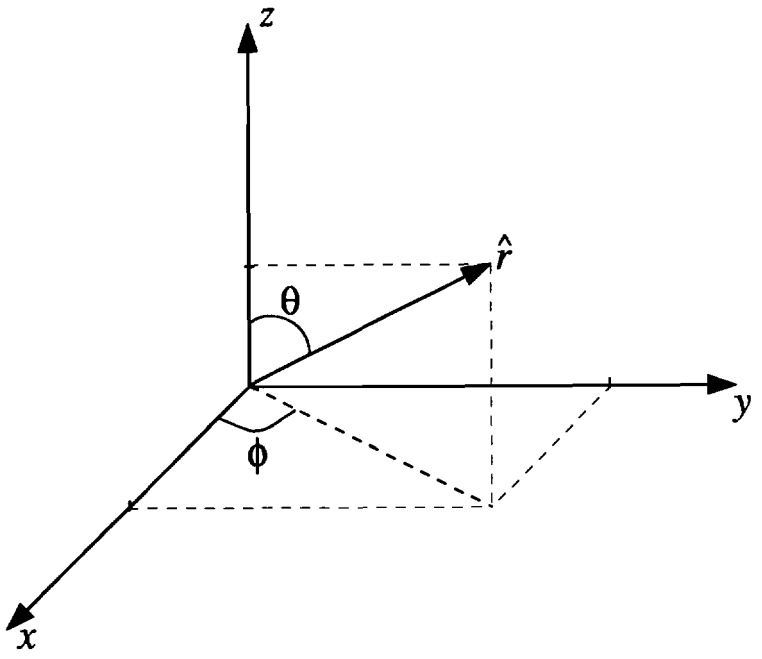

Figure 2.1 Spherical coordinate system

The points in space on such a plane are described by the equation $\hat{v} \cdot \vec{p} = k$, where k is a constant. Let $\hat{r} = -6$ be the vector specifying the DOA of the plane wave. Equation 2.1 can then be rewritten as

$$s(t, \vec{p}) = g\left(t + \frac{\hat{r} \cdot \vec{p}}{v}\right). \qquad [2.2]$$

The spherical coordinate system (r, θ, ϕ) depicted in Figure 2.1 will be employed to specify the DOA of a signal. The elevation and azimuth angles of a source arriving from the direction $\hat{r}$ are θ and ϕ, respectively. The DOA vector $\hat{r}$ can also be expressed in cartesian coordinates as follows:

$$\hat{r} = (u, v, w) = (\sin\theta\cos\phi, \sin\theta\sin\phi, \cos\theta), \qquad [2.3]$$

where u,v, and w are respectively the direction cosines with respect to the x, y, and z axes.

Harmonic Plane Waves

The harmonic wave whose shape is specified by $g(t) = A\cos(2\pi f t + a)$, and propagating at the speed of light c is of interest in radar systems. The wavelength λ and frequency f of the wave are related by the equation $c = f\lambda$. Following Equation 2.2, such a wave arriving from the direction $\hat{r}$ is described by

$$s(t, \vec{p}) = A\cos\left[2\pi f\left(t + \frac{\hat{r}\cdot\vec{p}}{c}\right) + \alpha\right] = A\cos[2\pi f t + k_0\hat{r}\cdot\vec{p} + \alpha], \qquad [2.4]$$

where $k_0 = 2\pi/\lambda$ is the wavenumber. The quantity $k_0\hat{r}\cdot\vec{p}$ is the phase shift in radians between the signal received at the origin and that at locations on the plane $\hat{r}\,.\,\vec{p} =$ constant. The components of the vector $k_0\hat{r}$ are the spatial frequencies of the signal in the x, y, and z directions.

2.2 Complex Envelope Representation of Band-Pass Signals

The complex envelope representation of is a very useful tool for the analysis of band-pass systems. The complex envelope retains all the information content of a band-pass signal, but is itself a low-pass signal. The representation of the antenna element outputs in terms of complex envelopes turns out to be very useful for the narrow-band DOA estimation problem. The following discussion of the complex envelope representation is brief, and further details may be found in [Hay83].

Let $g(t)$ be a real-valued band-pass signal with carrier frequency f_c and bandwidth 2W. For the purposes of illustration, let the amplitude spectrum of $g(t)$ be as shown in Figure 2.2a. The pre-envelope of the signal $g(t)$ is a complex-valued function $g_+(t)$ defined by

$$g_+(t) = g(t) + j\hat{g}(t),$$

where $\hat{g}(t)$ is the Hilbert transform of $g(t)$. The complex envelope $\tilde{g}(t)$ of the signal $g(t)$ is defined as follows:

$$\tilde{g}(t) = g_+(t)\exp(-j2\pi f_c t).$$

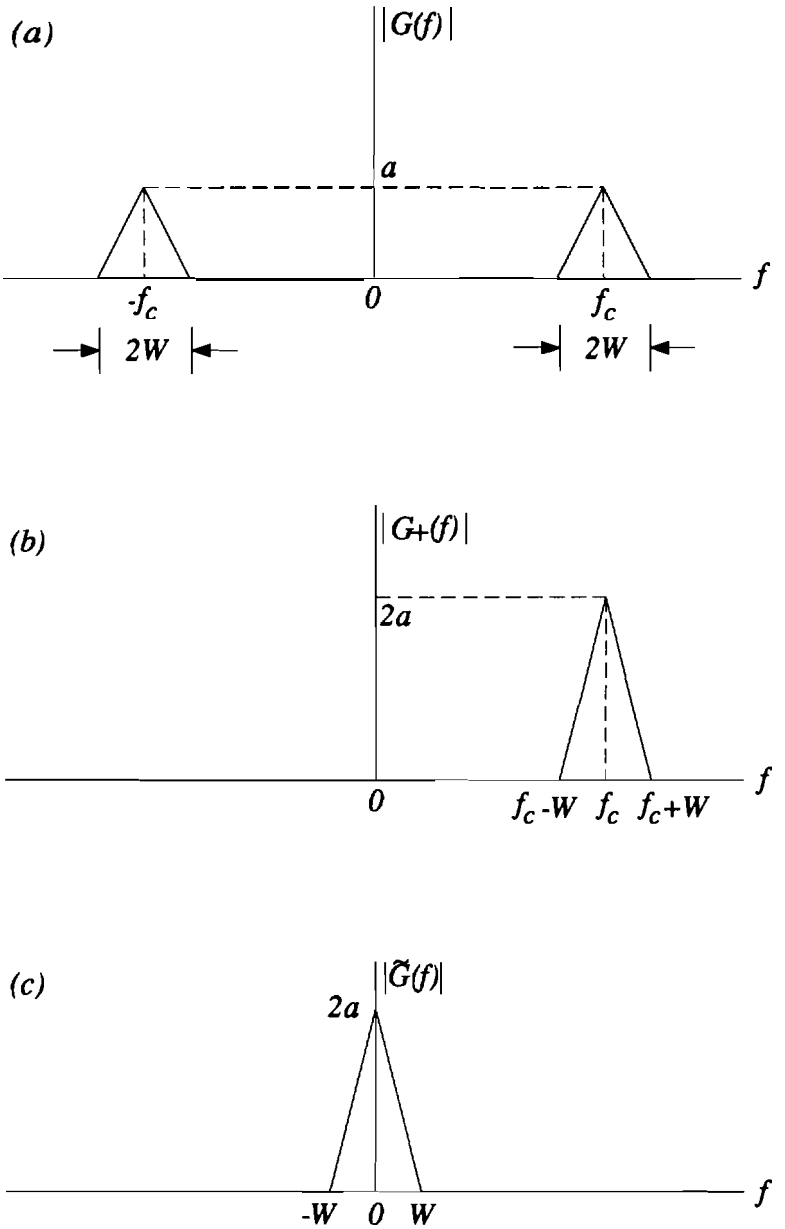

Figure 2.2 Band-pass signals: (a) Amplitude spectrum of signal. (b) Amplitude spectrum of pre-envelope. (c) Amplitude spectrum of complex envelope.

The complex envelope $\tilde{g}(t)$ is a low-pass signal whose spectrum is limited to the frequency band $-W \leq \mathrm{f} \leq \mathrm{W}$. The amplitude spectra of $g_+(t)$ and $\tilde{g}(t)$ are depicted in Figures 2.2b and 2.2c, respectively. The signal $g(t)$ may be expessed in terms of the complex envelope $\tilde{g}(t)$ as follows:

$$g(t) = \mathrm{Re}\,[\tilde{g}(t)\exp(j2\pi f_c t)] \qquad [2.5]$$

The complex envelope $\tilde{g}(t)$ can also be expressed in the following form:

$$\tilde{g}(t) = a(t)\exp[j\phi(t)], \qquad [2.6]$$

where $a(t)$ and $\phi(t)$ are both real-valued, low-pass functions. The corresponding representation for the narrow-band signal $g(t)$ is

$$g(t) = a(t)\cos[2\pi f_c t + \phi(t)]. \qquad [2.7]$$

2.3 Array Manifold Vectors

The array manifold vector (or array response vector) for an array of N elements corresponding to a narrow-band signal arrival from the direction $\hat{r}$ is an N vector **a(?).** It provides a convenient description of the signals received by the array, and is valid only for narrow-band signals. Consider an antenna array that consists of N identical, isotropic elements. The array geometry is depicted in Figure 2.3. The array elements are numbered from 0 to N – 1, and the position vector $\vec{p}_n$ specifies the location of element n. The origin of the coordinate system is chosen to coincide with the location of element 0, and hence $\vec{p}_0 = \vec{0}$. The signals received by the antenna elements are represented by their complex envelopes: $\tilde{g}_n(\mathrm{t})$ represents the output of element n at time t. The array output at time t is given by the vector

$$\mathbf{x}(t) = [\tilde{g}_0(t), \tilde{g}_1(t), \cdots, \tilde{g}_{N-1}(t)]^T. \qquad [2.8]$$

We proceed to obtain the array manifold vector corresponding to a plane wave arrival from the direction $\hat{r}$. The case of a harmonic plane wave is first considered. We then show that the same manifold vector can be used to describe the array output when the incident signal is a narrow-band plane wave.

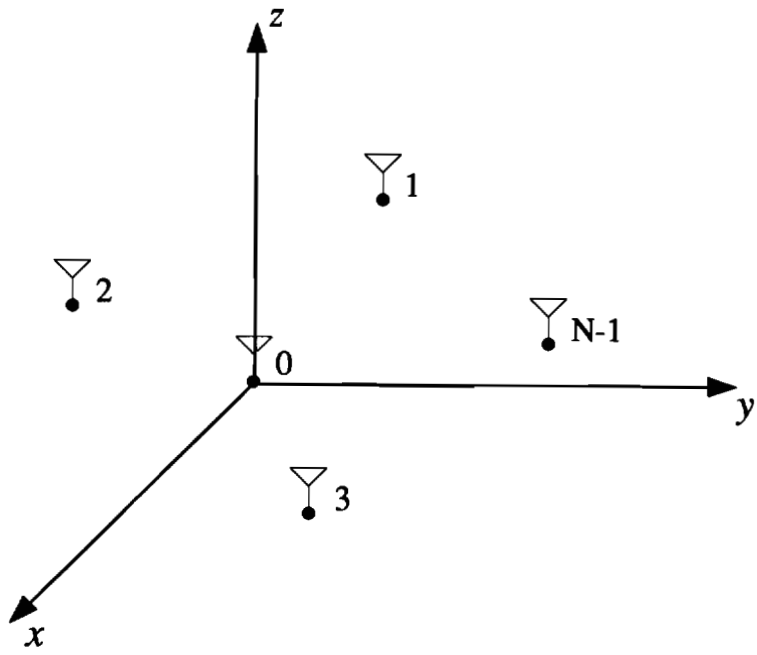

Figure 2.3 Arbitrary array geometry

Harmonic Plane Waves

The signal received by element 0 (located at the origin) is the harmonic signal $g_0(t) = \mathrm{A}\cos(2\pi f_c t + \mathrm{a})$. The signal received at element n is a time delayed version of $g_0(t)$. Since time delays translate into phase delays for harmonic signals, we have (following Equation 2.4) $g_n(t) = \mathrm{A}\cos(2\pi f_c t + k_0\hat{r}\,.\,\vec{p}_n + \mathrm{a})$. The complex envelope of $g_n(t)$ is

$$\tilde{g}_n(t) = A\exp(j\alpha)\exp(jk_0\hat{r}\cdot\vec{p}_n) = \tilde{g}_0(t)\exp(jk_0\hat{r}\cdot\vec{p}_n), \qquad [2.9]$$

where $\tilde{g}_0(t)$ is the complex envelope of the signal received at element 0. From Equations 2.8 and 2.9, we see that the array output at time t can be expressed as follows:

$$\mathbf{x}(t) = \tilde{g}_0(t)\underline{\mathbf{a}}(\hat{r}), \text{ where} \qquad [2.10]$$

$$\underline{\mathbf{a}}(\hat{r}) = \begin{bmatrix} \exp(jk_0\hat{r}\cdot\vec{p}_0) \\ \exp(jk_0\hat{r}\cdot\vec{p}_1) \\ \vdots \\ \exp(jk_0\hat{r}\cdot\vec{p}_{N-1}) \end{bmatrix} \qquad [2.11]$$

is the array manifold vector corresponding to the direction $\hat{r}$. Component n of $\underline{\mathbf{a}}(\hat{r})$ is just the phase shift between the signals received at element n and at the origin at any given time instant. Equation 2.10 expresses the array output in terms of the signal $\tilde{g}_0(t)$ received at the reference element (element 0), and the array response vector $\underline{\mathbf{a}}(\hat{r})$. If the origin of the coordinates does not coincide with an element location, the array output can be expressed as $\mathbf{x}(t) = \tilde{g}_{org}(t)\underline{\mathbf{a}}(\hat{r})$, where $\tilde{g}_{org}(t)$ is the complex envelope of the signal received at the origin at time t. If the array elements were not omnidirectional but had a complex response pattern $h(\hat{r})$, the array manifold vector would be modified as follows: $\underline{\mathbf{a}}_d(\hat{r}) = h(\hat{r})\underline{\mathbf{a}}(\hat{r})$.

Narrow-Band Plane Waves

In practice, the signals received by the antenna elements are not pure sine waves, but are pulsed sine waves with some target modulation. The spectrum of the received signal is however still concentrated in a small frequency band around the carrier frequency f_c. Assume that the spectrum is confined to the band $f_c \pm$ W as in Figure 2.2a. If the maximum frequency deviation W from f_c is 'small', the array manifold vector can still be represented by phase differences corresponding to those for a harmonic signal with frequency f_c. The definition of 'small' however depends on the center frequency f_c and the aperture (maximum distance between any two elements) of the array.

Assume that the two array elements that are furthest apart are elements 0 and n. Since the incident signals are band-pass, the signal received at element 0 can be expressed as follows (see Equation 2.7):

$$g_0(t) = a(t)\cos[2\pi f_c t + \phi(t)]. \qquad [2.12]$$

The complex envelope of this signal is $\tilde{g}_0(t) = a(t)\exp[j\phi(t)]$. The signal received at element n is a time delayed version of $g_0(t)$. Following Equation 2.2, we have $g_n(t) = g_0(t + \tau)$, where $\tau = \hat{r} \cdot \vec{p}_n/c$ is the appropriate time delay. Using the fact that $k_0 = 2\pi f_c/c$, we obtain $g_n(t) = a(t + \tau)\cos[2\pi f_c t + k_0 \hat{r} \cdot \vec{p}_n + \phi(t + \tau)]$. The

complex envelope of this signal is

$$\begin{aligned} \tilde{g}_n(t) &= a(t+\tau)\exp[j\phi(t+\tau)]\exp(jk_0\hat{r}\cdot\vec{p}_n) \\ &= \tilde{g}_0(t+\tau)\exp(jk_0\hat{r}\cdot\vec{p}_n). \end{aligned} \quad [2.13]$$

Now if $\tilde{g}_0(t+\tau) \approx \tilde{g}_0(t)$, we have $\tilde{g}_n(t) = \tilde{g}_0(t)\exp(jk_0\hat{r}\cdot\vec{p}_n)$. This equation is identical in form to Equation 2.9, and the array output can hence be written as

$$\mathbf{x}(t) = \tilde{g}_0(t)\underline{\mathbf{a}}(\hat{r}), \quad [2.14]$$

as in Equation 2.10. The components of the array manifold vector $\underline{\mathbf{a}}(\hat{r})$ in the above equation are the phase factors corresponding to the center frequency f_c.

The signals received by the array are narrow-band if $\tilde{g}_0(t+\tau_{\max}) \approx \tilde{g}_0(t)$, where $\tau_{\max}$ is the maximum time taken for a wavefront to propagate across the entire array. From the definition of τ, we see that $\tau_{\max} = \|\vec{p}_n\|/c = d_{\max}/c$, where $d_{\max}$ is the maximum distance between any two array elements. Now, $\tilde{g}_0(t)$ is a low-pass signal with maximum frequency component W. If W is such that $\tau_{\max} \ll 1/\mathrm{W}$, the signal $\tilde{g}_0(t)$ cannot change appreciably in time $\tau_{\max}$, and the received signals are narrow-band.

To illustrate via an example, consider the case of a 10 element uniform linear array (ULA) operating at a center frequency $f_c = 2$ GHz ($\lambda = 0.15$m). The elements are spaced half a wavelength apart to avoid grating lobes. We have $d_{\max} = 9\lambda/2 = 0.675$m, and $\tau_{\max} = 2.25$ns. We want to find limits on the maximum frequency deviation W for which the wave can be considered to be narrow-band. In the time period $\tau_{\max}$, the maximum fractional change of a sinusoid (change in signal level / signal amplitude) is $2\pi W\tau_{\max}$. Limiting the maximum fractional change to 1% yields W = 0.71 MHz. The received signal would thus be narrow-band if its spectrum was confined to the band $f_c \pm 0.71$ Mhz.

2.4 Array Data Model

The standard model employed to describe the antenna array output in a multiple source, narrowband scenario is presented in this section. The array has N identical

elements at locations $\vec{p}_n$, n = 0, 1, . . . , N – 1 with reference to an appropriately positioned cartesian coordinate system. Assume that d < N point sources are present in the far-field of the array, and that the source DOAs are $\hat{r}_k$, k = 1, 2, . . . , d. Narrowband plane waves with common center frequency f_c emanate from each of the sources and impinge on the array. Addititve noise corrupts the signals received by the antenna elements. The received signals (in complex envelope form) are sampled at time instants t = 1, 2, . . . , L, yielding L snapshots of array data. The snapshot vector at time t is modeled as follows:

$$\mathbf{x}(t) = \sum_{k=1}^{d} s_k(t)\underline{\mathbf{a}}(\hat{r}_k) + \mathbf{n}(t) \qquad t = 1, 2, \ldots, L, \qquad [2.15]$$

where $\underline{\mathbf{a}}(\hat{r}_k)$, defined in Equation 2.11, is the array manifold vector corresponding to the kth source. The signal DOAs do not change during the observation period, and the manifold vectors thus remain constant over all the snapshots. In the model, $s_k(t)$ is the complex envelope of the kth signal at the reference element (the origin). The vector $\mathbf{n}(t)$ is formed by stacking the complex envelopes of the noise at the array elements. Equation 2.15 can be expressed in matrix form as follows:

$$\mathbf{x}(t) = \underline{\mathbf{A}}\mathbf{s}(t) + \mathbf{n}(t) \qquad t = 1, 2, \ldots, L, \qquad [2.16]$$

where $\underline{\mathbf{A}} = [\underline{\mathbf{a}}(\hat{r}_1), \ldots, \underline{\mathbf{a}}(\hat{r}_d)]$ is the DOA matrix, and $\mathbf{s}(t) = [s_1(t), s_2(t), \cdots, s_d(t)]^T$ is the vector of signal complex envelopes.

The signals and the noises are assumed to be stationary, zero mean, uncorrelated random processes. The noise covariance matrix is $\mathbf{R}_n = E[n(t)n^H(t)]$, and the source covariance matrix is $P = E[s(t)s^H(t)]$. The array output covariance matrix $\underline{\mathbf{R}} = E[x(t)x^H(t)]$ thus has the form

$$\underline{\mathbf{R}} = \underline{\mathbf{A}}\mathbf{P}\underline{\mathbf{A}}^H + \mathbf{R}_n. \qquad [2.17]$$

The noise vector is frequently assumed to be spatially white, (uncorrelated from sensor to sensor) with variance σ. The noise covariance matrix is thus $\mathbf{R}_n = \sigma\mathbf{I}$. The source covariance matrix P has full rank d provided the incident signals are non-coherent.

2.5 Beamforming and Array Patterns

Beamforming is a spatial filtering operation that is the basis for the conventional method of DOA estimation with antenna arrays. A beam is formed by weighting and summing the array outputs. Let $\mathbf{x}(t)$ be the array output at time t, and $\mathbf{w}^H = [w_0, w_1, \ldots, w_{N-1}]$ be the beamforming weight vector. The beam output is

$$y(t) = \mathbf{w}^H \mathbf{x}(t). \qquad [2.18]$$

The response of the array to a source in the direction $\hat{r}$ is given by the array manifold vector $\underline{\mathbf{a}}(\hat{r})$. The elements of the manifold vector are just the phase shifts incurred by the wavefront in propagating from element to element. The standard beamforming procedure is to choose the beamformer weights such that these phase shifts are compensated for. Such a beamformer is called a cophasal beamformer; the weight vector required to 'steer' the array to the direction $\hat{r}_s$ is just $\underline{\mathbf{a}}^H(\hat{r}_s)$. From Equation **2.18,** we see that the beam output is large when a source arrives from the direction $\hat{r}_s$, since all the signals sum up in phase. Signals arriving from other directions are attenuated by the beamformer. The beamformer thus performs spatial filtering.

Given a certain weight vector $\boldsymbol{w}^H$, the antenna array pattern specifies the response of the beamformer to a source arriving from the arbitrary direction $\boldsymbol{i}$. The array pattern thus specifies the spatial frequency response of the antenna array for a given set of beamformer weights. The array pattern depends only on the weight vector $\boldsymbol{w}^H$ and the relative positions of the array elements. The array pattern is independent of the type of elements employed. For an N element array with elements located at $\vec{p}_0, \vec{p}_1, \ldots, \vec{p}_{N-1}$, the array pattern is

$$f(i) = \mathbf{w}^H \underline{\mathbf{a}}(\hat{r}) = \sum_{n=0}^{N-1} w_n \exp(jk_0 \hat{r} \cdot \vec{p}_n). \qquad [2.19]$$

The array pattern $f(i)$ is in general complex-valued. Its absolute value $|f(i)|$ is typically an oscillatory function with a main-lobe and side-lobes. The main-lobe represents the pass-band of the beamformer; sources from directions $\hat{r}$ in the main-lobe region are passed without much attenuation. It is desirable that the array pattern

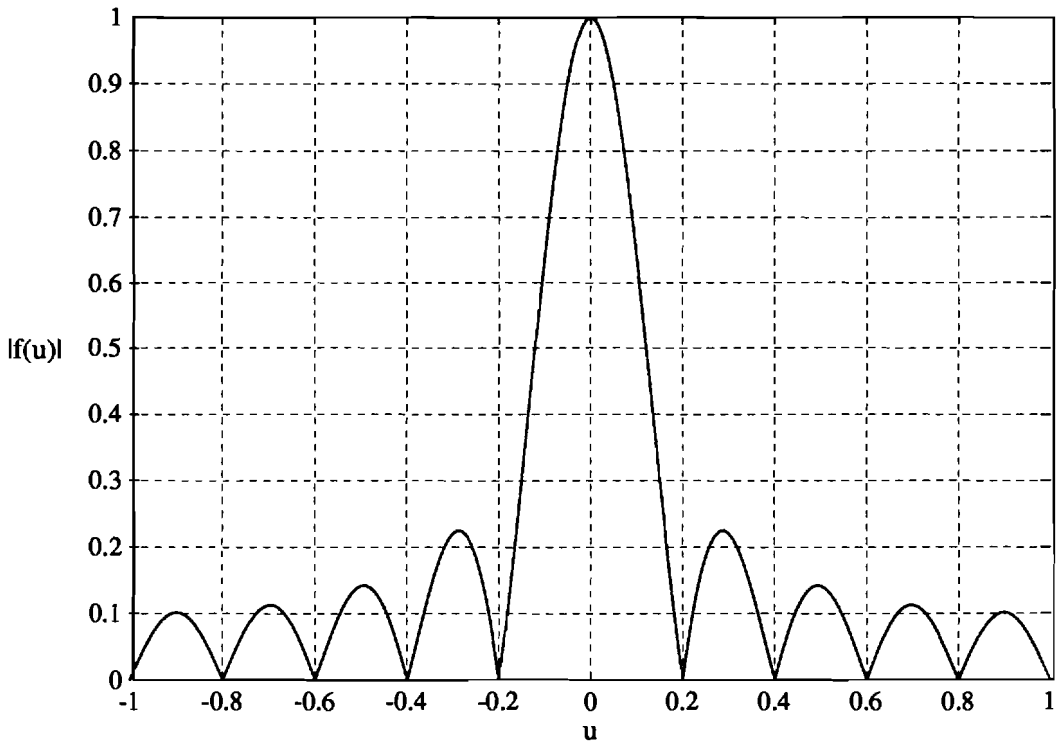

Figure 2.4 Array pattern for a 10 element ULA

have a narrow main-lobe and low side-lobes. The array can be steered to 'look' in different directions by changing the weight vector w^H. For example, (cophasal excitation) the weight vector $w^H = \underline{a}^H(\hat{r}_s)$ steers the main-lobe to the direction $\hat{r}_s$.

For illustrative purposes, we proceed to obtain the cophasal array pattern for a ULA. The ULA has N elements located on the z axis of the spherical coordinate system of Figure 2.1. The elements are spaced apart by a distance d, and the position vector at element n is $\vec{p}_n = nd\hat{z}$. The interelement spacing is assumed to be $d = \lambda/2$ to avoid grating lobes. The array manifold vector (given by Equation 2.11) corresponding to the arrival of a narrow-band plane wave of wavelength X from the direction $\hat{r}$ is

$$\underline{a}(u) = [1, e^{j\pi u}, \ldots, e^{j(N-1)\pi u}]^T, \qquad [2.20]$$

where $u = \cos\theta$. It is clear that the ULA is sensitive only to the angle 9 that the source makes with the axis of the array and that it is insensitive to the angle ϕ. The normalized cophasal beamforming weight vector required to steer the array to the direction u_s is $\mathbf{w}^H(u_s) = \underline{a}^H(u_s)/N$. Using Equation 2.19, we find that the array pattern is

$$f(u) = \exp\left[j(N-1)\frac{\pi}{2}(u-u_s)\right]\frac{\sin\left[N\frac{\pi}{2}(u-u_s)\right]}{N\sin\left[\frac{\pi}{2}(u-u_s)\right]}, \quad -1 \le u \le 1.$$

The spatial frequency response of the ULA under cophasal excitation thus has sinc-like structure. If the origin of the coordinate system had chosen to be at the center of the array, the corresponding cophasal array pattern would have been real-valued. With the origin at the center of the array, the element positions are specified by $\vec{p}_n = (\mathrm{nd} - (\mathrm{N}-1)d/2)\hat{z}$. The corresponding array manifold vector $\underline{a}'(u) = e^{-j(N-1)\pi u/2}\underline{a}(u)$ is centro-Hermitian. The corresponding real-valued array pattern is

$$f'(u) = \frac{\sin\left[N\frac{\pi}{2}(\mathrm{u}-u_s)\right]}{\mathrm{N}\sin\left[\frac{\pi}{2}(u-u_s)\right]}, \quad -1 \le u \le 1. \qquad [2.21]$$

Figure 2.4 depicts the absolute value of the array pattern for an N = 10 element ULA steered to boresight ($u_s = 0$). The main-lobe has a 3dB beamwidth u $\approx$ 0.886 x $4/N$,

and the first side-lobe is approximately 13.5dB below the level of the main-lobe. The width of the main-lobe is inversely proportional to the aperture of the array. The side-lobe levels can be lowered by applying amplitude tapers to the beamforming weight vector. This windowing operation however broadens the main lobe.

The development of the UCA-RB-MUSIC algorithm involves synthesis of real-valued array patterns for the UCA. As described in Section 2.6.2, synthesizing real-valued beam patterns reduces the computational complexity of the beamspace MUSIC algorithm.

2.6 The MUSIC Algorithm

The MUSIC (Multiple SIgnal Classification) algorithm [Sch86] for DOA estimation of narrow-band signals is described in Section 2.6.1. MUSIC is one of the 'super-resolution' algorithms that can resolve sources that are spaced less than a beamwidth apart. The Beamspace MUSIC algorithm employs a beamforming matrix to process the array data. MUSIC is then applied to the data in the transformed space (beamspace). Section 2.6.2 contains a brief description of Beamspace MUSIC. Note that the UCA-RB-MUSIC algorithm is a beamspace version of MUSIC that employs a phase mode excitation based beamformer. The MUSIC (and Beamspace MUSIC) algorithms obtain DOA estimates via a search for peaks in the MUSIC spectrum. A variation of the algorithm, Root-MUSIC [Bar83], dispenses with the need for a spectral search when a ULA is employed. Root-MUSIC provides DOA estimates via the zeros of a polynomial; the expensive search procedure required by MUSIC is replaced by a polynomial rooting procedure. Root-MUSIC was originally designed for use in conjunction with ULAs. However, employing phase mode excitation based beamformers allows Root-MUSIC and other ULA techniques to be employed in beamspace with UCAs (see Section 4.2.1, [ZM92], and [MZ92]). Section 2.6.3 describes the Root-MUSIC algorithm.

2.6.1 Element **Space MUSIC**

MUSIC is also known as 'Element Space MUSIC' when the algorithm is applied to the array data directly (no preprocessing via beamforming matrices is employed). Let us assume that d narrow-band plane waves from the distinct directions $\hat{r}_k$, k = $1, 2, \ldots,$ d are incident on an array of N elements. The standard data model $\mathbf{x}(t) = \underline{\mathbf{A}}\mathbf{s}(t) + \mathbf{n}(t)$ of Equation 2.16 describes the array output. We will assume without loss of generality that the noise vector $\mathbf{n}(t)$ is spatially white with covariance matrix $\sigma\mathbf{I}$. As in Equation 2.17, the element space covariance matrix is

$$\underline{\mathbf{R}} = \underline{\mathbf{A}}\mathbf{P}\underline{\mathbf{A}}^H + \sigma\mathbf{I}. \qquad [2.22]$$

The incident signals are assumed to be non-coherent, and the source covariance matrix P thus has full rank d. The N x N matrix $\underline{\mathbf{A}}\mathbf{P}\underline{\mathbf{A}}^H$ (called the clean covariance matrix) is Hermitian, and has rank d. Its spectral decomposition is

$$\underline{\mathbf{A}}\mathbf{P}\underline{\mathbf{A}}^H = \sum_{i=1}^{d} \underline{\lambda}_i^c \underline{\mathbf{s}}_i \underline{\mathbf{s}}_i^H + \sum_{i=d+1}^{N} \underline{\lambda}_i^c \underline{\mathbf{g}}_i \underline{\mathbf{g}}_i^H, \qquad [2.23]$$

where the eigenvalues $\underline{\lambda}_i^c$ are real-valued and satisfy

$$\underline{\lambda}_1^c \geq \cdots \geq \underline{\lambda}_d^c > 0 \text{ and } \underline{\lambda}_{d+1}^c = \cdots = \underline{\lambda}_N^c = 0.$$

The orthonormal eigenvectors $\underline{\mathbf{s}}_i$ (called signal space eigenvectors), and $\underline{\mathbf{g}}_i$ (called noise space eigenvectors) are grouped to form the matrices

$$\underline{\mathbf{S}} = [\underline{\mathbf{s}}_1, \ldots, \underline{\mathbf{s}}_d] \text{ and } \underline{\mathbf{G}} = [\underline{\mathbf{g}}_{d+1}, \ldots, \underline{\mathbf{g}}_N]. \qquad [2.24]$$

The vectors $\underline{\mathbf{g}}_i$ are in the null-space of $\underline{\mathbf{A}}\mathbf{P}\underline{\mathbf{A}}^H$, and we thus have $\underline{\mathbf{A}}^H\underline{\mathbf{g}}_i = \mathbf{0}_d$. The matrix $\underline{\mathbf{G}}$ thus spans the orthogonal complement of $\mathcal{R}(\underline{\mathbf{A}})$, and is said to span the noise subspace. The matrix $\underline{\mathbf{S}}$ clearly spans $\mathcal{R}(\underline{\mathbf{A}})$, and is said to span the signal subspace. The MUSIC spectrum defined by

$$S_e(\hat{r}) = \frac{1}{\mathbf{a}^H(\hat{r})\,\underline{\mathbf{G}}\underline{\mathbf{G}}^H\,\mathbf{a}(\hat{r})} \qquad [2.25]$$

goes to infinity when $\hat{r} = \hat{r}_i$, a true signal direction. The d peak locations in the MUSIC spectrum thus specify the source DOAs. The matrix $\underline{\mathbf{G}}\underline{\mathbf{G}}^H$ above is the

projection matrix onto the noise subspace. Note that the eigenvectors of the element space covariance matrix $\underline{\mathbf{R}}$ are identical to those of the clean covariance matrix. The spectral decomposition of the element space covariance matrix, which is what is available, is

$$\underline{\mathbf{R}} = \sum_{i=1}^{d} \underline{\lambda}_i \, \underline{\mathbf{s}}_i \underline{\mathbf{s}}_i^H + \sum_{i=d+1}^{N} \sigma \, \underline{\mathbf{g}}_i \underline{\mathbf{g}}_i^H, \qquad [2.26]$$

where $\underline{\lambda}_i = \underline{\lambda}_i^c + a$. THE EVD of $\underline{\mathbf{R}}$ thus yields the necessary bases for the signal and noise subspaces.

In practice, a finite number of snapshots, K, of array data are available. The sample covariance matrix

$$\hat{\underline{\mathbf{R}}} = \frac{1}{K} \sum_{k=1}^{K} \mathbf{x}(k)\mathbf{x}^H(k) \qquad [2.27]$$

is used as an estimator for $\underline{\mathbf{R}}$. This estimator is consistent and asymptotically efficient when the noise is Gaussian. The EVD of $\hat{\underline{\mathbf{R}}}$ reveals that d of the smallest eigenvalues are clustered together. Criteria such as the Akaike Information Criterion (AIC) or Minimum Descriptor Length (MDL) [WK85] can be employed to obtain an estimate, $\hat{d}$, of the number of sources. Given the estimate of the number of sources, the eigenvectors can be partitioned to form $\hat{\underline{\mathbf{S}}}$ and $\hat{\underline{\mathbf{G}}}$. The estimator $\hat{\underline{\mathbf{G}}}$ is then employed in (2.25) that defines the MUSIC spectrum. The location of peaks in the spectrum give the source DOAs. The MUSIC algorithm can be employed even if the noise is spatially correlated (provided the noise covariance matrix $\mathbf{R}_n$ is known). When the noise is correlated, the generalized eigenvalue decomposition (GEVD) of the matrix pencil $\{\underline{\mathbf{R}}, \mathbf{R}_n\}$ yields bases for the signal and noise subspaces.

2.6.2 Beamspace MUSIC

With beamspace MUSIC, the array output data is first processed by a beamforming matrix. The MUSIC algorithm is then applied to the transformed (beamspace) data. The dimension of the beamspace data vector may be smaller than the dimension, N, of the element space data vector. Operating in beamspace can offer a number of advantages (such as reduced computational complexity, lower SNR resolution thresholds, and reduced sensitivity to sensor perturbations) over element space

operation [ZKS93]. Beamspace processing yields rich dividends with UCAs – phase mode excitation based beamforming leads to the development of the UCA-RB-MUSIC and UCA-ESPRIT algorithms.

In the following developments we will assume that the element space noise vector has covariance matrix $\sigma\mathbf{I}$. Let F^H be the $b \times N$ beamforming matrix, where the number of beams is $b \leq N$. Each row of F^H is a beamforming weight vector that possibly steers the array to a desired direction. The effect of the beamforming matrix could thus be to limit the search for sources to a certain sector in space. The beamspace data vector is $\mathbf{y}(t) = \mathbf{F}^H\mathbf{x}(t) = \mathbf{F}^H\underline{\mathbf{A}}\mathbf{s}(t) + F^H n(t)$. The matrix $\mathbf{A} = [\mathbf{a}(\hat{r}_1), \ldots, \mathbf{a}(\hat{r}_d)] = \mathbf{F}^H\underline{\mathbf{A}}$ is the beamspace DOA matrix, and $\mathbf{a}(\hat{r}_i) = \mathbf{F}^H\underline{\mathbf{a}}(\hat{r}_i)$ are the appropriate beamspace manifold vectors. The beamspace covariance matrix is

$$\mathbf{R} = \mathbf{F}^H\underline{\mathbf{R}}\mathbf{F} = \mathbf{A}\mathbf{P}\mathbf{A}^H + \sigma\mathbf{F}^H\mathbf{F}. \qquad [2.28]$$

The beamspace noise vector has covariance matrix F^HF, and is white only if the beamformer is orthogonal (i.e., satisfies $F^HF = I$). Now, as with element space MUSIC, the GEVD of the matrix pencil $\{\mathbf{R}, \mathbf{F}^H\mathbf{F}\}$ yields matrices $\mathbf{S}$ and $\boldsymbol{G}$ that respectively span the beamspace signal and noise subspaces. The beamspace MUSIC spectrum is

$$S_b(\hat{r}) = \frac{1}{\mathbf{a}^H(\hat{r})\,\mathbf{G}\mathbf{G}^H\,\mathbf{a}(\hat{r})}. \qquad [2.29]$$

The source DOAs are obtained by searching for peaks in the spectrum as usual.

Section 2.5 addressed real-valued pattern synthesis with ULAs. The UCA-RB (Real-Beamspace) MUSIC algorithm also employs a beamformer that synthesizes real-valued beam patterns. Synthesis of real-valued patterns implies that the beamspace DOA matrix $\mathbf{A}$ is real-valued. It is clear from (2.28) that the real-valued GEVD of the matrix pencil $\{Re(R), Re(F^HF)\}$ yields bases for the beamspace signal and noise subspaces in such cases. Synthesizing real-valued patterns thus reduces the computational complexity, as only real-valued EVDs are required.

2.6.3 Root-MUSIC

Root-MUSIC [Bar83, ZKS93] is a variation of the MUSIC algorithm that was originally developed for use in conjunction with ULAs. Root-MUSIC provides DOA estimates via the zeros of a polynomial, and the computationally expensive spectral search procedure required by MUSIC is avoided. As seen in Section 2.5, the ULA manifold vectors are Vandermonde. This allows the denominator of the MUSIC spectrum of Equation 2.25 to be written as a polynomial. The zeros of this polynomial that are close to the unit circle identify the source arrival angles as described below. The ULA manifold vector defined in Equation 2.20 is $\underline{\mathbf{a}}(u) = [1, e^{j\pi u}, \ldots, e^{j(N-1)\pi u}]^T$. The manifold vector can be written in terms of the complex variable z as follows:

$$\underline{\mathbf{a}}(z) = [1, z, z^2, \cdots, z^{N-1}]^T,$$

where it is understood that $z = e^{j\pi u}$ lies on the unit circle. The denominator of the MUSIC spectrum of Equation 2.25 can be expressed as the polynomial

$$Q(z) = \underline{\mathbf{a}}^H(z)\underline{\mathbf{G}}\underline{\mathbf{G}}^H\underline{\mathbf{a}}(z). \qquad [2.30]$$

We have $Q(z_i) = 0$ when $z_i = e^{j\pi u_i}$ corresponds to a true signal arrival direction. The roots of the equation $Q(z) = 0$ that are close to the unit circle thus identify the signal DOAs. The polynomial $Q(z)$ above has order $2(N-1)$ and its coefficients are easily shown to be centro-Hermitian. Thus if z_i is a zero of $Q(z)$, so is $1/z_i^*$. The roots thus occur in pairs on radial lines in the z plane. A root z_i close to the unit circle corresponds to a source in the direction u; $= \arg(z_i)/\pi$.

The Root-MUSIC algorithm offers better performance than spectral MUSIC as has been documented in [RH89b]. Root-MUSIC has a lower failure rate than spectral MUSIC [SS91]. A 'failure' here refers to the presence of only a single peak in the MUSIC spectrum, when two closely spaced sources are present in reality. Root-MUSIC exhibits two distinct signal zeros in many of the cases where spectral MUSIC fails to resolve the two sources. Our initial research efforts [ZM92, MZ92] focused on applying Root-MUSIC with UCAs to perform the azimuthal search for sources

at a given elevation. Although Root-MUSIC cannot be employed in element space with UCAs, the phase mode excitation based transformation to beamspace induces a beamspace manifold vector whose azimuthal dependence is through a Vandermonde vector. This property allows Root-MUSIC to be employed in beamspace with UCAs. Section 4.2.1 discusses how Root-MUSIC is applicable as part of the UCA-RB-MUSIC algorithm.

3. BEAMFORMING FOR CIRCULAR RING ARRAYS/APERTURES

This chapter reviews beamforming techniques for circular ring arrays/apertures. Two beamforming techniques – standard cophasal beamforming, and phase mode excitation based beamforming are studied. The UCA-RB-MUSIC and UCA-ESPRIT algorithms employ phase mode excitation based beamformers, and most of the attention is thus focused on phase mode excitation based beamformers. Discussions on phase mode excitation of UCAs can be found in [Dav83, LCD67, CZ69]. Cophasal excitation is not employed in the development of UCA-RB-MUSIC or UCA-ESPRIT: the discussion is included for the sake of completeness. Further details on cophasal beamforming with UCAs can be found in [Ma74]. The discussions on beamforming first address the case of the circular ring aperture. The UCA (sampled version of the circular ring aperture) is then considered. The development of UCA-RB-NIUSIC and UCA-ESPRIT requires that the UCA far-field patterns closely approximate those of circular ring apertures. This can be accomplished by judicious choice of the number of array elements.

The UCA geometry is introduced in Section 3.1; expressions for the UCA manifold vectors are also obtained. Section 3.2 describes cophasal beamforming for circular arrays/apertures. Phase mode excitation of UCAs is next discussed in Section 3.3. A discussion on the number of independent modes that can be excited with a given aperture and the selection of the number of array elements is included. Phase mode excitation based pattern synthesis for UCAs is described in Appendix B.

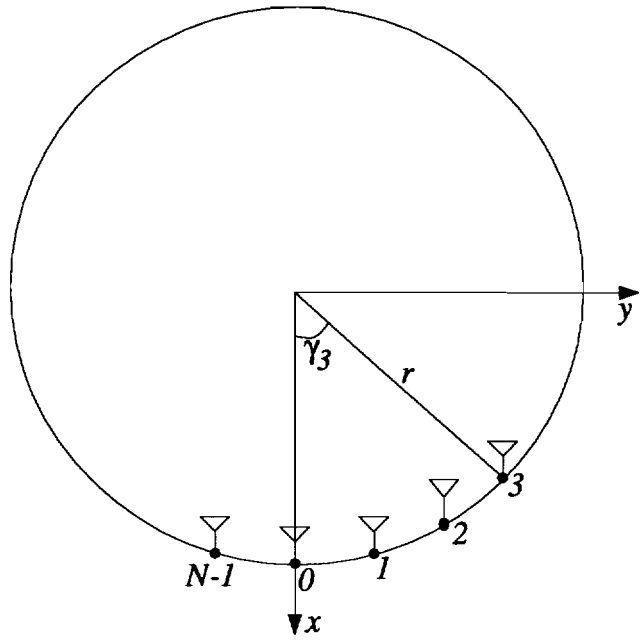

Figure 3.1 Uniform circular array geometry.

3.1 Uniform Circular Array Geometry

The UCA geometry is depicted in Figure 3.1. The antenna elements, assumed to be identical and omnidirectional, are uniformly distributed over the circumference of a circle of radius r in the xy plane. A spherical coordinate system is used to represent the arrival directions of the incoming plane waves. The origin of the coordinate system is located at the center of the array. Source elevation angles $\theta \in [0, \pi/2]$ are measured down from the z axis, and azimuth angles $\phi \in [0, 2\pi]$ are measured counterclockwise from the x axis.

Element n of the array is displaced by an angle $\gamma_n = 2\pi n/N$ from the x axis. The position vector at this location is $\vec{p}_n = (r\,\text{cosy},,\ r\sin\gamma_n, 0)$. Consider a narrowband plane wave with wavenumber $k_0 = 2\pi/\lambda$ propagating in the direction $-\hat{r}$ with elevation and azimuth θ and ϕ, respectively. The unit vector $\hat{r}$ has cartesian coordinates $\hat{r} = (\text{u}, \text{v}, \cos\theta)$: $\text{u} = \sin\theta\cos\phi$, and $v = \sin\theta\sin\phi$ are respectively the direction cosines with respect to the x and y axes. From this point onwards, the vector $\boldsymbol{\theta} = (\zeta, \phi)$ where $\zeta = k_0 r \sin\theta$, or the vector $\boldsymbol{\beta} = (\text{u}, \text{v})$ will be used to represent

the DOA of a signal (rather than the vector $\hat{r}$ as in the previous chapter). At any given time instant, the signal complex envelopes received at the origin and at element n differ in phase by $\psi_n = e^{jk_0\hat{r}\cdot\vec{p}_n} = e^{jk_0 r(u\cos\gamma_n + v\sin\gamma_n)} = e^{j\zeta\cos(\phi-\gamma_n)}$. The element space UCA manifold vector thus has the following representations:

$$\underline{\mathbf{a}}(\boldsymbol{\theta}) = \begin{bmatrix} e^{j\zeta\cos(\phi-\gamma_0)} \\ e^{j\zeta\cos(\phi-\gamma_1)} \\ \\ e^{j\zeta\cos(\phi-\gamma_{N-1})} \end{bmatrix}, \quad \underline{\mathbf{a}}(\boldsymbol{\beta}) = \begin{bmatrix} e^{jk_0 r(u\cos\gamma_0 + v\sin\gamma_0)} \\ e^{jk_0 r(u\cos\gamma_1 + v\sin\gamma_1)} \\ \\ e^{jk_0 r(u\cos\gamma_{N-1} + v\sin\gamma_{N-1})} \end{bmatrix} \qquad [3.1]$$

The representation in terms of 8 will be used in the development of the UCA-RB-MUSIC and UCA-ESPRIT algorithms. The representation in terms of $\boldsymbol{\beta}$ is more convenient for performance analysis of the algorithms.

3.2 Cophasal Excitation of Circular Arrays/Apertures

Cophasal excitation of arrays with arbitrary geometries was discussed in Section 2.5. In this type of beamforming, the beamformer weights steer the array to the desired 'look' direction by compensating for the corresponding phase shifts at each element location. The Bessel function of the first kind, J_0, describes the far-field pattern resulting from cophasal excitation of circular ring apertures. In the following discussion of cophasal excitation, the vector $\boldsymbol{\beta}$ of direction cosines is used to represent source arrival directions.

3.2.1 Circular Ring Aperture: Cophasal Excitation

We proceed to obtain the expression for the far-field pattern $\mathrm{f}^c(\boldsymbol{\beta}, \boldsymbol{\beta}_s)$ that describes the aperture gain in the direction $\boldsymbol{\beta} = (\mathrm{u}, \mathrm{v})$ when cophasal beamforming is employed to steer the aperture to the direction $\boldsymbol{\beta}_s = (u_s, v_s)$. The superscript c signifies that the pattern corresponds to a continuous aperture. It is useful to define the difference vector

$$\boldsymbol{\beta}_d - \boldsymbol{\beta} - \boldsymbol{\beta}_s = (u_d, v_d), \text{ where } u_d = \mathrm{u} - u_s, \text{ and } v_d = v - v_s. \qquad [3.2]$$

Let the representation of $\boldsymbol{\beta}_d$ in polar coordinates be (τ, v). We have

$$\tau = \sqrt{u_d^2 + v_d^2}, \text{ and } \nu = \tan^{-1}(v_d/u_d). \qquad [3.3]$$

The beamformer weight required at angular position $\gamma \in [0, 2\pi]$ to steer the aperture to the direction $\boldsymbol{\beta}_s$ is $w(\gamma) = e^{-jk_0 r(u_s \cos\gamma + v_s \sin\gamma)}$. The resulting far-field pattern is

$$f^c(\boldsymbol{\beta}, \boldsymbol{\beta}_s) = \int_0^{2\pi} e^{jk_0 r(u_d \cos\gamma + v_d \sin\gamma)}\, d\gamma.$$

This integral can be simplified using the property $J_0(x) = \frac{1}{2\pi}\int_0^{2\pi} e^{jx\cos y}\,\mathrm{dy}$ to obtain the following expression for the far-field pattern:

$$f^c(\boldsymbol{\beta}, \boldsymbol{\beta}_s) = J_0(k_0 r\tau). \qquad [3.4]$$

The cophasal beam-pattern of circular ring apertures is thus described by the Bessel function J_0. Note that the array gain in the direction $\boldsymbol{\beta}$ depends only on the distance $\tau = \|\boldsymbol{\beta}_d\|$ (in the uv plane) between this direction and the 'look' direction.

3.2.2 Uniform Circular Array: Cophasal Excitation

As discussed in Section 2.5, the beamforming weight vector required to steer the UCA to the direction $\boldsymbol{\beta}_s$ is just $\mathrm{w}^{\mathrm{H}} = \underline{\mathbf{a}}^H(\boldsymbol{\beta}_s)/N$. The corresponding far-field pattern is $f^s(\boldsymbol{\beta}, \boldsymbol{\beta}_s) = \underline{\mathbf{a}}^H(\boldsymbol{\beta}_s)\underline{\mathbf{a}}(\boldsymbol{\beta})/N$, where the superscript s signifies a sampled aperture. Substituting for $\underline{\mathbf{a}}$ from Equation 3.1, we obtain

$$f^s(\boldsymbol{\beta}, \boldsymbol{\beta}_s) = \frac{1}{N}\sum_{n=0}^{N-1} e^{jk_0 r\tau\cos(\nu - 2\pi n/N)},$$

where τ and ν are defined in Equation 3.3. Employing a procedure similar to that used to prove Equation 3.10, the above directional pattern can be expressed as

$$f^s(\boldsymbol{\beta}, \boldsymbol{\beta}_s) = J_0(k_0 r\tau) + 2\sum_{q=1}^{\infty} j^{Nq} J_{Nq}(k_0 r\tau)\cos(Nq\nu). \qquad [3.5]$$

The first term in the above expression (called the principal term) is identical to the far-field pattern for the continuous aperture. The remaining terms, called residual terms, arise due to sampling of the continuous aperture. The principal term dominates

the pattern provided N is sufficiently large. The residual term that contributes the most to $f^s(\beta, \beta_s)$ is the term with index q = 1. The amplitude of this term is no greater than $|J_N(k_0 r\tau)|$. The argument of the Bessel function is bounded by $2k_0 r$, since $\tau \in [0, 2]$. Now, $J_N(2k_0 r)$ is small if N $> 2k_0 r$: this is because the value of the Bessel function is small when its order excceeds its argument. Choosing a sufficiently large number, N, of array elements thus virtually eliminates the contribution of the residual terms. The discussion in Section 3.3.2 of phase mode excitation for UCAs includes a more detailed account on the contribution of residual terms.

3.3 Phase Mode Excitation of Circular Arrays/Apertures

In this excitation technique, the phase of the excitation function (beamformer weight) increases linearly as the circular aperture is traversed. This linear increase of phase is similar to the cophasal excitation of a ULA. The excitation function corresponding to phase mode m (for integer m) for a circular ring aperture is $w_m(\gamma) = e^{jm\gamma}$, $\gamma \in [0, 2\pi]$. The excitation function for phase mode m undergoes a phase increment of $2m\pi$ on traversing the circle. It is clear that phase mode m is just a spatial harmonic of any arbitrary excitation function: The arbitrary excitation function $w'(\gamma)$ has the expansion $w'(\gamma) = \sum_{m=-\infty}^{\infty} c_m e^{jm\gamma}$, where c_m is the Fourier series coefficient corresponding to phase mode m.

Phase mode excitation is the basis for a powerful pattern synthesis technique for circular arrays. Attractive directional patterns (with good directivity properties) can be synthesized using phase mode excitation [Dav83]. Pattern synthesis is however not of direct concern in the development of UCA-RB-MUSIC and UCA-ESPRIT. The algorithms rather exploit the structure of the induced beamspace manifold to advantage. Our initial efforts [ZM92, MZ92] on applying ULA techniques with UCAs focused on synthesizing sinc-type patterns with UCAs. A discssion of phase mode excitation based pattern synthesis for UCAs is thus included in Appendix B. In the following discussion of phase mode excitation for circular arrays, sources DOAs are represented by the vector $\theta = (\zeta, \phi)$, where $\zeta = k_0 r \sin\theta$.

3.3.1 Circular Ring Aperture: Phase Mode Excitation

The excitation function corresponding to phase mode m (for integer m) is $w_m(\gamma) = e^{jm\gamma}$. The resulting far-field pattern is $f_m^c(\boldsymbol{\theta}) = \frac{1}{2\pi}\int_0^{2\pi} w_m(\gamma)e^{j\zeta\cos(\phi-\gamma)}\,d\gamma$. Again, the superscript c signifies a continuous aperture. As shown in Appendix A.1, the far-field pattern can be expressed as follows:

$$f_m^c(\boldsymbol{\theta}) = j^m J_m(\zeta)e^{jm\phi}. \qquad [3.6]$$

In the above expression, $J_m(\zeta)$ is the Bessel function of the first kind of order m. The following observations can be made about the far-field pattern. First, the azimuthal variation $e^{jm\phi}$ in the far-field pattern has the same form as the excitation function $e^{jm\gamma}$. This property is the basis for phase mode excitation based pattern synthesis with UCAs, as described in Appendix B. Second, the elevation dependence (and also the amplitude) of the far-field pattern is through the Bessel function $J_m(\zeta)$. This places limitations on the number of independent modes that can be excited by a given circular aperture, as described below.

Number of Modes Excitable with a given Circular Aperture

Let M denote the highest order mode that can be excited by the aperture at a reasonable strength. A rule of thumb for determining M is [Dav83]

$$M \approx k_0 r. \qquad [3.7]$$

This is justified as follows: The visible region $\theta \in [0, \pi/2]$ translates into $\zeta = k_0 r \sin\theta \in [0, k_0 r]$. M is chosen as above because the mode amplitude $J_m(\zeta)$ is small when the Bessel function order m exceeds its argument ζ. For mode orders $|m| \geq$ M, $f_m^c(\boldsymbol{\theta})$ is small over the entire visible region. The beamformer for such a mode m thus severely attenuates sources from all directions. The M' $= 2$M$+1$ phase modes, m $\in [-$M$, M]$ (where M is specified by Equation 3.7) can thus be excited at a reasonable strength by a given aperture.

The following example illustrates the limit on the number of excitable modes. Consider a circular aperture of radius $r =$ A. Equation 3.7 suggests that the maximum

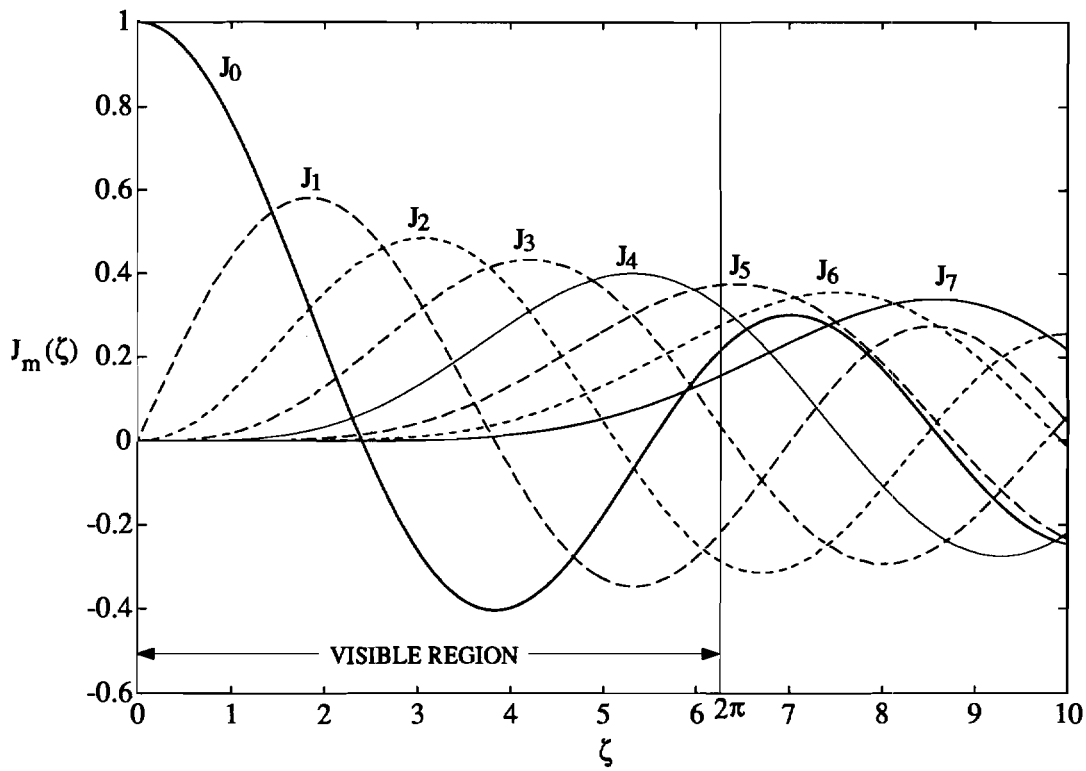

Figure **3.2** Bessel functions.

mode order is M = 6 (the closest integer to 2π). The Bessel functions of order 0 through 7 are plotted in Figure 3.2. The figure reveals that $J_7(\zeta)$ is indeed small over the entire visible region $0 \leq \zeta \leq 2\pi$. Thus only phase modes of order m $\in [-6, 6]$ can be excited at a reasonable strength by the aperture.

3.3.2 Uniform Circular Array: Phase Mode Excitation

We now consider phase mode excitation of an N element UCA. The normalized beamforming weight vector that excites the array with phase mode m, $|m| \leq$ M is

$$\mathbf{w}_m^H = \frac{1}{N}[e^{jm\gamma_0}, e^{jm\gamma_1}, \cdots, e^{jm\gamma_{N-1}}] = \frac{1}{N}[1, e^{j2\pi m/N}, \cdots, e^{j2\pi m(N-1)/N}]. \qquad [3.8]$$

The resulting array pattern $f_m^s(\boldsymbol{\theta})$, where the superscript s denotes the sampled aperture, is

$$f_m^s(\boldsymbol{\theta}) = \mathbf{w}_m^H \underline{\mathbf{a}}(\boldsymbol{\theta}) = \frac{1}{N} \sum_{n=0}^{N-1} e^{jm\gamma_n} e^{j\zeta \cos(\phi - \gamma_n)}. \qquad [3.9]$$

As shown in Appendix A.2, the array pattern can be expressed as follours [Dav83, CZ69]:

$$f_m^s(\boldsymbol{\theta}) = j^m J_m(\zeta) e^{jm\phi} + \sum_{q=1}^{\infty} \left(j^g J_g(\zeta) e^{-jg\phi} + j^h J_h(\zeta) e^{jh\phi} \right), \quad |m| < N, \qquad [3.10]$$

where $g =$ Nq$-$m and h $= Nq+m$. The first term in this equation, the principal term, is identical to the far-field pattern of Equation 3.6 corresponding to the continuous circular aperture. The remaining terms arise due to sampling of the continuous aperture, and are called residual or aliasing terms. Examination of Equation 3.10 reveals that the condition N $> 2|m|$ must be satisfied for the principal term to be the dominant one. The highest mode excited has order M, and we therefore need

$$N > 2M \qquad [3.11]$$

array elements. This condition is identical to the Nyquist sampling criterion, as M defines the maximum spatial frequency component in the array excitation. With M $= k_0 r$ as in Equation 3.7, it is clear that (3.11) requires the circumferential spacing between adjacent array elements to be less than 0.5λ. Note that an interelement

Table 3.1 Maximum residual term contribution as a function of N for a UCA with r = λ and $M = 6$.

N	13	14	15	16	17	18	19
$J_{N-M}(k_0 r)$	0.158	0.073	0.029	0.010	0.003	8.8e-4	2.3e-4

spacing of 0.5λ is sufficient to avoid grating lobes with ULAs. In practice, employing $N \geq 2M + 5$ elements is sufficient to make the residual term contributions negligible. With $N \geq 2M + 5$ elements, the UCA far-field pattern closely follows that of the continuous circular aperture. The following discussion addresses this issue in more detail.

Choosing N to make Residual Term Contributions Negligible

The residual term that contributes the most to the far-field pattern of Equation **3.10** arises from the q = **1** index. The amplitude of this term fbllows the Bessel function of order $N - |m|$. The residual contribution is clearly maximum for mode M, and the amplitude of this residual term follows $J_{N-M}(\zeta)$. Now $J_{N-M}(\zeta)$ is monotone increasing over the visible region $[0, k_0 r]$ by virtue of the choice of M and N in Equations **3.7** and **3.11.** $J_{N-M}(k_0 r)$ is therefore an upper bound on the maximum contribution of any residual term. This upper bound can be made as small as desired by making the number N of array elements sufficiently large.

We return to the example of the UCA of radius r = λ with $M = 6$ to illustrate the selection of N. Equation **3.11** requires that the array have $N > 12$ elements. The upper bound on the maximum residual contribution, $J_{N-M}(k_0 r)$, is tabulated in Table **3.1** for various values of N. The table indicates that the residual contribution is 'small enough' to be ignored for $N > 15$ elements (circumferential spacing $< 0.42\lambda$). Thus having $N > 15$ elements ensures that the UCA far-field patterns corresponding to phase mode excitation with mode orders $|m| \leq M = 6$ are virtually identical to the far-field patterns of Equation **3.6** corresponding to a continuous: aperture.

The development of the UCA-RB-MUSIC and UCA-ESPRIT algorithms in the following chapter assume that the maximum mode M and the number of array elements N have been chosen according to the design guidelines established in this section. The principal term thus characterizes the UCA far-field pattern. for mode orders $|m| \leq$ M: We have

$$f_m^s(\boldsymbol{\theta}) \approx j^m J_m(\zeta) e^{jm\phi} = j^{|m|} J_{|m|}(\zeta) e^{jm\phi}, \ |m| \leq M. \qquad [3.12]$$

The final equality above follows from the property $J_{-m}(\zeta) = (-1)^m J_m(\zeta)$ of Bessel functions.

4. DEVELOPMENT OF UCA-RB-MUSIC AND UCA-ESPRIT

The UCA-RB-MUSIC and UCA-ESPRIT algorithms for 2D angle estimation with UCAs are described in this chapter. Both algorithms operate in beamspace and employ phase mode excitation based beamformers. The beamforming matrices employed by the algorithms are constructed in Section 4.1. Section 4.2 describes the UCA-REI-MUSIC algorithm: the advantages UCA-RB-MUSIC offers over element space MUSIC are discussed in some detail. The UCA-ESPRIT algorithm is next developed in Section 4.3. The changes in the UCA manifold due to mutual coupling between array elements is described in Section 4.4. Simple modifications that enable UCA-RB-MUSIC and UCA-ESPRIT to account for mutual coupling effects are presented. Section 4.5 investigates the use of directional antenna elements with UCAs. Both UCIA-RB-MUSIC and UCA-ESPRIT are applicable if the element patterns are omnidirectional in azimuth (only elevation dependent). Although UCA-ESPRIT cannot be employed when the elements have arbitrary patterns, a phase mode excitation based beamspace MUSIC algorithm is still applicable.

4.3. Beamforming Matrices for UCA-RB-MUSIC and UCA-ESPRIT

Three phase mode excitation based beamformers that synthesize beamspace manifolds of dimension $M' = 2M + 1$ are developed in this section. The beamforming matrices are denoted $\mathbf{F}_e^H$, $\mathbf{F}_r^H$, and $\mathbf{F}_u^H$; the corresponding beamspace manifolds are $\mathbf{a}_e(\theta)$, $\mathbf{a}_r(\theta)$, and $\mathbf{a}_u(\theta)$, respectively. The subscipts e, r, and u respectively stand for 'even', 'real-valued' and 'UCA-ESPRIT' for reasons that will soon be apparent. All three beamformers are orthogonal (have orthonormal rows), and satisfy $F^H F = I$.

The orthogonal matrix

$$\mathbf{V} = \sqrt{N}[\mathbf{w}_{-M} \vdots \cdots \vdots \mathbf{w}_0 \vdots \cdots \vdots \mathbf{w}_M] \quad [4.1]$$

is the building block for the three beamformers. It is evident from Equation *3.8* that the rows of the M' x N matrix V^{H} are phase mode excitation beamforming weight vectors. These rows are in fact an M' dimensional subset of the N IDF'T (Inverse Discrete Fourier Transform) weight vectors.

The beamforming matrix $\mathbf{F}_{\mathbf{e}}^{H}$ is defined as follows:

$$\begin{aligned} \mathbf{F}_{\mathbf{e}}^{H} &= \mathbf{C}_{\mathbf{e}}\mathbf{V}^{H}, \text{ where} & [4.2] \\ \mathbf{C}_{\mathbf{e}} &= \text{diag}\{j^{-M}, \ldots, j^{-1}, j^{0}, j^{-1}, \ldots, j^{-M}\}. \end{aligned}$$

The diagonal, unitary matrix $\mathbf{C}_{\mathbf{e}}$ serves to eliminate factors of the form $j^{|m|}$ in Equation *3.12.* The resulting beamspace manifold vectors thus have the form

$$\begin{aligned} \mathbf{a}_{\mathbf{e}}(\boldsymbol{\theta}) &= \mathbf{F}_{\mathbf{e}}^{H}\underline{\mathbf{a}}(\boldsymbol{\theta}) \approx \sqrt{N}\mathbf{J}(\zeta)\mathbf{v}(\phi), \text{ where} & [4.3] \\ \mathbf{J}(\zeta) &= \text{diag}\{J_M(\zeta), \ldots, J_1(\zeta), J_0(\zeta), J_1(\zeta), \ldots, J_M(\zeta)\}, \text{ and} & [4.4] \\ \mathbf{v}(\phi) &= [e^{-jM\phi}, \ldots, e^{-j\phi}, e^{j0}, e^{j\phi}, \ldots, e^{jM\phi}]^{T} & [4.5] \end{aligned}$$

The azimuthal variation of $\mathbf{a}_{\mathbf{e}}(\boldsymbol{\theta})$ is through the vector $\mathbf{v}(\phi)$ that is similar in form to the ULA manifold vector. The elevation dependence takes the form of a !symmetric amplitude taper through the matrix $\mathbf{J}(\zeta)$ of Bessel functions. The diagonal elements of $\mathbf{J}(\zeta)$ are even about the center element; thence the subscript e. The beamspace manifold $\mathbf{a}_{\mathbf{e}}(\boldsymbol{\theta})$ is centro-Hermitian and satisfies $\tilde{\mathbf{I}}\mathbf{a}_{\mathbf{e}}(\boldsymbol{\theta}) = \mathbf{a}_{\mathbf{e}}^{*}(\boldsymbol{\theta})$, where $\tilde{\mathbf{I}}$ is the reverse permutation matrix with ones on the anti-diagonal and zeros elsewhere. Employing the beamformer $\mathbf{F}_{\mathbf{e}}^{H}$ thus allows a Forward-Backward (FB) average to be performed in beamspace.

The centro-Hermitian nature of $\mathbf{a}_{\mathbf{e}}(\boldsymbol{\theta})$ motivates the development of the beamformer $\mathbf{F}_{\mathbf{r}}^{H}$ that synthesizes a real-valued beamspace manifold. We have

$$\begin{aligned} \mathbf{F}_{\mathbf{r}}^{H} &= \mathbf{W}^{H}\mathbf{F}_{\mathbf{e}}^{H} = \mathbf{W}^{H}\mathbf{C}_{\mathbf{e}}\mathbf{V}^{H}, \text{ and} & [4.6] \\ \mathbf{a}_{\mathbf{r}}(\boldsymbol{\theta}) &= \mathbf{F}_{\mathbf{r}}^{H}\underline{\mathbf{a}}(\boldsymbol{\theta}) = \mathbf{W}^{H}\mathbf{a}_{\mathbf{e}}(\boldsymbol{\theta}) = \sqrt{N}\mathbf{W}^{H}\mathbf{J}(\zeta)\mathbf{v}(\phi). & [4.7] \end{aligned}$$

It is evident that the beamspace manifold $\mathbf{a_r}(\boldsymbol{\theta})$ is real-valued if the matrix W^H has centro-Hermitian rows. Orthogonality of $\mathbf{F_r^H}$ is maintained by restricting W to be unitary. An appropriate sparse matrix W^H and the corresponding beamspace manifold are given below. The symbol $\mathbf{0}_M$ denotes a zero vector of length M.

$$\mathbf{W}^H = \frac{1}{\sqrt{2}} \begin{bmatrix} \mathbf{I}_M & \mathbf{0}_M & \tilde{\mathbf{I}}_M \\ \mathbf{0}_M^T & \sqrt{2} & \mathbf{0}_M^T \\ j\tilde{\mathbf{I}}_M & \mathbf{0}_M & -j\tilde{\mathbf{I}}_M \end{bmatrix}, \text{ and} \qquad [4.8]$$

$$\mathbf{a_r}(\boldsymbol{\theta}) = \sqrt{2N}[J_M(\zeta)\cos(M\phi), \ldots, J_1(\zeta)\cos(\phi), \frac{1}{\sqrt{2}} J_0(\zeta), J_1(\zeta)\sin(\phi), \ldots, J_M(\zeta)\sin(M\phi)]^T. \qquad [4.9]$$

Another choice of W and the corresponding real-valued beamspace manifold are as follows:

$$\mathbf{W} = \frac{1}{\sqrt{M'}}[\mathbf{v}(\alpha_{-M}) \vdots \ldots \vdots \mathbf{v}(\alpha_0) \vdots \cdots \vdots \mathbf{v}(\alpha_M)], \text{ and} \qquad [4.10]$$

$$\mathbf{a_r}(\theta) = [f(\zeta, \phi - \alpha_{-M}), \ldots, f(\zeta, \phi - \alpha_{-1}), f(\zeta, \phi), f(\zeta, \phi - \alpha_1), \ldots, f(\zeta, \phi - \alpha_M)]^T, \qquad [4.11]$$

where $f(\zeta, \phi) = \sqrt{\frac{N}{M'}}[J_0(\zeta) + 2\sum_{m=1}^{M} J_m(\zeta)\cos(m\phi)]$, and $\alpha_i = 2\pi i/M'$, $i \in [-M, M]$. With this choice of W, the beamformer $\mathbf{F_r^H}$ synthesizes the basic beam pattern $f(\zeta, \phi)$ which is just the sum of the components of $\mathbf{a_e}(\boldsymbol{\theta})$. Multiple beams are obtained by rotating this basic pattern in azimuth by the angles α_i. Having a real-valued beamspace manifold is advantageous for computational reasons. It allows subspace estimates to be obtained via real-valued EVDs as opposed to complex-valued EVDs, and thus provides computational savings. The UCA-RB-MUSIC algorithm developed in the following section exploits this property.

The last beamformer $\mathbf{F_u^H}$ synthesizes the beamspace manifold $\mathbf{a_u}(\boldsymbol{\theta})$ whose special structure is exploited in the development of the UCA-ESPRIT algorithm. The beamformer is defined by

$$\mathbf{F_u^H} = \mathbf{C_u V}^H, \text{ where} \qquad [4.12]$$

$$\mathbf{C_u} = \text{diag}\{j^M, \ldots, j^1, j^0, j^{-1}, \ldots, j^{-M}\}.$$

The diagonal, unitary matrix $\mathbf{C_u}$ serves to eliminate factors of the form j^m in Equation 3.12. The resulting beamspace manifold is

$$\mathbf{a_u}(\boldsymbol{\theta}) = \mathbf{F}_{\mathbf{u}}^H \underline{\mathbf{a}}(\boldsymbol{\theta}) \approx \sqrt{N}\mathbf{J}_-(\zeta)\mathbf{v}(\phi), \text{ where} \quad [4.13]$$

$$\mathbf{J}_-(\zeta) = \text{diag}\{J_{-M}(\zeta), \ldots, J_{-1}(\zeta), J_0(\zeta), J_1(\zeta), \ldots, J_M(\zeta)\}, \quad [4.14]$$

and $\mathbf{v}(\phi)$ is defined in Equation 4.5. Examination of Equations 4.6 and 4.12 shows that a unitary transformation relates the beamformers $\mathbf{F}_{\mathbf{u}}^H$ and $\mathbf{F}_{\mathbf{r}}^H$: We have $\mathbf{F}_{\mathbf{u}}^H = \mathbf{C_o}\mathbf{W}\mathbf{F}_{\mathbf{r}}^H$, where

$$\mathbf{C_o} = \mathbf{C_u}\mathbf{C_e}^H = \text{diag}\{(-1)^M, \ldots, (-1)^1, 1, 1, \ldots, 1\}. \quad [4.15]$$

The same transformation thus relates the corresponding beamspace manifold vectors: We have

$$\mathbf{a_u}(\boldsymbol{\theta}) = \mathbf{C_o}\mathbf{W}\mathbf{a_r}(\boldsymbol{\theta}). \quad [4.16]$$

This property enables computation of the beamspace signal subspace matrix for UCA-ESPRIT via a real-valued EVD.

4.2 **Development** of UCA-RB-MUSIC

UCA-RB (Real-Beamspace) MUSIC employs the beamformer $\mathbf{F}_{\mathbf{r}}^H$ that synthesizes the real-valued beamspace manifold $\mathbf{a_r}(\boldsymbol{\theta}) = \sqrt{N}\mathbf{W}^H\mathbf{J}(\zeta)\mathbf{v}(\phi)$ of Equation 4.7. Depending on the choice of W, $a_r(0)$ has the form of Equation 4.9 or Equation 4.11. Since $\mathbf{a_r}(\boldsymbol{\theta})$ is real-valued, signal eigenvector estimates can be obtained via a real-valued EVD as described below. This reduction in computation (element space MUSIC requires a complex-valued EVD) is one of the advantages of UCA-RB-MUSIC.

Let $\underline{\mathbf{A}} = [\underline{\mathbf{a}}(\boldsymbol{\theta}_1), \ldots, \underline{\mathbf{a}}(\boldsymbol{\theta}_d)]$ be the N x d DOA matrix, assuming that d signals impinge on the array. Using the standard data model, the element space data vector can be represented as follows: $\mathbf{x}(t) = \underline{\mathbf{A}}\mathbf{s}(t) + \mathbf{n}(t)$, where $\mathbf{s}(t)$ is the vector of signal complex envelopes, and $\mathbf{n}(t)$ is the noise vector. The signals and the noises are assumed to be stationary, zero mean, uncorrelated random processes. The incident signals are assumed to be non-coherent, and the source covariance matrix $\mathbf{P} = \mathrm{E}[\mathrm{s(t)s^H(t)}]$ is

thus positive definite. The noise process $\mathbf{n}(t)$ is assumed to be complex Gaussian distributed and spatially white with covariance matrix $\sigma\mathbf{I}$. The element space covariance matrix $\underline{\mathbf{R}} = \mathrm{E}[\mathbf{x}(t)\mathbf{x}^H(t)]$ thus has the form

$$\underline{\mathbf{R}} = \underline{\mathbf{A}}\mathbf{P}\underline{\mathbf{A}}^H + \sigma\mathbf{I}. \qquad [4.17]$$

Eniploying the beamformer $\mathbf{F}_\mathbf{r}^H$ yields the beamspace data vector $\mathbf{y}(t) = \mathbf{F}_\mathbf{r}^H\mathbf{x}(t) = \mathbf{A}_\mathbf{r}\mathbf{s}(t) + \mathbf{F}_\mathbf{r}^H\mathbf{n}(t)$, where $\mathbf{A}, = \mathbf{F}_\mathbf{r}^H\underline{\mathbf{A}}$ is the real-valued beamspace DOA matrix. The corresponding beamspace covariance matrix is denoted $\mathbf{R}_\mathbf{y}$. Expressions for $\mathbf{R}_\mathbf{y}$ and the matrix $\mathbf{R} = \mathrm{Re}\{\mathbf{R}_\mathbf{y}\}$ are given below:

$$\mathbf{R}_\mathbf{y} = \mathbf{F}_\mathbf{r}^H\underline{\mathbf{R}}\mathbf{F}_\mathbf{r} = \mathbf{A}_\mathbf{r}\mathbf{P}\mathbf{A}_\mathbf{r}^T + \sigma\mathbf{I} \qquad [4.18]$$

$$\mathbf{R} = \mathrm{Re}\{\mathbf{R}_\mathbf{y}\} = \mathbf{A}_\mathbf{r}\mathbf{P}_R\mathbf{A}_\mathbf{r}^T + \sigma\mathbf{I}, \qquad [4.19]$$

where $\mathbf{P}_R = \mathrm{Re}\{\mathbf{P}\}$. It is clear that the real-valued EVD of $\mathbf{R}$ yields bases for the beamspace signal and noise subspaces. Let $\lambda_1 > \cdots > \lambda_d > \lambda_{d+1} = \cdots = \lambda_{M'} = \boldsymbol{a}$ be the ordered eigenvalues of $\mathbf{R}$, and let $\mathbf{s}_1, \ldots, \mathbf{s}_d, \mathbf{g}_{d+1}, \ldots, \mathbf{g}_{M'}$ be the corresponding orthonormal eigenvectors. The real-valued matrices $\mathbf{S}$ and $\boldsymbol{G}$ defined below respectively span the beamspace signal and noise subspaces.

$$\mathbf{S} = [\mathbf{s}_1, \ldots, \mathbf{s}_d] \qquad [4.20]$$

$$\mathbf{G} = [\mathbf{g}_{d+1}, \ldots, \mathbf{g}_{M'}] \qquad [4.21]$$

The UCA-RB-MUSIC spectrum

$$S_b(\boldsymbol{\theta}) = \frac{1}{\mathbf{a}_\mathbf{r}^T(\boldsymbol{\theta})\mathbf{G}\mathbf{G}^T\mathbf{a}_\mathbf{r}(\boldsymbol{\theta})} \propto \frac{1}{\mathbf{v}^H(\phi)\mathbf{J}(\zeta)\left[\mathbf{W}\mathbf{G}\mathbf{G}^T\mathbf{W}^H\right]\mathbf{J}(\zeta)\mathbf{v}(\phi)} \qquad [4.22]$$

has peaks at $\mathbf{8} = \mathbf{8}$; corresponding to the signal arrival directions. DOA estimates are therefore obtained by searching for d peaks in the two-dimensional UCA-RB-MUSIC spectrum. The major computations required by UCA-RB-MUSIC are a real-valued EVD of the matrix $\mathbf{R}$, and a two-dimensional search for peaks in the spectrum $S_b(\boldsymbol{\theta}) = S_b(\zeta, \mathbf{4})$. The elevation dependence of the spectrum is through the parameter $\zeta = k_0 r \sin\theta$, where θ is the elevation angle.

4.2.1 **Advantages** of UCA-RB-MUSIC

The UCA-RB-MUSIC algorithm offers many attractive features that art: not available in element space. All these features are available in beamspace because the azimuthal. dependence of the beamspace manifold $\mathbf{a_r}(\boldsymbol{\theta})$ of Equation 4.7 is through the vector $\mathbf{v}(\phi)$ whose form is similar to the ULA manifold vector. One advantage mentioned already is the computational savings due to the requirement of only a real-valued EVD. Other advantages include improved estimator performance due to FB averaging, applicability of Root-MUSIC, and the ability to perform coarse searches of the UCA-RB-MUSIC spectrum via an FFT. These features are discussed in further detail below.

Forward/Backward averaging in beamspace

As mentioned Section 4.1, the beamformer $\mathbf{F}_{\mathbf{e}}^H$ synthesizes the centro-Hermitian beamspace manifold $\mathbf{a_e}(\boldsymbol{\theta})$. Forward/Backward (FB) averaging is thus possible in beamspace: The corresponding FB averaged covariance matrix is $\mathbf{R}_{fb} = (\mathrm{R_e} + \tilde{\mathbf{I}}\mathbf{R}_{\mathbf{e}}^{*}\tilde{\mathbf{I}})/2$, where $\mathrm{R_e} = \mathbf{F}_{\mathbf{e}}^H\underline{\mathbf{R}}\mathbf{F_e}$ is the beamspace covariance matrix under the beamformer $\mathbf{F}_{\mathbf{e}}^H$. The property $\tilde{\mathbf{I}}\mathbf{W} = \mathbf{W}^*$ is employed in the manipulations below that show that the matrix $\mathbf{R} = \mathrm{Re}\{\mathbf{R_y}\}$ employed by UCA-RB-MUSIC is derived from the FB averaged covariance matrix $\mathbf{R}_{fb}$.

$$\mathbf{R} = \mathrm{Re}\{\mathbf{W}^H\mathbf{R_e}\mathbf{W}\} = \frac{1}{2}(\mathbf{W}^H\mathbf{R_e}\mathbf{W} + \mathbf{W}^T\mathbf{R}_{\mathbf{e}}^{*}\mathbf{W}^*) \quad [4.23]$$

$$= \frac{1}{2}\mathbf{W}^H(\mathbf{R_e} + \tilde{\mathbf{I}}\mathbf{R}_{\mathbf{e}}^{*}\tilde{\mathbf{I}})\mathbf{W} = \mathbf{W}^H\mathbf{R}_{fb}\mathbf{W}. \quad [4.24]$$

UCA-RB-MUSIC is thus endued with benefits associated with FB averaging, such as improved estimator performance in correlated source scenarios. FB type averaging can be performed in element space with a UCA when the number of array elements N is even; this property does not appear to have been exploited by researchers prior to this work. FB type averaging is possible for even N because the permuted version $\mathbf{J}\underline{\mathbf{a}}(\boldsymbol{\theta})$ of the element space manifold vector, with

$$\mathbf{J} = \begin{bmatrix} \mathbf{I}_{N/2} & \mathbf{0} \\ \mathbf{0} & \tilde{\mathbf{I}}_{N/2} \end{bmatrix},$$

is centro-Hermitian. However, such averaging is not possible in element space when N is odd. UCA-RB-MUSIC can thus outperform element space MUSIC when N is odd. The theoretical performance curves in Section 5.5 substantiate this claim.

Spectral Search via FFT

UCA-RB-MUSIC requires a search for peaks in the 2D spectrum of Equation 4.22 to obtain source azimuth and elevation estimates. This search is expedited by the fact that the computationally efficient FFT can be employed to evaluate the spectrum at each candidate elevation angle. Let $V(\phi;\zeta) = \mathbf{v}^H(\phi)\mathbf{J}(\zeta)\mathbf{W}\mathbf{G}\mathbf{G}^T\mathbf{W}^H\mathbf{J}(\zeta)\mathbf{v}(\phi)$ denote the UCA-RB-MUSIC null spectrum at the elevation specified by $\zeta = k_0 r \sin\theta$. With $\mathbf{Q}_\zeta = \mathbf{J}(\zeta)\mathbf{W}\mathbf{G}\mathbf{G}^T\mathbf{W}^H\mathbf{J}(\zeta)$, the null spectrum can be written in the form

$$V(\phi;\zeta) = \sum_{l=-(M'-1)}^{M'-1} a_\zeta(l)e^{jl\phi}, \text{ where } a_\zeta(l) = \sum_{i,j:j-i=l} \mathbf{Q}_\zeta(i,j). \qquad [4.25]$$

The matrix $\mathbf{Q}_\zeta$ is Hermitian such that $a_\zeta(-l) = a_\zeta^*(l)$. $V(\phi;\zeta)$ can thus be written in terms of the Discrete Time Fourier Transform of the M' point sequence $a'_\zeta = \{a_\zeta(0), 2a_\zeta(-1), \ldots, 2a_\zeta(-M'+1)\}$: We have $V(\phi;\zeta) = \text{Re}\{A'_\zeta(\phi)\}$, where $A'_\zeta(\phi) = \sum_{l=0}^{M'-1} a'_\zeta(l)e^{-jl\phi}$. The UCA-RB-MUSIC null spectrum $V(\phi;\zeta)$ at the elevation specified by [can thus be evaluated at L equispaced azimuth angles $\phi_l = 2\pi l/L$, I = 0, 1, ... L − 1 via an L point FFT of the sequence a'_ζ appropriately zero padded. In contrast, the search for peaks in the element space MUSIC spectrum cannot be expedited via an FFT.

Application of Root-MUSIC

The Root-MUSIC algorithm [Bar83] originally developed for use in conjunction with ULAs hinges on the Vandermonde structure of the ULA manifold. Root-MUSIC cannot be employed in element space with UCAs as the UCA manifold vectors $\underline{\mathbf{a}}(\boldsymbol{\theta})$ of Equation 3.1 are not Vandermonde. However, the azimuthal dependence of the UCA-RB-MUSIC null spectrum is through the vector $\mathbf{v}(\phi)$ of Equation 4.5 that is Vandermonde except for a multiplicative scale factor. Root-MUSIC can thus be employed in beamspace to obtain azimuth angles of sources at a given elevation. The Root-MUSIC formulation follows on setting $z = e^{j\phi}$ in Equation 4.25, and equating

the null spectrum $V(\phi;\zeta)$ to zero. The polynomial equation

$$a_\zeta(M'-1)z^{2M'-2} + a_\zeta(M'-2)z^{2M'-3} + \cdots + a_\zeta(-M'+1) = 0$$

results. Roots z_i of this equation which are close to the unit circle yield the azimuth estimates $\phi_i = \arg(z_i)$ of sources at the elevation ζ. UCA-RB-MUSIC thus benefits from the concomitant advantages of Root-MUSIC such as a lower failure rate for closely spaced sources at a given elevation.

Mapping onto ULA type manifold

Several researchers [Dav83, DD92] have considered the case where all incident sources are confined to a given elevation angle, say ζ_0, and the problem of interest is to estimate the source azimuth angles. It is clear from Equation 4.3 that the beamformer $\mathbf{F}_{ULA}^H(\zeta_0) = (1/\sqrt{N})\mathbf{J}^{-1}(\zeta_0)\mathbf{F}_\mathbf{e}^H$ maps the UCA manifold $\underline{\mathbf{a}}(\zeta_0,\phi)$ corresponding to the elevation ζ_0 onto the manifold $\mathbf{v}(\phi)$ of Equation 4.5. We have

$$\mathbf{F}_{ULA}^H(\zeta_0)\,\underline{\mathbf{a}}(\zeta_0,\phi) = \mathbf{v}(\phi), \qquad [4.26]$$

and the beamspace manifold corresponding to the elevation ζ_0 is similar to the ULA manifold. Using the beamformer $\mathbf{F}_{ULA}^H(\zeta_0)$ in such a scenario thus permits Spatial Smoothing [PK89a] to be employed in beamspace to combat the rank reducing effect caused by source coherency. Further, sinc type azimuthal patterns can be synthesized as with a ULA [ZM92, MZ92], and the Beamspace Root-MUSIC algorithm [ZKS93] can thus be employed. This algorithm allows for parallel sector-wise azimuthal searches for sources via rooting of reduced order polynomials.

4.2.2 UCA-RB-MUSIC: Algorithm Summary

1. Form the array sample covariance matrix $\hat{\underline{\mathbf{R}}} = \frac{1}{K}\sum_{t=1}^{K}\mathbf{x}(t)\mathbf{x}^H(t)$ by averaging over the K data snapshots. Also form the sample beamspace covariance matrix $\hat{\mathbf{R}}_\mathbf{y} = \mathbf{F}_\mathbf{r}^H\hat{\underline{\mathbf{R}}}\mathbf{F}_\mathbf{r}$.

2. Perform the real-valued EVD of the matrix $\mathrm{R} = \mathrm{Re}\{\hat{\mathbf{R}}_\mathbf{y}\}$, and apply an appropriate detection technique to get an estimate d of the number of sources. Let the

ordered eigenvalues of $\mathbf{R}$ be $\hat{\lambda}_1 \geq \cdots \geq \hat{\lambda}_{M'}$, and the corresponding orthonormal eigenvectors be $\hat{\mathbf{s}}_1, \ldots, \hat{\mathbf{s}}_{\hat{d}}, \hat{\mathbf{g}}_{\hat{d}+1}, \ldots, \hat{\mathbf{g}}_{M'}$. Form the matrices $\hat{\mathbf{S}} = [\hat{\mathbf{s}}_1, \ldots, \hat{\mathbf{s}}_{\hat{d}}]$ and $\mathrm{G} = [\hat{\mathbf{g}}_{\hat{d}+1}, \cdots, \hat{\mathbf{g}}_{M'}]$ that respectively span the estimated signal and noise subspaces.

3. Search for $\hat{d}$ peaks in the two-dimensional UCA-RB-MUSIC spectrum

$$\hat{S}_b(\theta) = \frac{1}{\mathbf{v}^H(\phi)\mathbf{J}(\zeta)[\mathbf{W}\hat{\mathbf{G}}\hat{\mathbf{G}}^T\mathbf{W}^H]\mathbf{J}(\zeta)\mathbf{v}(\phi)}. \qquad [4.27]$$

The peak locations $\hat{\boldsymbol{\theta}}_i = (k_0 r \sin\hat{\theta}_i, \hat{\phi}_i)$, $i = 1, \ldots, \hat{d}$ give the DOA estimates. As described earlier, use of the FFT facilitates this 2D spectral search.

4. If a good estimate of source elevation angle is available, Root-MUSIC can be employed to obtain the azimuth angle estimate as described earlier. Root-MUSIC can resolve sources at a given elevation and closely spaced in azimuth even if the UCA-RB-MUSIC spectrum reveals only a single peak in the vicinity.

4.2.3 Previous Work on Application of ULA Techniques with UCAs

As mentioned in Section 1.1, phase mode excitation based beamformers have been employed to synthesize attractive directional patterns with UCAs, and to obtain DOA estimates via the beamforming principle. Our initial work [ZM92, MZ92] focused on phase mode excitation based sinc-type pattern synthesis with UCAs (patterns similar to the cophasal ULA beam patterns). Root MUSIC was then employed to obtain azimuth angle estimates of sources at a given elevation. Other work on the application of ULA techniques with UCAs include that of Tewfik and Hong [TH92], and Friedlander and Weiss [FW92].

To compare UCA-RB-MUSIC with the work reported in [TH92], we recall that the rows of the matrix V^{H} (of Equation 4.1) that defines the beamforming matrix $\mathbf{F}_{\mathrm{e}}^{H'}$ are inverse DFT weight vectors. Row m $\in [-\mathrm{M}, M]$ of V^{H} excites the array with phase mode m, and a total of $M' = 2\mathrm{M} + 1 < \mathrm{N}$ modes are excited. Thus, only M' of the N possible phase modes are excited. The reason for choosing $M' < \mathrm{N}$ was to make the contributions of residual terms to the UCA far-field pattern negligible,

thus leading to a beamspace manifold whose azimuthal dependence is through the Vandermonde (except for a multiplicative scale factor) vector $\mathbf{v}(\phi)$. A full N x N inverse D'FT beamformer was employed in [TH92] to make the transformation from element space to beamspace. Some of the beams thus have significant contributions from residual terms, and this detracts from the desired Vandermonde structure. The approach proposed in [TH92] was to employ Root-MUSIC to obtain source azimuth estimates at each elevation angle under consideration. The imperfect Vandermonde structure however introduces errors in the estimates. The problem of elevation angle estimation was not addressed in [TH92].

Friedlitnder [FW92] proposed the interpolated array scheme that employs mapping matrices to map the manifold vectors for an arbitrary array onto Vandermonde ULA type steering vectors. The azimuthal field of view corresponding to each candidate elevation angle is divided into sectors, for each of which a different mapping matrix is designed. The interpolating matrix for a given sector is computed as the least squares solution of an overdetermined system of equations corresponding to the desired mapping. The link between the present work and the interpolated array technique is provided by Equation 4.26. It reveals that $\mathbf{F}_{ULA}^{H}(\zeta_0)$ is the desired mapping matrix that maps the element space UCA manifold $\underline{\mathbf{a}}(\zeta_0, \phi)$ corresponding to the elevation ζ_0 onto the ULA type manifold vector $\mathbf{v}(\phi)$. Phase mode analysis thus provides closed-form expressions for the mapping matrix for each elevation angle, and the mapping is valid for the entire 360° of azimuth.

4.3 Development of UCA-ESPRIT

The UCA-ESPRIT algorithm represents a significant advance in the area of 2D arrival angle estimation. It is a closed-form algorithm that provides automatically paired source azimuth and elevation angle estimates. In contrast, the algorithms for 2D arrival angle estimation to date have required expensive spectral searches [Sch86], iterative solutions to multi-dimensional optimization problems [CS91, SK93], or a pairing procedure for associating independently obtained direction cosine estimates

[ZS89]. The UCA-ESPRIT algorithm is fundamentally different from ESPRIT in that it is not based on the displacement invariance array structure required by ESPRIT [RK89]. The development of UCA-ESPRIT hinges rather on a recursive relationship between Bessel functions. The steps in the algorithm however, are similar to those of TLS-ESPRIT [RK89]. In the 1D angle estimation scenario, TLS-IESPRIT provides DOA estimates via the eigenvalues of a matrix. UCA-ESPRIT provides closed-form DOA estimates via matrix eigenvalues in the 2D angle estimation scenario: The eigenvalues have the form $\mu_i = \sin 8; e^{j\phi_i}$, and thus yield automaticisIly paired source azimuth and elevation angle estimates. Since $\theta_i \in [0, \pi/2]$, the eigenvalues satisfy $|\mu_i| \leq 1$, and lie within or on the unit circle. It is clear that $|\mu_i| = \sin\theta_i$, and $\arg(\mu_i) = \phi_i$ respectively specify the elevation and azimuth angles of the ith source without ambiguity. Note also that $\mu_i = u; + jv_i$, where $u_i = \sin\theta_i \cos\phi_i$, and $v_i = \sin\theta_i \sin\phi_i$ are respectively the direction cosines with respect to the x and y axes. Another similarity between UCA-ESPRIT and ESPRIT is the approximate halving (with respect to the size of the beamspace manifold) in the maximum number of resolvable sources. UCA-ESPRIT can resolve a maximum of $d_{max} = M - 1$ sources, roughly half the number resolvable with UCA-RB-MUSIC.

The beamformer $\mathbf{F}_{\mathbf{u}}^H$ of Equation 4.12 forms the basis for the development of UCIA-ESPRIT. The structure of the corresponding beamspace manifold a,(@) of Equation 4.13 is crucial to the development of the algorithm. We have

$$\mathbf{a_u}(\boldsymbol{\theta}) = \mathbf{F}_{\mathbf{u}}^H \underline{\mathbf{a}}(\boldsymbol{\theta}) = \sqrt{N} \begin{bmatrix} J_{-M}(\zeta)e^{-jM\phi} \\ \vdots \\ J_{-1}(\zeta)e^{-j\phi} \\ J_0(\zeta) \\ J_1(\zeta)e^{j\phi} \\ \vdots \\ J_M(\zeta)e^{jM\phi} \end{bmatrix} \qquad [4.28]$$

Consider extracting three subvectors of size $M_e = M' - 2$ from the beamspace manifold as follows: a; $= \boldsymbol{\Delta}_i \mathbf{a_u}(\boldsymbol{\theta})$, $i = -1, 0, 1$, where the M_e x M' selection matrices $\boldsymbol{\Delta}_{-1}, \boldsymbol{\Delta}_0$

and $\mathbf{\Delta}_1$ pick out the first, middle and last M_e elements from $\mathbf{a_u}(\boldsymbol{\theta})$. The property $J_{-m}(\zeta) = (-1)^m J_m(\zeta)$ of Bessel functions leads to the following relationship:

$$\begin{aligned} \mathbf{a}_1 &= \mathbf{D}\tilde{\mathbf{I}}\mathbf{a}^*_{-1}, \text{ where} \\ \mathbf{D} &= \text{diag}\{(-1)^{M-2}, \ldots, (-1)^1, (-1)^0, (-1)^1, \ldots, (-1)^M\}. \end{aligned} \quad [4.29]$$

The phases (excluding the signs of the values of the Bessel functions) of the vectors $\mathbf{a}_0, e^{j\phi}\mathbf{a}_{-1}$ and $e^{-j\phi}\mathbf{a}_1$ are the same. The recursive relationship $J_{m-1}(\zeta) + J_{m+1}(\zeta) = (2m/\zeta) J_m(\zeta)$ can now be applied to match the magnitude components of the three vectors. This leads to the critical relationship

$$\begin{aligned} \mathbf{\Gamma a}_0 &= \mu\mathbf{a}_{-1} + \mu^*\mathbf{a}_1 \\ &= \mu\mathbf{a}_{-1} + \mu^*\mathbf{D}\tilde{\mathbf{I}}\mathbf{a}^*_{-1}, \text{ where} \\ \mathbf{\Gamma} &= \frac{\chi}{\pi r} \text{diag}\{-(M-1), \ldots, -1, 0, 1, \ldots, M-1\}, \text{ and} \\ \mu &= \sin\theta\, e^{j\phi}. \end{aligned} \quad [4.30]$$

The partitions of the beamspace DOA matrix $\mathbf{A_u} = [\mathbf{a_u}(\boldsymbol{\theta}_1) \vdots \ldots \vdots \mathbf{a_u}(\boldsymbol{\theta}_d)]$ also satisfy the above property. Defining $A_i = \mathbf{\Delta}_i\mathbf{A_u}$, $i = -1, 0$, we obtain

$$\begin{aligned} \mathbf{\Gamma A}_0 &= \mathbf{A}_{-1}\mathbf{\Phi} + \mathbf{D}\tilde{\mathbf{I}}\mathbf{A}^*_{-1}\mathbf{\Phi}^*, \text{ where} \\ \mathbf{\Phi} &= \text{diag}\{\mu_1, \ldots, \mu_d\} = \text{diag}\{\sin\theta_1\, e^{j\phi_1}, \ldots, \sin\theta_d\, e^{j\phi_d}\}. \end{aligned} \quad [4.31]$$

The beamspace signal subspace matrix S, that spans $\mathcal{R}\{\mathbf{A_u}\}$ can be obtained via a complex-valued EVD of the beamspace covariance matrix $\mathbf{R}_u = \mathbf{F}_u^H \underline{\mathbf{R}} \mathbf{F_u}$. However, the relationship of Equation 4.16 allows S, to be expressed in terms of the signal subspace matrix S of Equation 4.20 that was obtained via a real-valued EVD. We have $\mathbf{A_u} = \mathbf{C_o W A_r} = \mathbf{C_o W S T}^{-1}$, where T is a d x d real-valued non-singular matrix. Thus

$$\mathbf{A_u} = \mathbf{S_u T}^{-1}, \text{ and S, } = \mathbf{C_o W S}. \quad [4.32]$$

The critical relationship (4.31) can now be expressed in terms of the partitions $\mathbf{S}_i = \mathbf{\Delta}_i\mathbf{S_u}$, i = $-1, 0$ of the signal subspace matrix S,. Substituting $\mathbf{A}_i = \mathbf{S}_i\mathbf{T}^{-1}$

in Equation 4.31, and using the fact that T is real-valued leads to the following relationship:

$$\begin{aligned} \mathbf{\Gamma S}_0 &= \mathbf{S}_{-1}\mathbf{\Psi} + \mathbf{D\tilde{I}S}^*_{-1}\mathbf{\Psi}^*, \text{ where} \\ \mathbf{\Psi} &= \mathbf{T}^{-1}\mathbf{\Phi T}. \end{aligned} \quad [4.33]$$

Writing in block matrix form yields the following system of equations:

$$\begin{aligned} \mathbf{E}\underline{\mathbf{\Psi}} &= \mathbf{\Gamma S}_0, \text{ where} \\ \mathbf{E} &= [\mathbf{S}_{-1} \vdots \mathbf{D\tilde{I}S}^*_{-1}], \text{ and} \\ \underline{\mathbf{\Psi}} &= \begin{bmatrix} \mathbf{\Psi} \\ \mathbf{\Psi}^* \end{bmatrix}. \end{aligned} \quad [4.34]$$

This system of equations is overdetermined when $M_e > 2$d i.e., d < M, and has a unique solution $\underline{\mathbf{\Psi}}$ or equivalently, $\mathbf{\Psi}$. From (4.33) we have $\mathbf{\Phi} = \mathbf{T\Psi T}^{-1}$, and the eigenvalues of $\mathbf{\Psi}$ are thus $\mu_i = \sin 8; e^{j\phi_i}, i = 1, \ldots,$ d. The eigenvalues of $\mathbf{\Psi}$ thus yield automatically paired source azimuth and elevation angles: We have 8; $= \sin^{-1}(|\mu_i|)$ and $\phi_i = \arg(\mathrm{p};)$. We point out that the eigenvalues μ_i can be obtained via a real-valued EVD in place of the complex-valued EVD of $\mathbf{\Psi} = \mathbf{\Psi}_R + j\mathbf{\Psi}_I$. We have $\mathbf{\Psi\Psi}^* = \mathbf{\Psi}_R^2 + \mathbf{\Psi}_I^2 = \mathbf{T}^{-1}\mathbf{\Phi\Phi}^*\mathbf{T}$, a real-valued matrix. The real-valued EVD of the matrix $\mathbf{\Psi}_R^2 + \mathbf{\Psi}_I^2$ thus yields the matrix T of eigenvectors, and $\mathbf{\Phi}$ is computed according to $\mathbf{\Phi} = \mathbf{T\Psi T}^{-1}$. UCA-ESPRIT cannot be employed when d $\geq$ M, and the system of Equation 4.34 is underdetermined. This is because the system possesses an infinity of solutions having the block conjugate structure of $\underline{\mathbf{\Psi}}$, as shown in Appendix C.2. The maximum number of sources that UCA-ESPRIT can resolve is thus $d_{max} = \mathrm{M} - 1$, where M is the maximum mode excited.

Under noisy conditions, the matrices $\hat{\mathbf{E}}$ and $\hat{\mathbf{S}}_0$ are formed using signal subspace estimates. The matrix $\underline{\hat{\mathbf{\Psi}}}$ is then obtained as the least squares (LS) solution to the overdetermined system

$$\hat{\mathbf{E}}\underline{\mathbf{\Psi}} = \mathbf{\Gamma}\hat{\mathbf{S}}_0. \quad [4.35]$$

Appendix C.1 shows that $\underline{\hat{\mathbf{\Psi}}}$ has block conjugate structure, as in the noise free case. The eigenvalues of the upper block $\hat{\mathbf{\Psi}}$ yield the source DOA estimates as described

earlier. Appendix C.1 also shows that the block conjugate structure leads to the following simplification in computing the LS solution. It allows the LS solution to be obtained by solving the system of 2d real equations below rather than solving a system of 2d complex equations as would otherwise be required.

$$\begin{bmatrix} (\mathbf{B}+\mathbf{C})_R & (\mathbf{C}-\mathbf{B})_I \\ (\mathbf{B}+\mathbf{C})_I & (\mathbf{B}-\mathbf{C})_R \end{bmatrix} \begin{bmatrix} \hat{\mathbf{\Psi}}_R \\ \hat{\mathbf{\Psi}}_I \end{bmatrix} = \begin{bmatrix} \mathbf{Q}_R \\ \mathbf{Q}_I \end{bmatrix}, \text{ where} \qquad [4.36]$$

$$\mathbf{B} = \hat{\bar{\mathbf{S}}}_{-1}^H \hat{\bar{\mathbf{S}}}_{-1}, \; \mathrm{C} = \hat{\mathbf{S}}_{-1}^H \mathbf{D}\tilde{\mathbf{I}}\hat{\mathbf{S}}_{-1}^*, \text{ and } \boldsymbol{Q} = \hat{\mathbf{S}}_{-1}^H \mathbf{\Gamma}\hat{\mathbf{S}}_0. \qquad [4.37]$$

The subscripts R and I in the above equation denote the real and imaginary parts, respectively.

UCA-ESPRIT is clearly superior to existing 2D angle estimation algorithms with respect to computational complexity. The significant computations required by UCA-ESPRIT include a real-valued EVD of the M' x M' matrix $\hat{\mathbf{R}}$, solution of the system (4.36) of 2d real equations, and a d $\times$ d EVD of the complex-valued matrix $\hat{\mathbf{\Psi}}$ (or a real-valued EVD of $\hat{\mathbf{\Psi}}_R^2 + \hat{\mathbf{\Psi}}_I^2$). Spectral searches, iterative optimization techniques, and the need to pair independently obtained direction cosine estimates are dispensed with. The simulations in Section 5.6 however show that the UCA-RB-MUSIC estimates have lower variances than the UCA-ESPRIT estimates. The UCA-ESPRIT estimates serve as good starting points for iterative Newton searches for peaks in the UCA-RB-MUSIC spectrum. The performance of UCA-RB-MUSIC can thus be realized at the additional cost of a Newton iteration if required.

4.3.1 UCA-ESPRIT: Algorithm Summary

1. Obtain the real-valued matrix $\mathbf{S}$ via Steps 1 and 2 in the algorithm summary of Section 4.2.2. Compute $\hat{\mathbf{S}}_\mathbf{u} = \mathbf{C_o}\mathbf{W}\hat{\mathbf{S}}$, where $\mathbf{C_o}$ is defined in Equation 4.15, and W is specified by either Equation 4.8 or Equation 4.10. Form the submatrices $\hat{\mathbf{S}}_i = \mathbf{\Delta}_i\hat{\mathbf{S}}_\mathbf{u}$, $i = -1, 0$, and construct the matrix $\mathrm{E} = [\hat{\mathbf{S}}_{-1} \vdots \mathbf{D}\tilde{\mathbf{I}}\hat{\mathbf{S}}_{-1}^*]$.

2. Obtain the least squares solution $\hat{\mathbf{\Psi}} = \hat{\mathbf{\Psi}}_R + j\hat{\mathbf{\Psi}}_I$ by solving the real-valued system of equations in (4.36).

3. Compute the eigenvalues $\hat{\mu}_i$, $i = 1 \ldots, d$ of . The eigenvalues $\hat{\mu}_i$ are the diagonal entries of the matrix $\hat{\mathbf{T}}\hat{\mathbf{\Psi}}\hat{\mathbf{T}}^{-1}$, where $\hat{\mathbf{T}}^{-1}$ is the real-valued matrix whose columns are the eigenvectors of $\hat{\mathbf{\Psi}}_R^2 + \hat{\mathbf{\Psi}}_I^2$. The estimates of the elevation and azimuth angles of the ith source are $\hat{\theta}_i = \sin^{-1}(|\hat{\mu}_i|)$ and $\hat{\phi}_i = \arg(\hat{\mu}_i)$, respectively. If direction cosine estimates are desired, we have $\hat{u}_i = \mathrm{Re}\{\hat{\mu}_i\}$, and $\hat{v}_i = \mathrm{Im}\{\hat{\mu}_i\}$.

4. DOA estimates of lower variance can be obtained by using the UCA-ESPRIT estimates from Step 3 as starting points for a Newton search for nearby maxima in the two-dimensional UCA-RB-MUSIC spectrum of Equation 4.27.

4.4 Mutual Coupling Effects

Mutual coupling effects can be quite significant with UCAs of omnidirectional elements [Dav83]. In the presence of mutual coupling, $\underline{\mathbf{a}}(\boldsymbol{\theta})$ of Equation 3.1 is no longer an accurate representation of the UCA manifold. The UCA manifold after incorporating mutual coupling effects is denoted $\underline{\mathbf{a}}_m(\boldsymbol{\theta})$. We have $\underline{\mathbf{a}}_m(\boldsymbol{\theta}) = \mathbf{Y}\underline{\mathbf{a}}(\boldsymbol{\theta})$, where Y is the mutual coupling matrix [RW92]. At first glance it; appears that all the phase mode excitation developments are inapplicable due to the presence of Y. However it is well known [Dav83] that exciting a UCA with phase mode m synthesizes the same phase mode in the far-field pattern even when mutual coupling effects apply. A change in the corresponding mode amplitude in the far-field pattern is the only effect of mutual coupling. As a consequence of this property, UCA-RB-MUSIC and UCA-ESPRIT are easily adapted to account for mutual coupling efects. Accounting for mutual coupling with a UCA turns out to be much simpler than with other array geometries (see [FW91]).

Before proceeding to discuss the modifications required to adapt the algorithms to cope with mutual coupling, we provide a proof of the above mentioned property. The matrix V^{H} defined in Equation 4.1 excites the UCA with the appropriate phase

modes, and the relationship to be proved is

$$\mathbf{V}^H \underline{\mathbf{a}}_m(\theta) = \mathbf{V}^H \mathbf{Y} \underline{\mathbf{a}}(\theta) = \mathbf{\Lambda}_y \mathbf{V}^H \underline{\mathbf{a}}(\theta), \qquad [4.38]$$

where A, is a diagonal matrix whose entries represent the change in far-field mode amplitude due to mutual coupling. The mutual coupling matrix Y is circulant due to circular symmetry of the UCA. Let $\boldsymbol{y}^T$ be the first row of Y: we have $\boldsymbol{y}^T = \{y_0, y_1, y_2, y_1\}$ for a four element UCA. It is well known [Dav79] that the DFT (Discrete Fourier Transform) matrix diagonalizes any circulant matrix; the IDFT (Inverse DFT) matrix thus gives the left eigenvectors of any circulant matrix. As mentioned in Section 4.1, the M' rows of the matrix V^{H} are a subset of the N IDFT weight vectors. We therefore have

$$\mathbf{V}^H \mathbf{Y} = \mathbf{\Lambda}_y \mathbf{V}^H, \text{ where} \qquad [4.39]$$

$$\mathbf{\Lambda}_y = \text{diag}\{\lambda_{-M}, \ldots, \lambda_0, \ldots, \lambda_M\} \qquad [4.40]$$

is the diagonal matrix whose entries are the appropriate subset of eigenvalues of Y. These equations prove the assertion in (4.38). We also point out that the eigenvalue of Y associated with the ith column of the DFT matrix (or the ith row of the IDFT matrix) is just the ith element in the DFT of the sequence $\boldsymbol{y}^T$.

From Equation 4.38 it is evident that the beamformers

$$\mathbf{F}_{\mathbf{em}}^H = \mathbf{\Lambda}_y^{-1} \mathbf{F}_{\mathbf{e}}^H, \; \mathbf{F}_{\mathbf{rm}}^H = \mathbf{W}^H \mathbf{F}_{\mathbf{em}}^H, \text{ and } \mathbf{F}_{\mathbf{um}}^H = \mathrm{Ah}; ^1 \mathbf{F}_{\mathbf{u}}^{\mathbf{H}} \qquad [4.41]$$

respectively synthesize the beamspace manifolds a, (O), a, (O), and a, (θ) of Section 4.1. It is clear that both UCA-RB-MUSIC and UCA-ESPRIT can be applied in conjunction with the above beamformers. However, there are slight differences in the implementation of the algorithms as $\mathbf{F}_{\mathbf{rm}}^H$ is not an orthogonal beamformer. With a being the power of the spatially white element space noise, the beamspace noise covariance matrix is $\mathbf{R}_{\mathrm{n}} = \sigma \mathbf{F}_{\mathbf{rm}}^H \mathbf{F}_{\mathbf{rm}} = \sigma \mathbf{W}^H |\mathbf{\Lambda}_y|^{-2} \mathbf{W}$, a real-valued, Toeplitz matrix. Since the beamspace noise is non-white, a generalized eigenvalue decomposition (GEVD) is required to obtain signal eigenvector estimates. The steps involved in

adapting UCA-RB-MUSIC and UCA-ESPRIT to cope with mutual coupling effects are summarized below. The mutual coupling matrix Y can be obtained experimentally or via theoretical analysis.

4.4.1 Incorporation of Mutual Coupling Effects: Algorithm Summary

1. Let A; denote the ith bin of the DFT of the vector $\mathbf{y}^T$ that specifies the first row of the mutual coupling matrix Y. Using the fact that $\lambda_{-i} = \lambda_{N-i}$, form the matrix A, $= \text{diag}\{\lambda_{-M}, \ldots, \lambda_0, \ldots, \lambda_M\}$.

2. Form the sample beamspace covariance matrix $\hat{\mathbf{R}}_\mathbf{y} = \mathbf{F}_{\mathbf{rm}}^H \hat{\underline{\mathbf{R}}} \mathbf{F}_{\mathbf{rm}}$, where $\mathbf{F}_{\mathbf{rm}}^H = \mathrm{W}^{\mathrm{H}} \mathbf{\Lambda}_y^{-1} \mathbf{F}_\mathbf{e}^H$. The beamformer $\mathbf{F}_\mathbf{e}^H$ is defined in Equation 4.2.

3. Perform the real-valued GEVD of $\hat{\mathbf{R}} = \text{Re}\{\hat{\mathbf{R}}_\mathbf{y}\}$ in the metric of $\mathbf{W}^H |\mathbf{\Lambda}_y|^{-2} \mathbf{W}$. Obtain an estimate $\hat{d}$ of the number of sources, and form the matrices $\hat{\mathbf{S}} = [\hat{\mathbf{s}}_1, \ldots, \hat{\mathbf{s}}_{\hat{d}}]$ and $\boldsymbol{G} = [\hat{\mathbf{g}}_{\hat{d}+1}, \cdot \cdot, \hat{\mathbf{g}}_{M'}]$ by grouping the $\hat{d}$ "largest" and $M' - \mathrm{d}$ "smallest" generalized eigenvectors.

4. Use the matrices $\hat{\mathbf{S}}$ and $\boldsymbol{G}$ from the previous step in the algorithm summaries of Sections 4.2.2 and 4.3.1 for UCA-RB-MUSIC and UCA-ESPRIT, respectively.

4.5 Extensions for Directional Elements

The developments to this point assumed that the UCA consisted of omnidirectional elements. We now consider the case where the UCA employs directional elements disposed such that circular symmetry is retained. Rahim et al. [RD82] obtained expressions for the far-field patterns of UCAs of directional elements under phase mode excitation: They showed that the far-field pattern still has the same azimuthal variation $e^{jm\phi}$ as the excitation function. However, the amplitude of the phase mode in the far-field pattern is a sum of Bessel functions rather than just $J_m(\zeta)$. One of the advantages of using directional elements is that attractive azimuthal directional patterns can be synthesized over wide frequency ranges (over an octave). Consider

azimuthal pattern synthesis in the array plane ($8 = 90°$): With omnidirectional elements, the mode amplitude $J_m(2\pi r/\lambda)$ undergoes rapid variations and passes through nulls as λ is varied. This is not suitable for pattern synthesis, as non-zero mode amplitudes are required. With directional elements, the mode amplitude is a sum of Bessel functions, and is observed to be stable over wide frequency ranges. Another advantage of using directional elements is that mutual coupling effects (specifically diametrical coupling across the array) are mitigated in arrays of small radius.

Let $g(\theta, \phi)$ represent the directional response of an individual antenna element. The UCA of directional elements is characterized by the element space manifold

$$\begin{aligned} \underline{\mathbf{a}}_d(\boldsymbol{\theta}) &= \mathbf{G}_{\boldsymbol{\theta}}\underline{\mathbf{a}}(\boldsymbol{\theta}), \text{ where} \\ \mathbf{G}_{\boldsymbol{\theta}} &= \text{diag}\{g(\theta, 4 - \gamma_0), \ldots, g(\theta, \phi - \gamma_{N-1})\}, \end{aligned} \quad [4.42]$$

and $\gamma_i = 2\pi i/N$ is the angular position of the ith element. First consider the case where the element pattern is only elevation dependent (omnidirectional in azimuth). With the element pattern denoted $g(\theta)$, the corresponding UCA manifold is $\underline{\mathbf{a}}_d(\boldsymbol{\theta}) = g(\theta)\underline{\mathbf{a}}(\boldsymbol{\theta})$, a scalar multiple of the omnidirectional UCA manifold. The element space data vector thus has the representation $\mathbf{x}(t) = \underline{\mathbf{A}}\mathbf{s}'(t) + \mathbf{n}(t)$, where $\mathrm{s}'(\mathrm{t}) = \mathbf{G}_\theta\mathbf{s}(t)$, and $\mathbf{G}_\theta = \text{diag}\{g(\theta_1), \ldots, g(\theta_d)\}$. It is evident that UCA-RB-MUSIC and UCA-ESPRIT are both applicable in this scenario – the only change is that the source covariance matrix $\mathbf{P}$ is replaced by $\mathbf{P}_d = \mathbf{G}_\theta\mathbf{P}\mathbf{G}_\theta^H$.

Now consider the general case where the element pattern is a function of both azimuth and elevation. Let $g(\phi; 8) = \sum_{k=-p}^{p} c_\theta(k)e^{jk\phi}$ be the Fourier series expansion for the azimuthal variation of the element pattern at the elevation 8. The far-field pattern (ignoring residual terms) resulting from excitation of the UCA of directional elements with phase mode m is [RD82]

$$\begin{aligned} f_m^s(\boldsymbol{\theta}) &= \mathbf{w}_m^H\underline{\mathbf{a}}_d(\boldsymbol{\theta}) \approx A_m(\theta)e^{jm\phi}, \text{ where} \\ A_m(\theta) &= \sum_{\mathrm{k=-p}}^{\mathrm{P}} c_\theta(k)j^{m-k}J_{m-k}(k_0 r \sin 8). \end{aligned} \quad [4.43]$$

This equation is similar to Equation 3.12 for the omnidirectional element case. The only difference is that the mode amplitude $A_m(\theta)$ involves a sum of Bessel functions,

and is not just $J_m(\zeta)$. The mode amplitudes are easily shown to satisfy $A_{-m}(\theta) = A_m(\theta)$. An element pattern suggested in [RD82] is $g(\theta, \phi) = 1 + \sin\theta\cos\phi$: The mode amplitudes corresponding to this pattern are $A_m(\theta) = j^m[J_m(<) - j\sin\theta J'_m(\zeta)]$, where $\zeta = k_0 r$ sine. From Equation **4.43,** it is evident that the beamformer V^H of Equation 4.1 synthesizes the beamspace manifold

$$\begin{aligned} \mathbf{a}_d(\boldsymbol{\theta}) &= \mathbf{V}^H \underline{\mathbf{a}}_d(\boldsymbol{\theta}) = \mathbf{J}_d(\theta)\mathbf{v}(\phi), \text{ where} \\ \mathbf{J}_d(\theta) &= \text{diag}\{A_M(\theta), \ldots, A_1(\theta), A_0(\theta), A_1(\theta), \ldots, A_M(\theta)\}. \end{aligned} \quad [4.44]$$

The azimuthal dependence of the beamspace manifold $\mathbf{a}_d(\boldsymbol{\theta})$ is through the vector $\mathbf{v}(\phi)$, as was the case with UCA-RB-MUSIC. The beamspace MUSIC algorithm (employing the beamformer V^H) for the UCA of directional elements thus possesses most of the features of UCA-RB-MUSIC. The features that are lost are the ability to perform FB averaging, and to compute signal eigenvectors via a real-valued EVD. This is because the beamspace manifold $\mathbf{a}_d(\boldsymbol{\theta})$ is not centro-Hermitian. UCA-ESPRIT cannot be employed when the elements have directional patterns that are functions of both azimuth and elevation. This is because the components of $\mathbf{J}_d(\theta)$ are sums of Bessel functions, and the recursive Bessel function relationship cannot be employed to match the magnitude components of the subvectors of $\mathbf{a}_d(\boldsymbol{\theta})$.

5. PERFORMANCE ANALYSIS

The statistical performance of element space MUSIC, UCA-RB-MUSIC, and UCA-ESPRIT is investigated in this chapter. Asymptotic expressions for the variances and covariances of the element space MUSIC estimators for 2D angle estimation are presented in Section 5.1. Such performance analysis results are available for the 1D angle estimation case [SN89]. However the present work appears to be the first time such results have been made available for the case of 2D angle estimation. Section 5.2 considers the performance of the UCA-RB-MUSIC algorithm. With UCA-RB-MUSIC, signal subspace estimates are obtained via real-valued EVDs, and the analysis differs from that of element space MUSIC in this respect. The final results, however, are similar in form to those for element space MUSIC. The statistical performance of UCA-ESPRIT is investigated in Section 5.3. The analysis is similar to that of the ESPRIT algorithm for 1D angle estimation [RH89a]. Section 5.4 presents results on the Cramer-Rao bound (CRB) for the 2D angle estimation problem. Finally, the performance of the algorithms for the one and two sources cases is investigated in some detail in Section 5.5. It has been shown [SN91] that beamspace MUSIC estimators cannot perform better than the corresponding element space MUSIC estimators. However, FB averaging is possible in beamspace and not possible in element space when the number of array elements N is odd. UCA-RB-MUSIC can thus outperform element space MUSIC when N is odd. The theoretical performance curves of Section 5.5 demonstrate this property.

Before beginning the analysis, we restate some of the assumptions made, and introduce some notation. The number of incident signals d is assumed to be known. The signals $\mathbf{s}(t)$ and noises $\mathbf{n}(t)$ are assumed to be stationary, zero mean, uncorrelated random processes. The noise process $\mathbf{n}(t)$ is assumed to be complex Gaussian

and spatially white with covariance matrix $\sigma\mathbf{I}$. The signals are assumed to be non-coherent, and the source covariance matrix $\mathbf{P}$ is thus positive definite. The number of snapshots of array data is K. The dimension of the element space UCA manifold is N, and the dimension of the real-valued beamspace manifold is M'. UCA-RB-MUSIC works with subspace estimates obtained via an EVD of the real matrix $\mathbf{R}$ of Equation 4.19. The eigenvalues of $\mathbf{R}$ in descending order are $\{\lambda_i\}_{i=1}^{M'}$. The real, orthonormal matrices $\mathbf{S}$ and $\mathbf{G}$ that respectively span the beamspace signal and noise subspaces are defined in Equations 4.20 and 4.21. The same symbol is used to denote similar quantities in element space and beamspace; the element space quantities are distinguished by underbars e.g., $\mathbf{S}$ and $\underline{\mathbf{S}}$ respectively span the beamspace and element space signal subspaces. Hats are used to denote estimated values of quantities e.g., $\hat{\boldsymbol{G}}$. In this chapter, subscripts are used to denote partial derivatives e.g., $\mathbf{b}_\zeta$ and $\mathbf{b}_{\zeta\phi}$ respectively represent the first partial derivative of $\mathbf{b}$ with respect to ζ, and the mixed partial derivative with respect to ζ and ϕ.

5.1 Performance of MUSIC for 2D Angle Estimation

Theorem 5.1.1 gives asymptotic (large number of snapshots K) expressions for the variances and covariances of the element space MUSIC estimator for 2D angle estimation. The results of the theorem hold for arbitrary array configurations. The following lemma gives asymptotic expressions for the errors in the element space MUSIC arrival angle estimates. The proof of the lemma is based on a first order Taylor series expansion of the MUSIC null spectrum about the true parameter values, and is similar to the proof of Lemma 5.2.1 in Section 5.2. The only difference is that the manifold vectors and subspace matrices are complex-valued in element space, whereas they are real-valued in beamspace.

Lemma **5.1.1** The asymptotic expression for the element space MUSIC estimation error vector, $\underline{\mathbf{e}}_i = [(\hat{\underline{\zeta}}_i - \zeta_i), (\hat{\underline{\phi}}_i - \phi_i)]^T$, for source i is

$$\underline{\mathbf{e}}_i = \left\{\underline{\hat{\mathbf{E}}}^{-1}\underline{\mathbf{p}}\right\}_{\boldsymbol{\theta}=\boldsymbol{\theta}_i}, \text{ where} \qquad [5.1]$$

$$\underline{\mathbf{E}} = \begin{bmatrix} \underline{\mathbf{a}}_\zeta^H \underline{\mathbf{G}}\underline{\mathbf{G}}^H \underline{\mathbf{a}}_\zeta & \mathrm{Re}\{\underline{\mathbf{a}}_\phi^H \underline{\mathbf{G}}\underline{\mathbf{G}}^H \underline{\mathbf{a}}_\zeta\} \\ \mathrm{Re}\{\underline{\mathbf{a}}_\phi^H \underline{\mathbf{G}}\underline{\mathbf{G}}^H \underline{\mathbf{a}}_\zeta\} & \underline{\mathbf{a}}_\phi^H \underline{\mathbf{G}}\underline{\mathbf{G}}^H \underline{\mathbf{a}}_\phi \end{bmatrix} = \begin{bmatrix} \underline{a} & \underline{c} \\ \underline{c} & \underline{b} \end{bmatrix}$$

is a symmetric, positive definite matrix with determinant $\underline{\Delta}$. The vector

$$\underline{\mathbf{p}} = \begin{bmatrix} -\mathrm{Re}\{\underline{\mathbf{a}}^H \hat{\underline{\mathbf{G}}}\hat{\underline{\mathbf{G}}}^H \underline{\mathbf{a}}_\zeta\} \\ -\mathrm{Re}\{\underline{\mathbf{a}}^H \hat{\underline{\mathbf{G}}}\hat{\underline{\mathbf{G}}}^H \underline{\mathbf{a}}_\phi\} \end{bmatrix} = \begin{bmatrix} \underline{e} \\ \underline{f} \end{bmatrix}$$

is a random vector.

Although the MUSIC estimation errors are in terms of the matrix $\hat{\underline{\mathbf{G}}}$ that spans the estimated noise subspace, knowledge of the statistics of the signal space eigenvectors is sufficient to obtain expressions for the variances of the DOA estimators. The following lemma gives the well known result [SN89] on the statistics of the signal space eigenvectors of the element space sample covariance matrix $\hat{\underline{\mathbf{R}}}$ that is complex Wishart distributed with K degrees of freedom.

Lemma 5.1.2 The element space signal eigenvector estimation errors, $(\hat{\underline{\mathbf{s}}}_i - \underline{\mathbf{s}}_i)$, are asymptotically jointly Gaussian distributed with zero means. The error covariance matrices are given by

$$E\left[(\hat{\underline{\mathbf{s}}}_i - \underline{\mathbf{s}}_i)(\hat{\underline{\mathbf{s}}}_j - \underline{\mathbf{s}}_j)^H\right] = \frac{\underline{\lambda}_i}{K}\left[\sum_{\substack{r=1 \\ r\neq i}}^{d} \frac{\underline{\lambda}_r}{(\underline{\lambda}_r - \underline{\lambda}_i)^2}\underline{\mathbf{s}}_r\underline{\mathbf{s}}_r^H + \sum_{r=d+1}^{N} \frac{\sigma}{(\underline{\lambda}_i - \sigma)^2}\underline{\mathbf{g}}_r\underline{\mathbf{g}}_r^H\right]\delta_{ij} \quad [5.2]$$

The following theorem gives expressions for the variances and covariance of the element space MUSIC arrival angle estimators $\hat{\underline{\zeta}}_i$ and $\hat{\underline{\phi}}_i$ corresponding to the ith source. The proof of the theorem employs Lemmas 5.1.1 and 5.1.2, and is similar to tht: proof of Theorem 5.2.1 in the Section 5.2.

Theorem 5.1.1 The element space MUSIC estimation error vector $\underline{\mathbf{e}}_i = [(\hat{\underline{\zeta}}_i - \zeta_i), (\hat{\underline{\phi}}_i - \phi_i)]^T$ for the ith source is asymptotically zero mean with covariance matrix

$$\mathbf{Cov}\,(\underline{\mathbf{e}}_i) = \begin{bmatrix} Var & Cov(\hat{\underline{\zeta}}_i, \hat{\underline{\phi}}_i) \\ Cov(\hat{\underline{\zeta}}_i, \hat{\underline{\phi}}_i) & Var(\hat{\underline{\phi}}_i) \end{bmatrix} = \frac{\sigma\underline{\rho}}{2K\underline{\Delta}}\begin{bmatrix} \underline{b} & \underline{c} \\ \underline{c} & \underline{a} \end{bmatrix}_{\boldsymbol{\theta}=\boldsymbol{\theta}_i} \quad [5.3]$$

where $\underline{a}, \underline{b}, \underline{c}$, and $\underline{\Delta}$ are as defined in Lemma **5.1.1.** Two expressions for the factor $\underline{p}$ follow. The latter expression is useful for analytical studies of performance.

$$\begin{aligned} \underline{\rho}(\boldsymbol{\theta}_i) &= \sum_{r=1}^{d} \frac{\underline{\lambda}_r}{(\underline{\lambda}_r - \sigma)^2} |\underline{\mathbf{a}}^H(\boldsymbol{\theta}_i)\underline{\mathbf{s}}_r|^2 \\ &= \left[\mathbf{P}^{-1}\right]_{ii} + \sigma \left[\mathbf{P}^{-1}\left(\underline{\mathbf{A}}^H\underline{\mathbf{A}}\right)^{-1}\mathbf{P}^{-1}\right]_{ii} \end{aligned} \quad [5.4]$$

5.2 Performance Analysis of UCA-RB-MUSIC

Theorem **5.2.1** gives asymptotic (large number of snapshots K) expressions for the variances and covariances of the UCA-RB-MUSIC estimators. To avoid double subscripts, the symbols $\mathbf{b}(\boldsymbol{\theta}) = \mathbf{a_r}(\boldsymbol{\theta})$ and B = A, are used to respectively represent the beamspace manifold vector and the beamspace DOA matrix. The following lemma gives asymptotic expressions for the errors in the UCA-RB-MUSIC arrival angle estimates.

Lemma **5.2.1** The asymptotic expression for the UCA-RB-MUSIC estimation error vector, $\mathbf{e}_i = [(\hat{\zeta}_i - \zeta_i), (\hat{\phi}_i - \phi_i)]^T$, for source i is

$$\mathbf{e}_i = \left\{\mathbf{E}^{-1}\mathbf{p}\right\}_{\boldsymbol{\theta}=\boldsymbol{\theta}_i}, \text{ where} \quad [5.5]$$

$$\mathbf{E} = \begin{bmatrix} \mathbf{b}_\zeta^T\mathbf{G}\mathbf{G}^T\mathbf{b}_\zeta & \mathbf{b}_\phi^T\mathbf{G}\mathbf{G}^T\mathbf{b}_\zeta \\ \mathbf{b}_\phi^T\mathbf{G}\mathbf{G}^T\mathbf{b}_\zeta & \mathbf{b}_\phi^T\mathbf{G}\mathbf{G}^T\mathbf{b}_\phi \end{bmatrix} = \begin{bmatrix} a & c \\ c & b \end{bmatrix}$$

is a symmetric, positive definite matrix with determinant **A.** The vector

$$\mathbf{p} = \begin{bmatrix} -\mathbf{b}^T\hat{\mathbf{G}}\hat{\mathbf{G}}^T\mathbf{b}_\zeta \\ -\mathbf{b}^T\hat{\mathbf{G}}\hat{\mathbf{G}}^T\mathbf{b}_\phi \end{bmatrix} = \begin{bmatrix} e \\ f \end{bmatrix}$$

is a random vector.

Proof: The UCA-RB-MUSIC null spectrum is $V(\boldsymbol{\theta}) = \mathbf{b}^T(\boldsymbol{\theta})\hat{\mathbf{G}}\hat{\mathbf{G}}^T\mathbf{b}(\boldsymbol{\theta})$. The null spectrum has a local minimum at $\hat{\boldsymbol{\theta}}_i = (\hat{\zeta}_i, \hat{\phi}_i)$ and we thus have $V_\zeta(\hat{\boldsymbol{\theta}}_i) = 0$, and $V_\phi(\hat{\boldsymbol{\theta}}_i) = 0$. Now, $\hat{\boldsymbol{\theta}}_i$ is a consistent estimator of $\boldsymbol{\theta}_i$, and a first order Taylor series expansion yields the following:

$$\begin{aligned} 0 &= V_\zeta(\hat{\boldsymbol{\theta}}_i) \approx V_\zeta(\boldsymbol{\theta}_i) + V_{\zeta\zeta}(\boldsymbol{\theta}_i)(\hat{\zeta}_i - \zeta_i) + V_{\zeta\phi}(\boldsymbol{\theta}_i)(\hat{\phi}_i - \phi_i) \\ 0 &= V_\phi(\hat{\boldsymbol{\theta}}_i) \approx V_\phi(\boldsymbol{\theta}_i) + V_{\phi\zeta}(\boldsymbol{\theta}_i)(\hat{\zeta}_i - \zeta_i) + V_{\phi\phi}(\boldsymbol{\theta}_i)(\hat{\phi}_i - \phi_i) \end{aligned}$$

Putting these equations into matrix form, we obtain

$$\begin{bmatrix} V_{\zeta\zeta}(\boldsymbol{\theta}_i) & V_{\zeta\phi}(\boldsymbol{\theta}_i) \\ V_{\phi\zeta}(\boldsymbol{\theta}_i) & V_{\phi\phi}(\boldsymbol{\theta}_i) \end{bmatrix} \begin{bmatrix} (\hat{\zeta}_i - \zeta_i) \\ (\hat{\phi}_i - \phi_i) \end{bmatrix} = - \begin{bmatrix} V_{\zeta}(\boldsymbol{\theta}_i) \\ V_{\phi}(\boldsymbol{\theta}_i) \end{bmatrix}. \qquad [5.6]$$

The expansions for the derivatives occurring in this equation are as given below. Only terms which result in contributions of order $O(1/N)$ in Equation 5.6 are retained.

$$\begin{aligned} V_{\zeta}(\boldsymbol{\theta}_i) &= 2\mathbf{b}^T(\boldsymbol{\theta}_i)\hat{\mathbf{G}}\hat{\mathbf{G}}^T\mathbf{b}_{\zeta}(\boldsymbol{\theta}_i) \\ V_{\phi}(\boldsymbol{\theta}_i) &= 2\mathbf{b}^T(\boldsymbol{\theta}_i)\hat{\mathbf{G}}\hat{\mathbf{G}}^T\mathbf{b}_{\phi}(\boldsymbol{\theta}_i) \\ V_{\zeta\zeta}(\boldsymbol{\theta}_i) &= 2\mathbf{b}_{\zeta}^T(\boldsymbol{\theta}_i)\hat{\mathbf{G}}\hat{\mathbf{G}}^T\mathbf{b}_{\zeta}(\boldsymbol{\theta}_i) + 2\mathbf{b}^T(\boldsymbol{\theta}_i)\hat{\mathbf{G}}\hat{\mathbf{G}}^T\mathbf{b}_{\zeta\zeta}(\boldsymbol{\theta}_i) \\ &\approx 2\mathbf{b}_{\zeta}^T(\boldsymbol{\theta}_i)\mathbf{G}\mathbf{G}^T\mathbf{b}_{\zeta}(\boldsymbol{\theta}_i) \\ V_{\phi\phi}(\boldsymbol{\theta}_i) &= 2\mathbf{b}_{\phi}^T(\boldsymbol{\theta}_i)\hat{\mathbf{G}}\hat{\mathbf{G}}^T\mathbf{b}_{\phi}(\boldsymbol{\theta}_i) + 2\mathbf{b}^T(\boldsymbol{\theta}_i)\hat{\mathbf{G}}\hat{\mathbf{G}}^T\mathbf{b}_{\phi\phi}(\boldsymbol{\theta}_i) \\ &\approx 2\mathbf{b}_{\phi}^T(\boldsymbol{\theta}_i)\mathbf{G}\mathbf{G}^T\mathbf{b}_{\phi}(\boldsymbol{\theta}_i) \\ V_{\zeta\phi}(\boldsymbol{\theta}_i) &= 2\mathbf{b}_{\phi}^T(\boldsymbol{\theta}_i)\hat{\mathbf{G}}\hat{\mathbf{G}}^T\mathbf{b}_{\zeta}(\boldsymbol{\theta}_i) + 2\mathbf{b}^T(\boldsymbol{\theta}_i)\hat{\mathbf{G}}\hat{\mathbf{G}}^T\mathbf{b}_{\zeta\phi}(\boldsymbol{\theta}_i) = V_{\phi\zeta}(\boldsymbol{\theta}_i) \\ &\approx 2\mathbf{b}_{\phi}^T(\boldsymbol{\theta}_i)\mathbf{G}\mathbf{G}^T\mathbf{b}_{\zeta}(\boldsymbol{\theta}_i) \end{aligned}$$

Substituting these expressions back into Equation 5.6 and dropping the common factor of two leads to the desired result $\mathbf{E}\mathbf{e}_i = \mathrm{p}$, where E, e;, and p are as defined in the lemma. Positive definitiveness and hence non-singularity of E follow from the Cauchy-Schwarz inequality.

UCA-RB-MUSIC works with subspace estimates obtained from the real matrix $\mathrm{R} = \mathrm{Re}\{\hat{\mathbf{R}}_{\mathbf{y}}\}$ that is derived from a FB averaged covariance matrix. The statistics of the signal space eigenvectors of R are required for the analysis of UCA-RB-MUSIC. The following lemma drawn from [ZK92] gives these statistics.

Lemma 5.2.2 The real beamspace signal eigenvector estimation errors, $(\hat{\mathbf{s}}_i - \mathrm{s};)$, are asymptotically (large K) zero mean with covariance matrices given by

$$E\left[(\hat{\mathbf{s}}_i - \mathbf{s}_i)(\hat{\mathbf{s}}_j - \mathbf{s}_j)^T\right] = \frac{1}{K}\left[\sum_{\substack{r=1 \\ r\neq i}}^{d}\sum_{\substack{s=1 \\ s\neq j}}^{d} \frac{\Gamma_{rsji}}{(\lambda_i - \lambda_r)(\lambda_j - \lambda_s)}\mathbf{s}_r\mathbf{s}_s^T + \delta_{ij}\sum_{r=d+1}^{M'} \frac{\lambda_i\sigma}{2(\lambda_i - \sigma)^2}\mathbf{g}_r\mathbf{g}_r^T\right] \qquad [5.7]$$

where

$$\Gamma_{rsji} = \frac{1}{2}\left\{\lambda_i\lambda_s\delta_{ij}\delta_{rs} + \lambda_i\lambda_j\delta_{is}\delta_{jr} + \mathbf{w}_r^T(\mathbf{s}_s\mathbf{s}_j^T + \mathbf{s}_j\mathbf{s}_s^T)\mathbf{w}_i\right\}, \text{ and } \mathbf{w}_i = \text{Im}\{\mathbf{R_y}\}\mathbf{s}_i.$$

The following theorem gives expressions for the variances and covariance of the UCA-RB-MUSIC arrival angle estimators ζ_i and ϕ_i corresponding to the ith source. The results are similar in form to those of Theorem 5.1.1 corresponding to the element space case. However, due to the inherent FB average, the results depend only on the real part $\mathbf{P}_R$ of the source covariance matrix P. The decorrelating effect of the FB average allows UCA-RB-MUSIC to outperform element space MUSIC in correlated source scenarios when N is odd.

Theorem 5.2.1 The UCA-RB-MUSIC estimation error vector $\mathbf{e}_i = [(\hat{\zeta}_i - \zeta_i), (\hat{\phi}_i - \phi_i)]^T$ for the ith source is asymptotically zero mean with covariance matrix

$$Cov(\mathbf{e}_i) = \begin{bmatrix} Var(\hat{\zeta}_i) & Cov(\hat{\zeta}_i, \hat{\phi}_i) \\ Cov(\hat{\zeta}_i, \hat{\phi}_i) & Var(\hat{\phi}_i) \end{bmatrix} = \frac{\sigma\rho}{2K\Delta}\begin{bmatrix} b & c \\ c & a \end{bmatrix}_{\boldsymbol{\theta}=\boldsymbol{\theta}_i} \quad [5.8]$$

where a, b, c, and A are as defined in Lemma 5.2.1. Two expressions for the factor ρ follow. In the latter expression, which is useful for analytical studies of performance, $\mathbf{P}_R = \text{Re}\{\mathbf{P}\}$.

$$\begin{aligned} \rho(\boldsymbol{\theta}_i) &= \sum_{r=1}^{d} \frac{\lambda_r}{(\lambda_r - \sigma)^2} |\mathbf{b}^T(\boldsymbol{\theta}_i)\mathbf{s}_r|^2 \\ &= \left[\mathbf{P}_R^{-1}\right]_{ii} + \sigma\left[\mathbf{P}_R^{-1}\left(\mathbf{B}^T\mathbf{B}\right)^{-1}\mathbf{P}_R^{-1}\right]_{ii} \end{aligned}$$

Proof: The MUSIC estimation error vector as given by Lemma 5.2.1 is

$$\mathbf{e}_i = \begin{bmatrix} \hat{\zeta}_i - \zeta_i \\ \hat{\phi}_i - \phi_i \end{bmatrix} = \left\{\mathbf{E}^{-1}\mathbf{p}\right\}_{\boldsymbol{\theta}=\boldsymbol{\theta}_i} = \frac{1}{\Delta}\begin{bmatrix} b & -c \\ -c & a \end{bmatrix}\begin{bmatrix} e \\ f \end{bmatrix}$$

We proceed to derive the expression for the variance of the estimator $\hat{\zeta}_i$. The remaining results can be obtained in similar fashion. The above equation yields

$$\zeta_i - \zeta_i = \frac{b'}{\Delta}, \text{ where } b' = be - cf. \quad [5.9]$$

As shown in [SN89], we have $\mathbf{b}^T(\boldsymbol{\theta}_i)\hat{\mathbf{G}}\hat{\mathbf{G}}^T \approx -\mathbf{b}^T(\boldsymbol{\theta}_i)\mathbf{S}\hat{\mathbf{S}}^T\mathbf{G}\mathbf{G}^T$. This result leads to the following expressions for the random quantities e and f in terms of the estimated signal space eigenvectors, whose statistics are available. T'he dependence of the expressions on $\boldsymbol{\theta}_i$ is dropped for conciseness.

$$\begin{aligned} e &= -\mathbf{b}^T\hat{\mathbf{G}}\hat{\mathbf{G}}^T\mathbf{b}_\zeta \approx \mathbf{b}^T\mathbf{S}\hat{\mathbf{S}}^T\mathbf{G}\mathbf{G}^T\mathbf{b}_\zeta = \mathbf{b}_\zeta^T\mathbf{G}\mathbf{G}^T\hat{\mathbf{S}}\mathbf{S}^T\mathbf{b} \\ f &= -\mathbf{b}^T\hat{\mathbf{G}}\hat{\mathbf{G}}^T\mathbf{b}_\phi \approx \mathbf{b}^T\mathbf{S}\hat{\mathbf{S}}^T\mathbf{G}\mathbf{G}^T\mathbf{b}_\phi = \mathbf{b}_\phi^T\mathbf{G}\mathbf{G}^T\hat{\mathbf{S}}\mathbf{S}^T\mathbf{b} \end{aligned}$$

Substituting in Equation 5.9, and using the definitions in Lemma 5.2.1 leads to the following expression for the term ***b':***

$$b' = \mathbf{q}^T\mathbf{z}, \qquad [5.10]$$

where $\boldsymbol{q} = (b\mathbf{b}_\zeta - c\mathbf{b}_\phi)$ is a deterministic quantity, and $\boldsymbol{z} = \mathbf{G}\mathbf{G}^T\hat{\mathbf{S}}\mathbf{S}^T\mathbf{b}$ is a random vector. The vector $\boldsymbol{z}$ will shortly be shown to have the following stististics:

$$\begin{aligned} \mathrm{E}(\boldsymbol{z}) &= 0, \text{ and} \qquad [5.11] \\ \mathrm{Cov}(\mathbf{z}) &= \mathrm{E}\left(\mathbf{z}\mathbf{z}^T\right) = \frac{\sigma\rho}{2K}\mathbf{G}\mathbf{G}^T, \end{aligned}$$

where $\rho(\boldsymbol{\theta}_i)$ is defined in the theorem statement. Equation 5.10 now- yields E $\boldsymbol{(b')} = 0$, and Var $\boldsymbol{(b')} = \frac{\sigma\rho}{2K}\mathbf{q}^T\mathbf{G}\mathbf{G}^T\mathbf{q} = \frac{\sigma\rho b\Delta}{2K}$. The final equality results because $\mathbf{q}^T\mathbf{G}\mathbf{G}^T\mathbf{q} = b\Delta$, a relationship which is easily verified. Employing these results in Equation 5.9 completes the proof: We obtain $\mathrm{E}(\hat{\zeta}_i - \zeta_i) = 0$, and $\mathrm{Var}(\hat{\zeta}_i) = \frac{\sigma}{2K}\left\{\frac{\rho b}{\Delta}\right\}_{\boldsymbol{\theta}=\boldsymbol{\theta}_i}$. The proof for the expression of $\rho(\boldsymbol{\theta}_i)$ in terms of $\mathbf{P}_R = \mathrm{Re}\{\mathbf{P}\}$ follows a similar proof in [SN89].

It now remains to verify the expressions for the statistics of the vector $\boldsymbol{z}$. We have

$$\mathbf{z} = \mathbf{G}\mathbf{G}^T\hat{\mathbf{S}}\mathbf{S}^T\mathbf{b} = \sum_{k=1}^{d}\mathbf{G}\mathbf{G}^T\hat{\mathbf{s}}_k(\mathbf{s}_k^T\mathbf{b}) = \sum_{k=1}^{d}(\mathbf{b}^T\mathbf{s}_k)\mathbf{G}\mathbf{G}^T(\hat{\mathbf{s}}_k - \mathbf{s}_k). \qquad [5.12]$$

We have $\mathrm{E}(\hat{\mathbf{s}}_k - \mathbf{s}_k) = 0$ from Lemma 5.2.2, and thus E $\boldsymbol{(z)} = 0$ as claimed. Now,

$$\mathrm{Cov}(\mathbf{z}) = \mathrm{E}[\mathbf{z}\mathbf{z}^T] = \sum_{k=1}^{d}\sum_{l=1}^{d}(\mathbf{b}^T\mathbf{s}_k)(\mathbf{b}^T\mathbf{s}_l)\mathbf{G}\mathbf{G}^T\mathrm{E}\left[(\hat{\mathbf{s}}_k - \mathbf{s}_k)(\hat{\mathbf{s}}_l - \mathbf{s}_l)^T\right]\mathbf{G}\mathbf{G}^T.$$

Using the result of Lemma 5.2.2 on the signal eigenvector statistics, we obtain

$$\begin{aligned}
\mathrm{Cov}\,(\mathbf{z}) &= \frac{1}{K}\sum_{k=1}^{d}\sum_{l=1}^{d}(\mathbf{b}^T\mathbf{s}_k)(\mathbf{b}^T\mathbf{s}_l)\frac{\lambda_k\sigma\delta_{kl}}{2(\lambda_k-\sigma)^2}\sum_{r=d+1}^{N'}\mathbf{g}_r\mathbf{g}_r^T \\
&= \frac{\sigma}{2K}\left(\sum_{k=1}^{d}\frac{\lambda_k}{(\lambda_k-\sigma)^2}\,|\mathbf{b}^T(\boldsymbol{\theta}_i)\mathbf{s}_k|^2\right)\mathbf{G}\mathbf{G}^T \\
&= \frac{\sigma\rho(\boldsymbol{\theta}_i)}{2K}\,\mathbf{G}\mathbf{G}^T
\end{aligned}$$

as claimed in Equation 5.11.

5.3 Performance Analysis of UCA-ESPRIT

Techniques similar to those used in [RH89a] to analyze the performance of the ESPRIT algorithm for 1D angle estimation are employed in the following analysis of UCA-ESPRIT [MZ93b]. As described in Section 4.3, the eigenvalues of the matrix $\hat{\boldsymbol{\Psi}}$ have the form $\hat{\mu}_i = \sin\hat{\theta}_i\, e^{j\hat{\phi}_i} = \hat{u}_i + j\hat{v}_i$, and provide automatically paired source DOA estimates. Theorem 5.3.1 gives asymptotic expressions for the variances and covariance of the UCA-ESPRIT direction cosine estimators **il;** and **6;.** The theorem also gives approximate expressions (accurate at moderate to high SNRs) for the variances of the estimators $\hat{\zeta}_i' = \sin\hat{\theta}_i$ and $\hat{\phi}_i$.

The asymptotic variance expressions in Theorem 5.3.1 involve the eigenvectors of $\boldsymbol{\Psi}$. Equation 4.33 gives the spectral decomposition of $\boldsymbol{\Psi}$: We have $\boldsymbol{\Psi} = \mathbf{T}^{-1}\boldsymbol{\Phi}\mathbf{T}$, where $\mathbf{T}$ is real-valued. The left and right eigenvectors of $\boldsymbol{\Psi}$ are thus real valued, and are denoted $\mathbf{q}_i^T$ and x;, respectively. The UCA-ESPRIT algorithm incorporates beamspace signal subspace computation via a real-valued EVD: We have $\mathbf{S_u} = \mathbf{C_o}\mathbf{W}\mathbf{S}$, where $\mathbf{S_u}$ spans the UCA-ESPRIT signal subspace, and $\mathbf{S}$ is obtained via the EVD of the real-valued matrix $\mathbf{R}$ of Equation 4.19. The analysis of UCA-ESPRIT thus requires the statistics of the signal eigenvector estimates $\hat{\mathbf{s}}_i$ that form the columns of $\hat{\mathbf{S}}$. Lemma 5.2.2 in Section 5.2 gives these statistics.

A superscript e is used to denote the error in an estimate in the following developments e.g., $\mathbf{sf} = \hat{\mathbf{s}}_i - \mathbf{s}$; is the error in the ith signal eigenvector estimate. The superscript $+$ is used to denote the Moore-Penrose pseudo-inverse e.g., $\mathbf{E}^+ = (\mathbf{E}^H\mathbf{E})^{-1}\mathbf{E}^H$ is the pseudo-inverse of $\mathbf{E}$.

Theorem 5.3.1 The UCA-ESPRIT direction cosine estimators $\hat{u}_i$ iand $\hat{v}_i$ are asymptotically unbiased. Asymptotic (large K) expressions for the variances and covariance of these estimators are given below:

$$\begin{aligned} Var(\hat{u}_i) &= \boldsymbol{\alpha}_{iR}^T \mathbf{H}_i \boldsymbol{\alpha}_{iR} \\ Var(\hat{v}_i) &= \boldsymbol{\alpha}_{iI}^T \mathbf{H}_i \boldsymbol{\alpha}_{iI} \\ Cov(\hat{u}_i, \hat{v}_i) &= \boldsymbol{\alpha}_{iR}^T \mathbf{H}_i \boldsymbol{\alpha}_{iI} \end{aligned} \qquad [5.13]$$

The matrices $\mathbf{H}_i$ and the vectors $\mathbf{a}_i = \boldsymbol{\alpha}_{iR} + j\boldsymbol{\alpha}_{iI}$ are defined as follows:

$$\begin{aligned} \mathbf{H}_i &= \sum_{j=1}^{d}\sum_{k=1}^{d} \mathbf{x}_{ij}\mathbf{x}_{ik} Cov(\mathbf{s}_j^e, \mathbf{s}_k^e) \\ \boldsymbol{\alpha}_i^T &= \mathbf{q}_i^T \mathbf{E}^{+t} \left[\Gamma\boldsymbol{\Delta}_0\mathbf{C}_o\mathbf{W} - \mu_i\boldsymbol{\Delta}_{-1}\mathbf{C}_o\mathbf{W} - \mu_i^*\mathbf{D}\tilde{\mathbf{I}}\boldsymbol{\Delta}_{-1}\mathbf{C}_o\mathbf{W}^*\right], \end{aligned} \qquad [5.14]$$

where $\mathbf{E}^{+t} = \left[\mathbf{I}_d \vdots \mathbf{0}_{d\times d}\right]\mathbf{E}^+$. The matrix $\mathbf{E} = \left[\mathbf{S}_{-1} \vdots \mathbf{D}\tilde{\mathbf{I}}\mathbf{S}_{-1}^*\right]$ is formed using the true signal space eigenvectors. The following approximate expressions for the asymptotic variances of the estimators $\hat{\zeta}_i' = \sin\hat{\theta}_i$ and $\hat{\phi}_i$ are accurate at moderate to high SNRs.

$$\mathrm{Var}(\hat{\zeta}_i') \approx \mathrm{Var}_{(\mathbf{Qi})}\cos^2\phi_i + \mathrm{Var}(\hat{v}_i)\sin^2\phi_i + \mathrm{Cov}(\hat{u}_i, \hat{v}_i)\sin 2\phi_i \qquad [5.15]$$

$$\mathrm{Var}(\hat{\phi}_i) \approx \frac{1}{(\zeta_i')^2}\left[\mathrm{Var}(\hat{v}_i)\cos^2\phi_i + \mathrm{Var}(\hat{u}_i)\sin^2\phi_i - \mathrm{Cov}(\hat{u}_i, \hat{v}_i)\sin 2\phi_i\right]. \qquad [5.16]$$

Proof: To a first order approximation, the UCA-ESPRIT eigenvalue error due to errors in subspace estimates is

$$\mu_i^e = \mathbf{q}_i^T \boldsymbol{\Psi}^e \mathbf{x}_i. \qquad [5.17]$$

The least squares solution to the overdetermined system $\hat{\mathbf{E}}\underline{\boldsymbol{\Psi}} = \Gamma\hat{\mathbf{S}}_0$ of Equation **4.35** yields the estimate $\underline{\hat{\boldsymbol{\Psi}}} = [\hat{\boldsymbol{\Psi}}^T \vdots \hat{\boldsymbol{\Psi}}^H]^T$. This system can be rewritten as $(\mathbf{E} + \mathbf{E}^e)(\underline{\boldsymbol{\Psi}} + \underline{\boldsymbol{\Psi}}^e) = \Gamma(\mathbf{S}_0 + \mathbf{S}_0^e)$. Using the fact that $\mathbf{E}\underline{\boldsymbol{\Psi}} = \Gamma\mathbf{S}_0$, and retaining only first order terms, we obtain $\mathbf{E}\underline{\boldsymbol{\Psi}}^e = \Gamma\mathbf{S}_0^e - \mathbf{E}^e\underline{\boldsymbol{\Psi}}$. Employing the least squares solution yields

the equation $\underline{\boldsymbol{\Psi}}^e = \mathbf{E}^+ (\boldsymbol{\Gamma}\mathbf{S}_0^e - \mathbf{E}^e\underline{\boldsymbol{\Psi}})$. This solution is adequate in that it yields expressions for DOA estimator variance that are accurate to $o(K^{-1})$ [RH89a]. Now $\boldsymbol{\Psi}^e = \left[\mathbf{I}_d \vdots \mathbf{0}_{d\times d}\right] \underline{\boldsymbol{\Psi}}^e$ and thus

$$\boldsymbol{\Psi}^e = \mathbf{E}^{+t} [\boldsymbol{\Gamma}\mathbf{S}_0^e - \mathbf{E}^e\underline{\boldsymbol{\Psi}}], \qquad [5.18]$$

where $\mathbf{E}^{+t} = \left[\mathbf{I}_d \vdots \mathbf{0}_{d\times d}\right] \mathbf{E}^+$. We have $\mathbf{E}^e = \left[\mathbf{S}_{-1}^e \vdots \mathbf{D}\tilde{\mathbf{I}}\mathbf{S}_{-1}^{e^*}\right]$, where $\mathbf{S}_i^e = \boldsymbol{\Delta}_i\mathbf{C}_o\mathbf{W}\mathbf{S}^e$, $i = -1, 0$. Substituting in Equation **5.18** leads to the following expression:

$$\boldsymbol{\Psi}^e = \mathbf{E}^{+t} \left[\boldsymbol{\Gamma}\boldsymbol{\Delta}_0\mathbf{C}_o\mathbf{W}\mathbf{S}^e - \boldsymbol{\Delta}_{-1}\mathbf{C}_o\mathbf{W}\mathbf{S}^e\boldsymbol{\Psi} - \mathbf{D}\tilde{\mathbf{I}}\boldsymbol{\Delta}_{-1}\mathbf{C}_o\mathbf{W}^*\mathbf{S}^e\boldsymbol{\Psi}^*\right]. \qquad [5.19]$$

Substituting **(5.19)** in **(5.17)** and using the fact that $\mathbf{x}_i$ is a real-valued eigenvector of $\boldsymbol{\Psi}$, we obtain the equation

$$\mu_i^e = u_i^e + jv_i^e = \boldsymbol{\alpha}_i^T\mathbf{S}^e\mathbf{x}_i, \qquad [5.20]$$

where $\boldsymbol{\alpha}_i^T = \boldsymbol{\alpha}_{iR}^T + j\boldsymbol{\alpha}_{iI}^T = \mathbf{q}_i^T\mathbf{E}^{+t} \left[\boldsymbol{\Gamma}\boldsymbol{\Delta}_0\mathbf{C}_o\mathbf{W} - \mu_i\boldsymbol{\Delta}_{-1}\mathbf{C}_o\mathbf{W} - \mu_i^*\mathbf{D}\tilde{\mathbf{I}}\boldsymbol{\Delta}_{-1}\mathbf{C}_o\mathbf{W}^*\right]$ is a complex-valued vector. Both $\mathbf{S}^e = \left[\mathbf{s}_1^e \vdots \ldots \vdots \mathbf{s}_d^e\right]$ and $\mathbf{x}_i$ are real-valued. From Equation **5.20,** we have

$$u_i^e = \boldsymbol{\alpha}_{iR}^T\mathbf{S}^e\mathbf{x}_i, \text{ and } v_i^e = \boldsymbol{\alpha}_{iI}^T\mathbf{S}^e\mathbf{x}_i. \qquad [5.21]$$

It is now evident from Lemma **5.2.2** that $\mathrm{E}(\mathbf{uf}) = \mathrm{E}(\mathbf{vf}) = 0$. The UCA-ESPRIT direction cosine estimates are thus asymptotically unbiased as claimed. Equations **5.13** and **5.14** that define the variances of the direction cosine estimators follow on straightforward application of the results of Lemma **5.2.2** in Equation **5.21.**

It now remains to verify Equations **5.15** and **5.16** that respectively give asymptotic expressions for the variances of the estimators ζ_i' and ϕ_i. These expressions follow from the geometry depicted in Figure **5.1.** The subscript i that denotes the ith source is dropped for notational expedience. Let the UCA-ESPRIT eigenvalue error be $\mu^e = |\mu^e|e^{j\beta}$. The errors in the direction cosine estimates are thus $u^e = |\mu^e|\cos\beta$, and $v^e = |\mu^e|\sin\beta$. From Figure **5.1** we see that $l_1 = |\mu^e|\cos(\beta - \mathbf{4}) \approx \zeta'^e$. We thus obtain $\zeta'^e \approx \mathbf{u}^e\cos\phi + \mathbf{v}^e\sin\mathbf{4}$. This leads to the expression in **(5.15)** as $\mathrm{E}(\zeta'^e) = \mathbf{0}$,

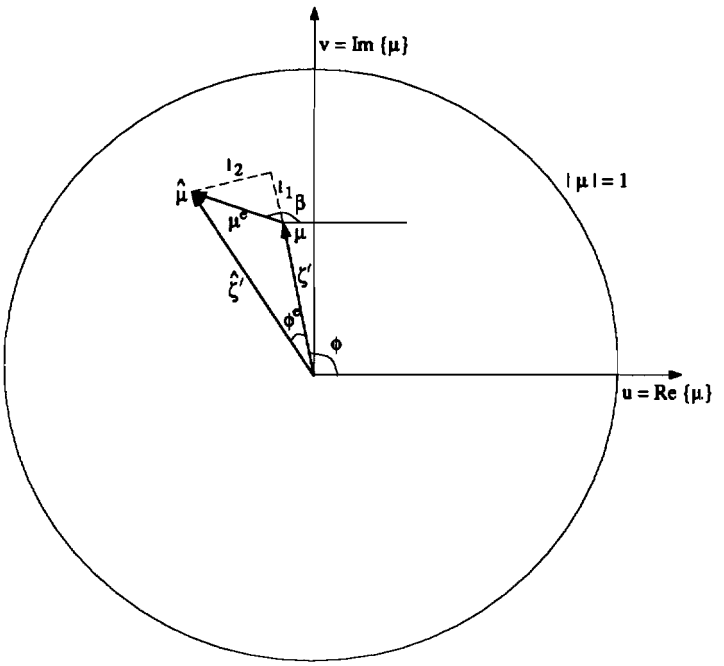

Figure 5.1 UCA-ESPRIT eigenvalue error.

and $\mathrm{Var}(\hat{\zeta}') = \mathrm{Var}(\zeta'^{e})$. Figure 5.1 also shows that $l_2 = |\mu^e| \sin(\beta - \phi) \approx \zeta' \phi^e$. Thus $\phi^e \approx \frac{1}{\zeta'} [v^e \cos\phi - u^e \sin\phi]$, and the expression in (5.16) follows as $E(\phi^e) = 0$, and $\mathrm{Var}(\hat{\phi}) = \mathrm{Var}(\phi^e)$. The approximations made in obtaining the above expressions are accurate provided the eigenvalue error μ^e is small; the expressions are thus accurate for moderate to high SNRs. Note that $\mathrm{Var}(\hat{\phi}) \propto 1/(\sin^2 \theta)$: The variance of the azimuth estimator thus increases as the elevation angle θ decreases. This is an intuitive result; we know that azimuth is not a good descriptor of source DOA when θ is small (in fact all azimuth angles are equivalent when $\theta = 0°$).

5.4 The Cramer-Rao Bound

It is instructive to compare the performance of the element space MUSIC, UCA-RB-MUSIC, and UCA-ESPRIT estimators with the ultimate performance dictated by the Cramer-Rao bound (CRB). The following lemma gives the CRB on the covariance matrix of unbiased estimators of the parameter vector $\Theta = [\zeta_1, \ldots, \zeta_d, \phi_1, \ldots, \phi_d]^T$. The CRB expression below is based on a random signal model, and is known as the

unconditional, or stochastic CRB. The result is a generalization of a similar result in [SN90] for the 1D angle estimation problem. The symbol $\odot$ is used to clenote the Hadamard or element-wise matrix product.

Lemma 5.4.1 The stochastic CRB for any unbiased estimator of $\boldsymbol{\Theta}$ is

$$CRB(\boldsymbol{\Theta}) = \frac{\sigma}{2\mathrm{K}} \left[\mathrm{Re}\left\{\mathrm{H} \odot \mathbf{P}_{+}^{T}\right\}\right]^{-1}, \text{ where} \qquad [5.22]$$

$$\mathbf{P}_{+} = \begin{bmatrix} \mathrm{P}' & \mathbf{P}' \\ \mathbf{P}' & \mathbf{P}' \end{bmatrix} \text{ with } \mathrm{P}' = \mathbf{P}\underline{\mathbf{A}}^{H}\underline{\mathbf{R}}^{-1}\underline{\mathbf{A}}\mathbf{P},$$

$$\mathbf{H} = \mathbf{D}^{H}\left[I - \underline{\mathbf{A}}\left(\underline{\mathbf{A}}^{H}\underline{\mathbf{A}}\right)^{-1}\underline{\mathbf{A}}^{H}\right]\mathbf{D}, \text{ and}$$

$$\mathbf{D} = [\underline{\mathbf{a}}_{\zeta}(\boldsymbol{\theta}_1), \ldots, \underline{\mathbf{a}}_{\zeta}(\boldsymbol{\theta}_d), \underline{\mathbf{a}}_{\phi}(\boldsymbol{\theta}_1), \ldots, \underline{\mathbf{a}}_{\phi}(\boldsymbol{\theta}_d)]$$

We point out that the expression (valid when K is large) for the conditional., or deterministic CRB can be obtained by making the substitution $\mathrm{P}' = \mathrm{P}$ in the lemma. Due to the simpler expression for P+, the deterministic CRB is employed in the theoretical performance study in Section 5.5. The study is meaningful as the deterministic CRB is a tighter bound than the stochastic CRB. The stochastic CRB is however used as the benchmark for comparison in the simulations of Section 5.6. This is because our developments have assumed a random signal model.

5.5 Study of Theoretical Performance for the One and Two Source Cases

This section investigates the theoretical performance of the element space MUSIC, UCA-RB-MUSIC, and UCA-ESPRIT estimators for the one and two source cases. The behavior of the deterministic CRB is also studied. The study focuses on the behavior of the direction cosine estimators $\hat{u}$ and 6 rather than the behavior of $\hat{\zeta}$ and $\hat{\phi}$. This is because the variance of the azimuth estimator $\hat{\phi}$ increases as θ decreases. Further, all values of ϕ are equivalent when the elevation $\theta = 0°$. There is no such ambiguity in the direction cosine space; we have u = v = 0. The vector of direction cosines, $\boldsymbol{\beta} = (u, v)$ is thus used to represent the source DOAs. The: results of Theorems 5.1.1 and 5.2.1 are easily modified to give the variances of the direction

cosine estimators. All that is required is to replace the subscripts ζ and ϕ denoting partial derivatives by the subscripts u and v, respectively. The same substitution in Lemma **5.4.1** gives the CRB expressions for the direction cosine estimators.

The main results of this theoretical performance study are as follows: (a) The deterministic CRB is independent of the source DOA in the single source scenario. For the two source case, the CRB depends only on the distance τ between the two source locations in the uv plane, and their relative orientation as specified by the angle ν of the line joining these locations. *(b)* Closed-form expressions for the element space MUSIC estimator variances are obtained for both the one and two source cases. The element space MUSIC estimator variances exhibit the same behavior as the CRB for these cases. *(c)* It is shown via a study of theoretical performance curves that the DOA dependence of the UCA-RB-MUSIC estimator variances closely follows the behavior of the CRB and element space MUSIC. The performance curves also demonstrate that UCA-RB-MUSIC can outperform element space MUSIC in correlated source scenarios when N is odd. (d) The UCA-ESPRIT estimator variances for the single source case are independent of azimuth at low elevation angles ($\sin\theta < 0.6$). At higher elevation angles, the estimator variances become azimuth dependent.

5.5.1 The Deterministic CRB

Consider the case of a single source of power $p = \mathrm{E}\,|s(n)|^2$ incident on the UCA from the direction $\beta = (u, v)$. Appendix D.2 shows that the deterministic CRB for unbiased estimators of u and v is

$$CRB(\hat{u}) = CRB(\hat{v}) = \frac{1}{KN(k_0 r)^2(p/\sigma)}, \qquad [5.23]$$

where p/σ is the signal to noise ratio. The CRBs for u and v are identical, and are independent of the arrival angle. The UCA thus favors all arrival angles equally. Not all array configurations have this desirable property; the rectangular array, for example, does not.

Let β_1 and β_2 specify the source DOAs for the two source case. Let the difference vector $\beta_d = \beta_2 - \beta_1$ have the representation $\beta_d = \tau e^{j\nu}$ in polar coordinates. τ is the

distance between the two sources in the uv plane, and ν is the angle of the line joining the two sources. Appendix D.2 shows that the dependence of the CRBs on the source DOAs is only through the vector $\boldsymbol{\beta}_d$, or equivalently, through the parameters τ and v. Thus the CRBs do not depend on the absolute positions of the sources but only on their positions relative to each other.

5.5.2 Performance of Element Space MUSIC

The variances of the element space MUSIC estimators for the single source case are shown in Appendix D.l to be

$$\mathrm{Var}(\hat{u}) = \mathrm{Var}(\hat{v}) = \frac{1 + 1/N}{KN(k_0 r)^2 (p/\sigma)}. \qquad [5.24]$$

The u and v estimator variances are equal and independent of the source DOA. Comparison with Equation 5.23 shows that the element space MUSIC estimators are asymptotically efficient in the single source scenario.

Theorem 5.1.1 gives expressions for the element space MUSIC estimator variances. We have $\mathrm{Var}(\hat{u}_i) = (\sigma \underline{\rho} \underline{b}/2K\underline{\Delta})|_{\boldsymbol{\beta}=\boldsymbol{\beta}_i}$, and $\mathrm{Var}(\mathrm{it},) = (\sigma \underline{\rho} \underline{a}/2K\underline{\Delta})|_{\boldsymbol{\beta}=\boldsymbol{\beta}_i}$. Simplified expressions for the parameters $\underline{a}$[1], $\underline{b}$ and $\underline{c}$ can be obtained for the two source case; Appendix D.l outlines the derivation of the following results:

$$\begin{aligned}
\underline{a}(\boldsymbol{\beta}_1) = \underline{a}(\boldsymbol{\beta}_2) &\approx (k_0 r)^2 \left[\frac{N}{2} - q\{NJ_1(k_0 r\tau)\cos\nu\}^2\right] \qquad [5.25]\\
\underline{b}(\boldsymbol{\beta}_1) = \underline{b}(\boldsymbol{\beta}_2) &\approx (k_0 r)^2 \left[\frac{N}{2} - q\{NJ_1(k_0 r\tau)\sin\nu\}^2\right]\\
\underline{c}(\boldsymbol{\beta}_1) = \underline{c}(\boldsymbol{\beta}_2) &\approx -(k_0 r)^2 q\{NJ_1(k_0 r\tau)\}^2 \sin\nu\cos\nu\\
\underline{\rho}(\boldsymbol{\beta}) &\approx f(\tau, \mathbf{P})
\end{aligned}$$

In the above equations, $q = \frac{1}{N[1 - J_0^2(k_0 r\tau)]}$. The final equation above signifies that the quantity $\underline{\rho}$ is a function of τ and the source covariance matrix $\mathbf{P}$. Equation 5.25 shows that $\underline{a}, \underline{b}, \underline{c}$, and $\underline{\rho}$ depend on the source DOAs only through the parameters τ and ν. Thus the element space MUSIC estimator variances depend only on τ and ν: this behavior is similar to that of the CRBs. Equation 5.25 also shows that the

[1]The scalar $\underline{a}$ is distinct from the UCA manifold vector $\underline{\mathbf{a}}$

parameters $\underline{a}, \underline{b}$, and $\underline{c}$ are the same for the two sources. The parameter $\underline{p}$ is also the same for both sources, provided they are equipowered. Thus with equipowered sources, the u and v estimator variances are the same for both sources.

It can be verified that the variances of the u estimates are highest when the angle $\nu = 0$, i.e., when the sources have different u coordinates but the same v coordinate. Similarly, the variances of the v estimates are highest when $\nu = \pi/2$. Now, $\underline{c} = 0$ when $\nu = 0$ or $\pi/2$ and hence $\underline{\Delta} = \underline{ab}$. The estimator variances corresponding to these orientations are thus given by $\text{Var}(\hat{u}) = \frac{\sigma\underline{\rho}}{2K\underline{a}}$, and $\text{Var}(\hat{v}) = \frac{\sigma\underline{\rho}}{2K\underline{b}}$. The minimum values that $\underline{a}$ and $\underline{b}$ take are identical and equal to $(k_0 r)^2[\frac{N}{2} - qN^2 J_1^2(k_0 r\tau)]$. The worst case estimator variances for any two source scenario are thus

$$\max(\text{Var}\,\hat{u}_i) = \max(\text{Var}\,\hat{v}_i) = \frac{\sigma\underline{\rho}(\beta_i)}{2K(k_0 r)^2[\frac{N}{2} - \text{qN}^2 J_1^2(k_0 r\tau)]}. \qquad [5.26]$$

The expression above depends only on the distance τ, and the siignal powers and correlations as specified by the source covariance matrix $\mathbf{P}$.

Figure 5.2 depicts the theoretical performance curves (dashed lines) of the element space MUSIC estimators in a two source scenario. The scenario is identical to that of Simulation Example 1 in Section 5.6: the location of the first source is kept fixed, and the angle ν is changed by shifting the position of the second source. The distance between the sources is maintained at $\tau = 0.25$, corresponding to a spacing of about two thirds of the main-lobe width of the cophasal beampattern. The graphs depict the estimator performance as a function of the angle ν between the sources. As expected, the highest u and v estimator variances occur at $\nu = 0$, and $\nu = \pi/2$, respectively. The estimator variances are seen to be identical for the two sources. This is in accord with expectations as the sources are equipowered (SNR=7dB). The ultimate performance dictated by the CRB is also sketched (dotted lines) in the figure. Note that the element space MUSIC, and CRB performance curves are independent of the location of the first source.

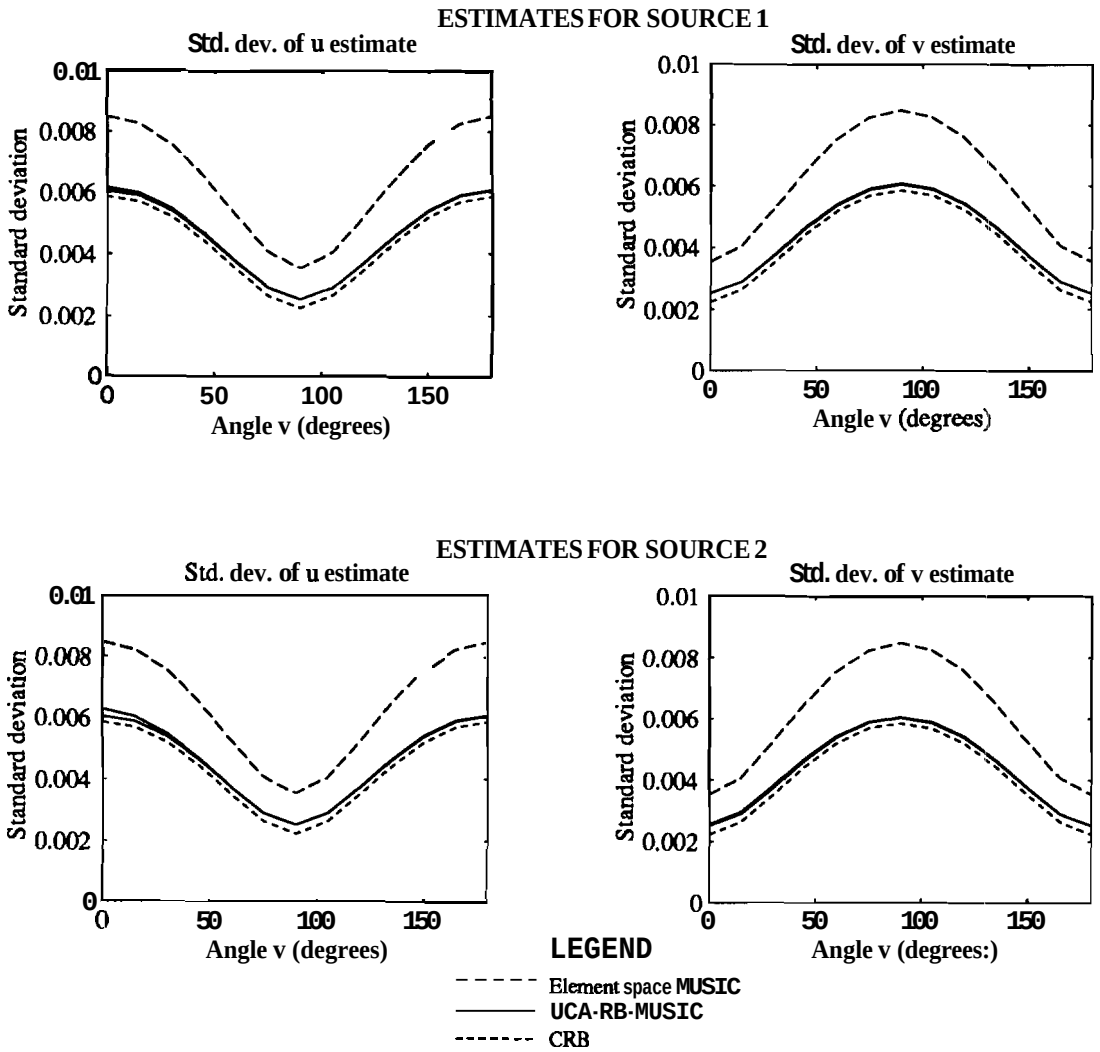

Figure 5.2 Theoretical performance of element space MUSIC and UCA-RB-MUSIC as a function of ν.

5.5.3 Performance of **UCA-RB-MUSIC**

Theorem 5.2.1 gives expressions for the UCA-RB-MUSIC estimator variances. We have $\mathrm{Var}(\hat{u}_i) = (\sigma\rho b/2K\Delta)|_{\boldsymbol{\beta}=\boldsymbol{\beta}_i}$, and $\mathrm{Var}(\hat{v}_i) = (\sigma\rho a/2K\Delta)|_{\boldsymbol{\beta}=\boldsymbol{\beta}_i}$. The beamspace manifold $\mathbf{a_r}(\boldsymbol{\theta})$ of Equation 4.7 (denoted $\mathbf{b}(\boldsymbol{\theta})$ in this chapter) has complex structure. Thus, unlike with element space MUSIC, simple expressions for the parameters a, *b*, and c cannot be obtained. The beamformer $\mathbf{F}_\mathbf{r}^H$ that makes the transformation to beamspace is orthogonal and one might thus expect the behavior of the UCA-RB-MUSIC estimates to be similar to that of the element space MUSIC estimates. Examination of theoretical performance curves reveals that this is indeed true. Figure 5.2 depicts the theoretical performance of the UCA-RB-MUSIC estimators (solid lines) for the same two source scenario. The graphs shown are a superposition of the performance curves corresponding to four different locations of the first source. These locations are $\boldsymbol{\beta} = (u, v) = (0,0), (0.15, 0.15), (-0.3, 0.3)$ and $(0.45, -0.45)$. The curves are almost identical, confirming that the the dependence of the UCA-RB-MUSIC estimator variances on the source DOAs is for the most part through the parameters τ and ν.

The graphs in Figure 5.2 also show that UCA-RB-MUSIC outperforms element space MUSIC in the source scenario under consideration. This is due to the decorrelating effect of the FB average inherent in UCA-RB-MUSIC. FB averaging is not possible in element space when N is odd, and UCA-RB-MUSIC thus outperforms element space MUSIC.

5.5.4 Performance of **UCA-ESPRIT**

Theorem 5.3.1 gives expressions for the variances of the UCA-ESPRIT direction cosine estimates $\hat{u}_i$ and $\hat{v}_i$. These expressions are quite complicated and cannot be simplified even for the single source case. Theoretical performance curves are used to investigate the performance of UCA-ESPRIT for the single source case with an SNR of 5dB. The standard deviations of the direction cosine estimates as a function of source azimuth angle are plotted in Figure 5.3 for several different elevation angles

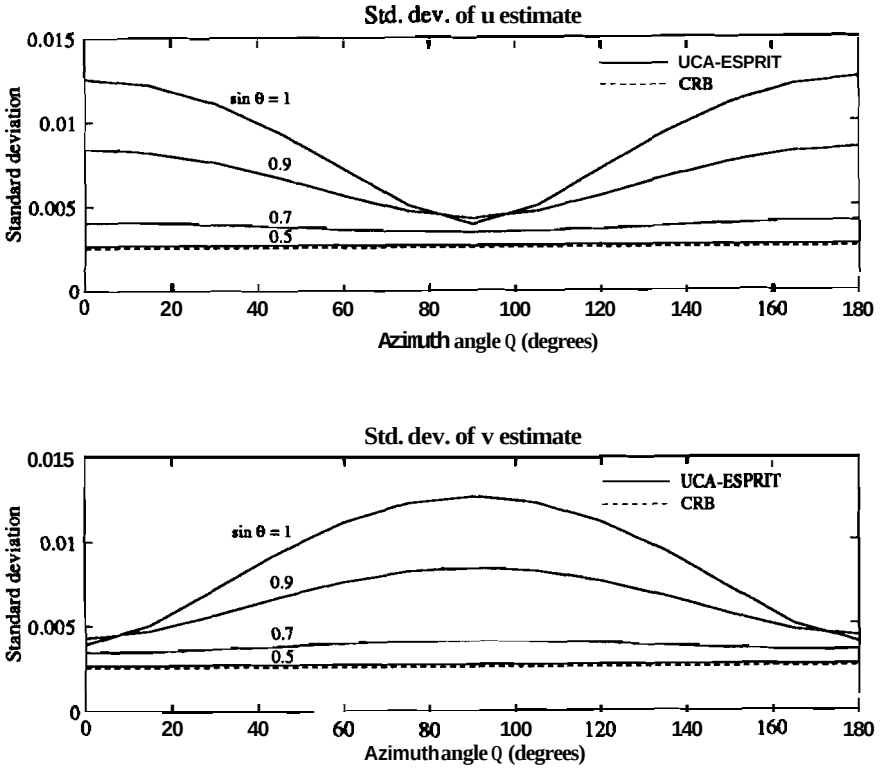

Figure 5.3 Theoretical performance of UCA-ESPRIT for the single source case.

($\zeta' = \sin\theta = 0.5, 0.7.0.9$ and 1.0). The deterministic CRB (which is independent of source location) is also plotted. The theoretical performance curves show that the estimator performance virtually meets the CRB for $\zeta' < 0.5$. The estimator performance degrades as ζ' increases from 0.5 to 1.0. The performance also becomes azimuth dependent at these higher elevation angles. The worst performance of the u estimate is at an azimuth of 0° (where v performs best), and the worst performance of the v estimate is at an azimuth of 90" (where u performs best). The behavior of $\mathrm{Cov}(u, \mathrm{v})$ as given by Equation 5.13 is responsible for the shape of the graphs. The correlation coefficent between the u and v estimates is observed to be close to zero for $\zeta' < 0.5$. The magnitude of the correlation coefficient increases with increasing ζ', and also becomes azimuth dependent; the correlation coefficient has smallest magnitude at azimuths of 0° and 90°. The u and v estimates are projections of the eigenvalue μ on the real and imaginary axes, respectively. This projection together with the behavior of the correlation coefficient is responsible for the curvature of the graphs at higher elevations. Although the variances of the u and v estimates are azimuth dependent, one would expect the variances of the ζ' and ϕ estimates to be independent of azimuth. Plots of the expressions of Equations 5.15 and 5.16 show that the ζ' and ϕ estimator variances are independent of azimuth, but are elevation dependent.

For comparison between UCA-RB-MUSIC and UCA-ESPRIT, we note that the UCA-RB-MUSIC u and v estimator variances are virtually DOA independent for the single source case. Further, these variances are very close to the CRB in the above single source scenario. UCA-RB-MUSIC thus performs better than UCA-ESPRIT, with the difference in performance being more pronounced at higher ζ'. The UCA-ESPRIT estimates can be used as starting points for Newton searches for peaks in the UCA-RB-MUSIC spectrum if estimates of better quality are required.

5.6 Results of Computer Simulations

This section documents the results of three computer simulations that explore the performance (estimator standard deviation) of UCA-RB-MUSIC and UCA-ESPRIT

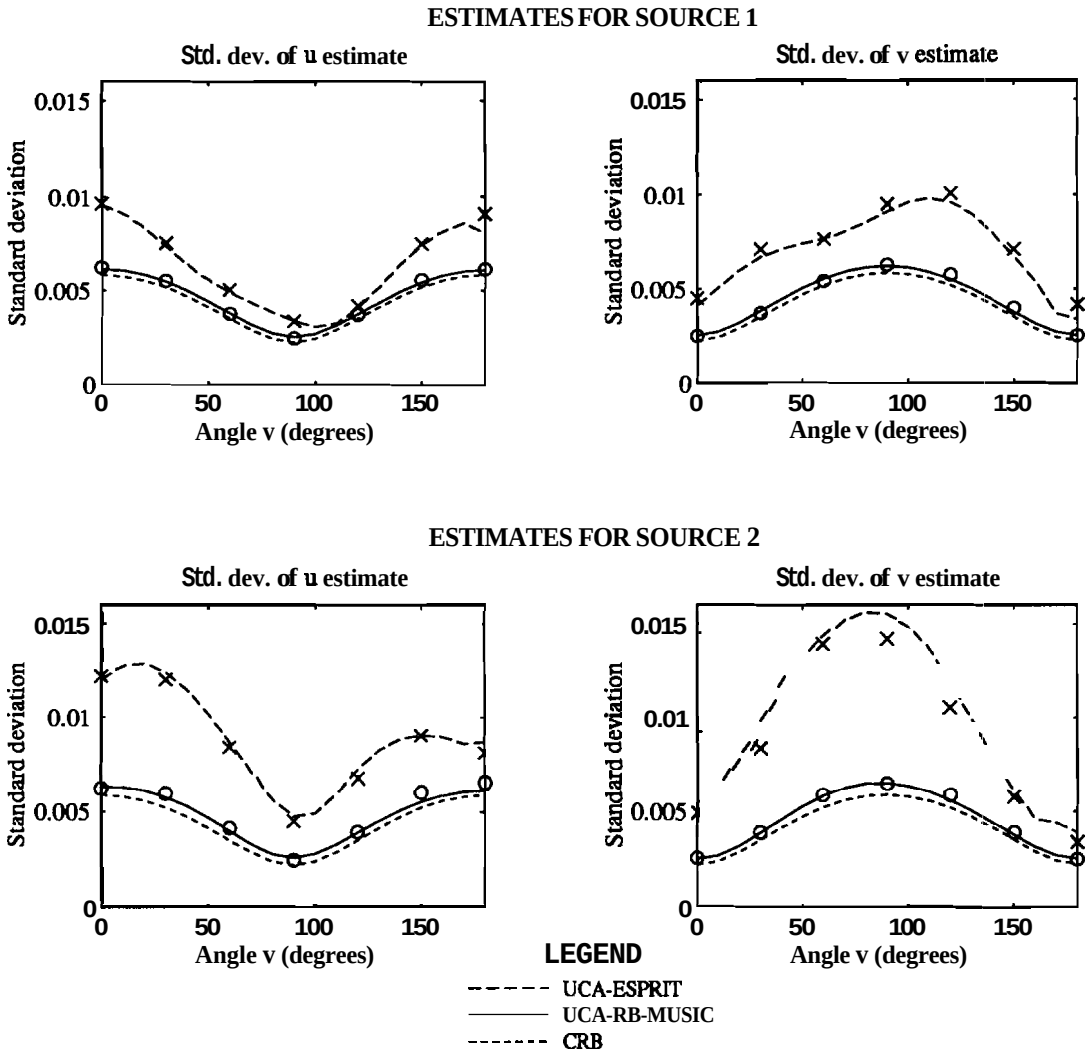

Figure 5.4 Performance of UCA-RB-MUSIC and UCA-ESPRIT as a function of ν.

in a two source scenario. Simulation examples 1,2, and 3 respectively investigate the performance of the algorithms as a function of the angle ν between the sources, the common source SNR, and the phase of the correlation coefficient between the signals. The computer simulations show that the experimental results closely match the theoretical performance predictions, thus validating the performance analysis results that have been obtained. The array and source descriptions for the simulations are as follows: The radius of the UCA is $r = \lambda$, and the maximum mode excited is $M = 6$ (this example was considered in Section 3.3.1). The number of array elements is chosen to be $N = 19$; Table 3.1 shows that the maximum residual contribution is negligible with these parameters. The source separation is $\tau = 0.25$ in all the simulations. This separation is about two-thirds of the main-lobe width of the cophasal UCA beam pattern that closely follows the Bessel function J_0 [CZ69]. The correlation between the signals is fairly high (magnitude of correlation coefficient = 0.8) in all the simulations. A moderate number of snapshots ($K = 64$) is employed. The theoretical asymptotic performance expressions are expected to be quite accurate with 64 snapshots. The simulations assume perfect detection of the number of sources. The SNRs quoted in the simulations are per source per array element. All the simulations feature equipowered sources; this implies identical values of the CRB for the two sources (also, the UCA-RB-MUSIC estimator variances for the first source will be very similar to those for the second source).

5.6.1 Simulation Example 1

This simulation investigates the estimator performance as a function of the angle ν of the line joining the two sources in the uv plane. The first source location is fixed at $\boldsymbol{\beta}_1 = (u_1, v_1) = (0.3, 0.6)$, corresponding to an elevation $\theta_1 = 42.1°$ and an azimuth $\phi_1 = 63.4'$. The angle ν is varied from $0°$ to $180°$ by rotating the second source about the first in the uv plane (the distance τ is set at 0.25). Both sources had SNRs of 7dB, and the correlation coefficient between the sources was $0.8e^{j\pi/4}$. The results of the simulations are plotted in Figure 5.4. The graphs show

that UCA-RB-MUSIC performs better than UCA-ESPRIT. Further, the UCA-RB-MUSIC performance is fairly close to the CRB. Note that the performance curves for UCA-RB-MUSIC and the CRB are independent of the location of the first source. In contrast, the performance of the UCA-ESPRIT estimates depends on the absolute position of each source. This is attested by the fact that the variances of the UCA-ESPRIT estimates are higher for the second source than for the first.

In the remaining two simulations, the second source is located at $\beta_2 = (u_2, v_2) = (0.175, 0.8165)$, corresponding to an elevation $\theta_2 = 56.62'$ and an azimuth $\phi_2 = 77.9'$. The location of the first source is left unchanged. These source locations correspond to a separation $\tau = 0.25$, and an orientation $\nu = 120'$. Examination of Figure 5.4 shows that the variance of the UCA-ESPRIT u estimate is higher for the second source than for the first at this value of v. However, the variance of the UCA-ESPRIT v estimates are approximately the same for the two sources. This behavior is evident in the UCA-ESPRIT performance curves of simulation examples 2 and 3. We reiterate that the UCA-RB-MUSIC performance curves and the CRB are identical for the two sources.

5.6.2 Simulation Example 2

This simulation examines the performance of the DOA estimators as a function of the common source SNR. The source locations are as specified in the previous paragraph, and the correlation coefficient between the sources is $0.8e^{j\pi/4}$. Figure 5.5 depicts the results of the simulations. The graphs show that the performance of UCA-RB-MUSIC is fairly close to the CRB even at 0dB SNR. UCA-RB-MUSIC)is seen to outperform UCA-ESPRIT; the performance difference, however, is less significant at higher SNRs. The experimental results for UCA-ESPRIT corresponding to 0dB SNR deviate a little from the theoretical predictions. This is probably because the first order approximation employed in the analysis is not accurate enough at this low SNR. Another observation from Figure 5.5 is that the UCA-ESPRIT estimator variances for the second source are a little lower than the theoretical predictions. This difference is

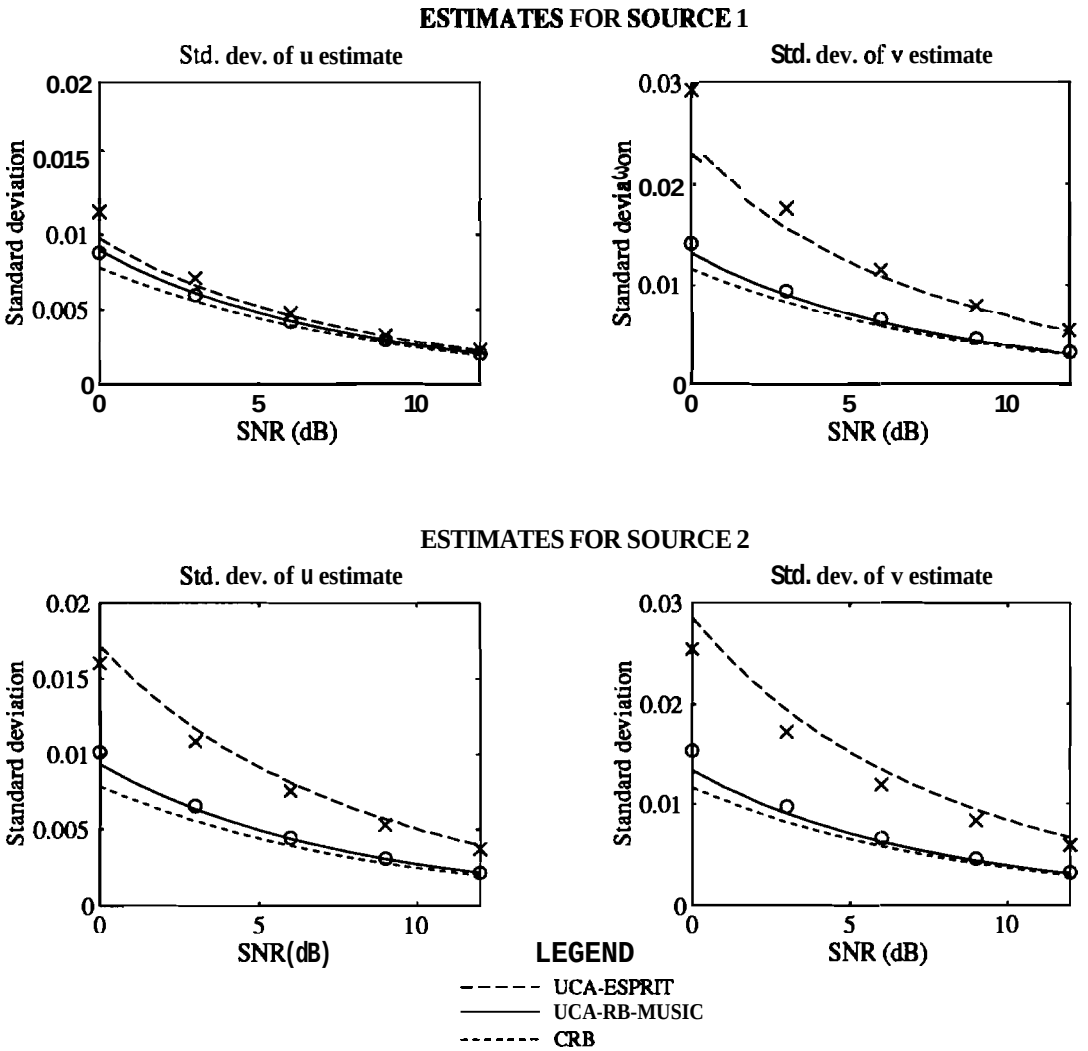

Figure 5.5 Performance of UCA-RB-MUSIC and UCA-ESPRIT as a function of the common source SNR.

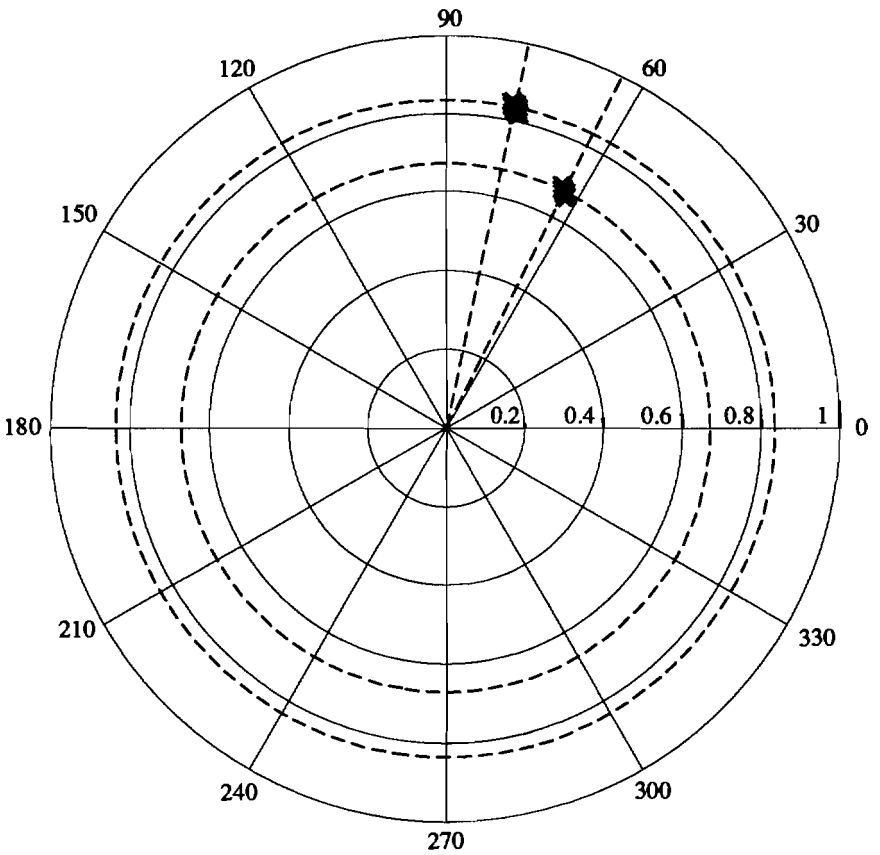

Figure 5.6 Plot of UCA-ESPRIT eigenvalues.

more pronounced in Figure 5.7 corresponding to Simulation Example 3. This behavior can be explained as follows: The far-field patterns corresponding to phase modes 0 and 2 have low gains at the location of the second source. We have $J_0(\zeta_2) = -0.09$ and $J_2(\zeta_2) = -0.04$, where $\zeta_2 = 2\pi \sin\theta_2$. The output powers associated with the incident signals in two of the 13 available beams is therefore small. In contrast, the gain of these two beams is fairly large at the location of the first source: We have $J_0(\zeta_2) = -0.37$ and $J_2(\zeta_2) = 0.31$. This explains the fact that the theoretical analysis predicts higher UCA-ESPRIT estimator variances for the second source than for the first. The non-asymptotic behavior of the FB average is responsible for the fact that the experimental estimator performance for the second source (with K = 64 snapshots) is a little better than the theoretical (asymptotic) predictions.

Figure 5.6 depicts the UCA-ESPRIT eigenvalues $\hat{\mu}_i$ (marked by 'x's). The figure was formed by superimposing the results of 200 runs at an SNR of 10 dB. The true source locations are at the intersections of the dotted radial lines (azimuth angles) and the dotted circles (elevation angles).

5.6.3 Simulation Example 3

This simulation investigates the performance of the algorithms as a function of the phase of the correlation coefficient between the signals. The source locations are the same as in the previous example. The common source SNR is 7dB, and the magnitude of the correlation coefficient between the sources is 0.8. :Figure 5.7 depicts the performance of the DOA estimators as the phase of the correlation coefficient is varied from 0° to 180°. The behavior of the estimators (best performance at a correlation phase of 90°) is due to the FB average inherent in UCA-RB-MUSIC and UCA-ESPRIT. As a consequence of the FB average, the performance of the algorithms depends only on the real part, $\mathbf{P}_R$, of the source covariance matrix P. The off-diagonal elements of $\mathbf{P}_R$ are zero when the correlation phase is 90°, and the algorithms see the sources as effectively uncorrelated. The FB average in fact enables

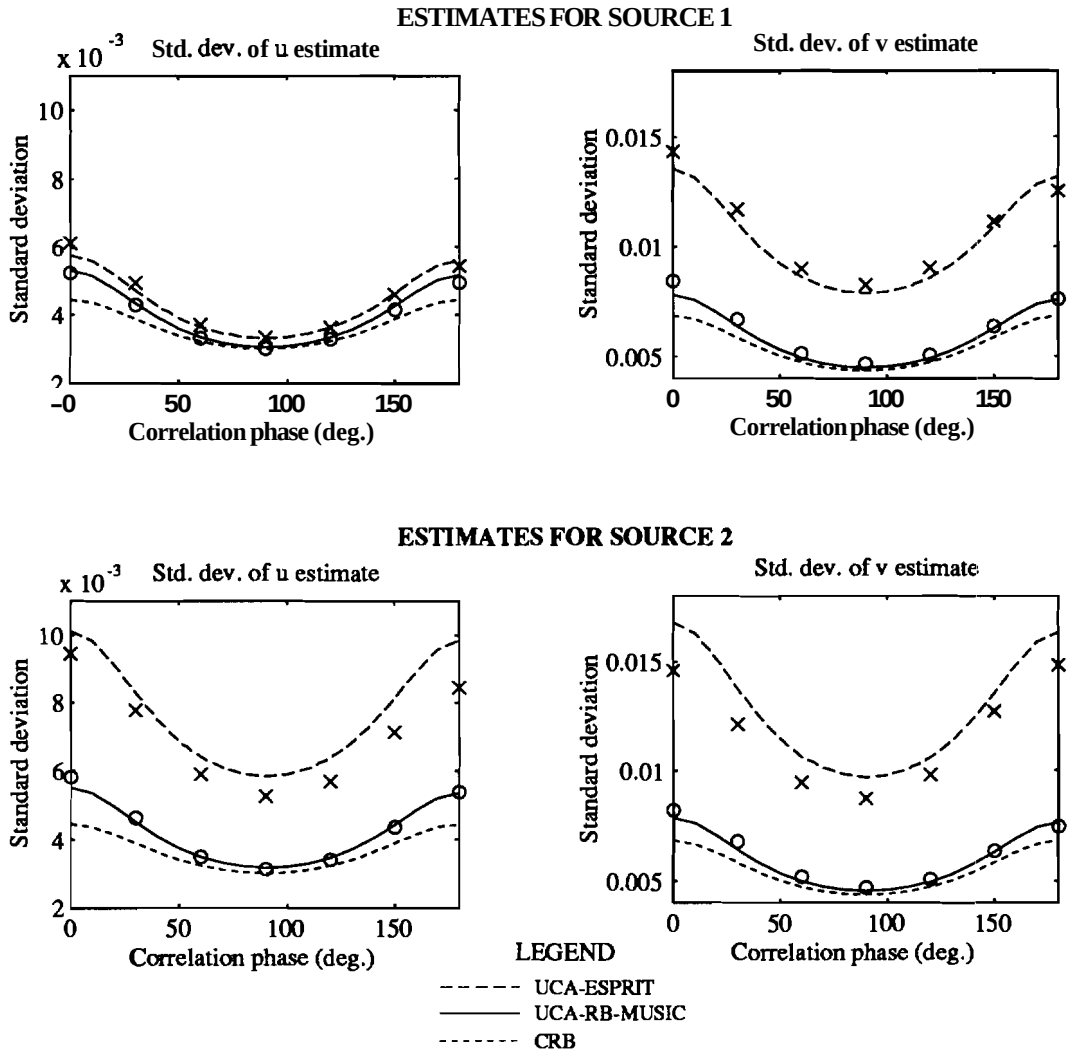

Figure 5.7 Performance of UCA-RB-MUSIC and UCA-ESPRIT as a function of the correlation coefficient phase.

UCA-RB-MUSIC and UCA-ESPRIT to resolve two coherent sources, provided the phase of the correlation coefficient is neither 0" nor 180°.

6. CONCLUSIONS

6.1 Summary of Results

Two signal subspace algorithms for 2D angle estimation with UCAs, UCA-RB-MUSIC and UCA-ESPRIT, have been developed. Both algorithms employ phase mode excitation based beamformers and operate in beamspace. UCA-RB-MUSIC is a beamspace version of MUSIC that offers the following advantages over element space MUSIC: ULA techniques such as FB averaging, Root-MUSIC, and Spatial smoothing can be employed in beamspace with the UCA. This is because the structure of the induced beamspace manifold is similar to the ULA manifold. The decorrelating effect of the inherent FB average allows UCA-RB-MUSIC to outperform element space MUSIC in correlated source scenarios when the number of array elements N is odd (FB type averaging is not possible in element space when N is odd). Finally, UCA-RB-MUSIC is more computationally efficient than element space MUSIC. This is because a real-valued EVD provides signal subspace estimates, ancl the FFT can be employed to facilitate the search for peaks in the beamspace MUSIC spectrum.

UCA-ESPRIT is a closed-form algorithm that provides automatically paired azimuth and elevation angle estimates for each source. It is the only. available closed-form algorithm for 2D angle estimation and thus represents a signiificant advance in the area. The eigenvalues of the matrix Ψ (derived from the least squares solution to an overdetermined system of equations) have the form $\mu_i = \sin\theta_i e^{j\phi_i} = u_i + jv_i$, and thus provide the properly associated DOA estimates. UCA-ESPRIT does not require expensive search procedures and is thus superior to existing 2D angle estimation algorithms with respect to computational complexity. Another factor that

reduces the computational load is that the implementation of UCA-ESPRI'T calls for only real-valued EVDs.

The effects of mutual coupling on the structure of the UCA element space manifold were analyzed. It was shown that the general structure of the original beamspace manifold is retained even when mutual coupling effects are present – the only difference is the introduction of gain and phase factors in the beamspace manifold. Consequently, minor modifications enable UCA-RB-MUSIC and UCA-ESPRIT to cope with mututal coupling effects. The properties of the UCA of directional elements were also studied. Both UCA-RB-MUSIC and UCA-ESPRIT are applicable if the individual element patterns are omnidirectional in azimuth. UCA-ESPRIT cannot be employed if this condition on element patterns is not met. However, a beamspace algorithm possessing many of the features of UCA-RB-MUSIC is still applicable.

The statistical performance of the element space MUSIC, UCA-RB-MUSIC, and UCA-ESPRIT algorithms for 2D angle estimation has been analyzed; asymptotic (large number of snapshots) expressions for the estimator variances/covariances have been derived. The analysis of element space MUSIC for 2D angle estimation holds for arbitrary array configurations. Prior to this work, the performance of MUSIC had been examined for only the 1D angle estimation problem. Closed-form expressions have been obtained for the element space MUSIC estimator variances in the one and two source scenarios. An investigation of the theoretical behavior of the element space MUSIC direction cosine estimator variances and the CRB has provided useful insights. In the single source case, both the element space MUSIC estimator variances and the CRB are constants (independent of the DOA). In the two source case, they depend only on the relative positions of the sources in the direction cosine space i.e., they depend only on the distance between the source locations and the orientation of the line joining the sources. The behavior of the UCA-RB-MUSIC estimator variances closely follows that of element space MUSIC and the CRB. The results of computer simulations that demonstrate the efficacy of UCA-RB-MUSIC and UCA-ESPRIT were presented. These results also validate the theoretical performance analysis; results.

6.2 Directions for Future Research

Two areas that merit further investigation are identified below. They concern the development of UCA-ESPRIT like algorithms for filled circular apertures/arrays and concentric ring arrays. We proceed to outline some ideas for accomplishing the above goals.

6.2.1 Adaptation of UCA-RB-MUSIC and UCA-ESPRIT for Filled Circular Arrays

Several existing phased array radar systems, e.g., the SPY-1A or SPY-1B radars in the AEGIS series [Sen88], and the arrays comprising the PAVE-PAWS surveillance network [Bro85], have circular apertures with antenna element locations specified by a hexagonal sampling lattice. Filled circular arrays also have potential application as base station antennas in mobile communications systems. The effort to adapt the UCA-RB-MUSIC and UCA-ESPRIT algorithms for filled circular arrays is thus relevant and significant. We proceed to discuss phase mode excitation (with a radial amplitude taper) of a circular disc aperture. The resulting far-field patterns are very similar to those of Section 3.3.1 for circular ring apertures. The UCA-RB-MUSIC and UCA-ESPRIT algorithms are thus easily adapted for use with filled circular apertures/arrays.

An excitation function corresponding to phase mode m for a circular disc aperture is

$$w_m(\rho,\gamma) = j^{-m}\left(\frac{\rho}{r}\right)^m e^{jm\gamma}, \quad \rho \in [0,r],\ \gamma \in [0,2\pi]. \qquad [6.1]$$

The term $e^{jm\gamma}$ (for integer m) excites the mth phase mode, $(\rho/r)^m$ is a mode dependent radial amplitude taper, and the phase factor j^{-m} ensures (as with the UCA) that the far-field mode amplitude is real-valued. The resulting far-field pattern is

$$\begin{aligned} f_m(\zeta,\phi) = f_m(k_o r\sin\theta,\phi) &= \frac{1}{2\pi}\int_0^R\int_0^{2\pi} w_m(\rho,\gamma) e^{jk_o\rho\sin\theta\cos(\phi-\gamma)}\,\rho\,d\rho\,d\gamma \\ &= \int_0^R (\rho/r)^m J_m(k_o\rho\sin\theta)\,e^{jm\phi}\,\rho\,d\rho \end{aligned}$$

$$= \left(\frac{r^2}{\zeta}\right) J_{m+1}(\zeta)\, e^{jm\phi}. \qquad [6.2]$$

The relationship $\int x^m J_m(x) = \mathrm{x}^{\mathrm{m}} J_{m+1}(x)$ was employed to obtain the final expression above. The far-field pattern above is similar to that of Equation **3.6** corresponding to phase mode excitation of a circular ring aperture. The differences are the increase in Bessel function order by one and the ζ dependence in the denominator. It is clear that a Real-Beamspace MUSIC algorithm similar to UCA-RB-MUSIC can be employed with a circular disc aperture. The UCA-ESPRIT principle can also be employed to develop a closed form 2D angle estimation algorithm with the circular disc aperture. A relationship between the far-field patterns corresponding to three successive phase modes can be developed by employing the recursive Bessel function property. The critical relationship is

$$\frac{\lambda}{\pi r}(m+1) f_m(\boldsymbol{\theta}) = \mu f_{m-1}(\boldsymbol{\theta}) + \mu^* f_{m+1}(\boldsymbol{\theta}), \qquad [6.3]$$

where $\mu = \sin\theta\, e^{j\phi}$. The development of the closed-form 2D angle estimation algorithm for the circular disc aperture now parallels the development of UCA-ESPRIT.

As was the case with UCAs, the far-field patterns of filled circular arrays closely follow the patterns of the circular disc apertures provided the interelement spacings are sufficiently small. Criteria need to be developed for locating array elements in a filled circular aperture such that the resulting patterns approximate those of continuous disc apertures. Possible sampling rasters include hexagonal, rectangular and polar. The efficacy of the versions of UCA-RB-MUSIC and UCA-ESPRIT for filled circular apertures needs to be evaluated. Comparisons can also be made between the performance of the algorithms for circular ring arrays and filled circular apertures.

6.2.2 Adaptation of UCA-ESPRIT for Concentric Ring Arrays

Concentric ring arrays have been employed for synthesis of directive patterns with low side-lobe levels [SS65]. We outline some ideas for extending the UCA-ESPRIT principle for concentric ring arrays (with two rings). The two concentric rings are assumed to have radii $r^{(i)}, i = 1, 2$. The spacing between the rings is denoted

$r_d = r^{(2)} - r^{(1)}$. $M' = 2M + 1$ phase modes are excited at each ring, as with the UCA. It is evident that the UCA-ESPRIT invariance principle can be independently applied to beam outputs of each ring. This yields twice as many equations compared with the single ring case; about twice as many sources can thus be resolved by the concentric ring array. The number of sources resolvable is easily verified to be $d_{max} = 2M - 1$, where M is the maximum mode excited. The number of sources resolvable with a single ring is $M - 1$.

UCA-ESPRIT relies on the recursive relationship between Bessel functions. Javier R. Lopez, who was a visiting scholar at Purdue University during the Fall of 1993, conceived the idea of employing another Bessel function property with concentric ring arrays. The property

$$J_{m-1}(\zeta) - J_{m+1}(\zeta) = 2J'_m(\zeta) \qquad [6.4]$$

relates Bessel functions and their derivatives. The idea was that the derivative could be approximated from the quantities associated with the two closely spaced rings. In the following, the superscript (i) will be employed to denote evaluation of a quantity at the ith ring e.g., $\zeta^{(2)} = k_0 r^{(2)} \sin\theta$ is just ζ evaluated at the second ring. The far-field pattern associated with phase mode m (neglecting the phase factor j^m) is $f_m^{(i)}(\theta) = J_m(\zeta^{(2)}) e^{jm\phi}$. Employing the relationship (6.4), it is easy to show that

$$e^{j\phi} f_{m-1}^{(1)}(\theta) - e^{-j\phi} f_{m+1}^{(1)}(\theta) = 2e^{jm\phi} J'_m(\zeta^{(1)}). \qquad [6.5]$$

The derivative can be approximated by

$$J'_m(\zeta^{(1)}) \approx \frac{e^{-jm\phi}[f_m^{(2)}(\theta) - f_m^{(1)}(\theta)]}{k_0 r_d \sin\theta}, \qquad [6.6]$$

provided the denominator $k_0 r_d \sin\theta$ is small. Combining Equations *6.5* and *6.6* leads to the relationship

$$\mu f_{m-1}^{(1)}(\theta) - \mu^* f_{m+1}^{(1)}(\theta) \approx \frac{2}{k_0 r_d}[f_m^{(2)}(\theta) - f_m^{(1)}(\theta)], \qquad [6.7]$$

where $\mu = \sin\theta e^{j\phi}$ as usual. This relationship provides another set of equations for the concentric ring array. More sources can be resolved by incorporating these

equations as well. The selection of the radial difference r_d is important, for the approximation of Equation 6.6 to be good. The denominator of this equation is $k_0 r_d \sin\theta = \frac{\zeta^{(2)} r_d}{r^{(2)}} \leq \frac{M r_d}{r^{(2)}}$. The final inequality above follows from Equation **3.7.** It is clear that r_d has to be a small fraction of the radius $r^{(2)}$ for the approximation in (6.6) to be accurate. This is a possible limitation of the method. Further investigation of the ideas proposed above is required.

BIBLIOGRAPHY

BIBLIOGRAPHY

[Bar83] A.J. Barabell. Improving the resolution performance of eigenstructure-based direction-finding algorithms. In Proc. IEEE *Int.* Conf. Acoust., Speech, Signal Processing, pages 336–339, 1983.

[BK84] G. Bienvenu and L. Kopp. Decreasing high resolution method sensitivity by conventional beamformer preprocessing. In Proc. IEEE *Int.* Conf. Acoust., Speech, Signal Processing, volume 2, pages 33.2.1–33.2.4, 1984.

[Bri81] D.R. Brillinger. Time Series: Data Analysis and Theory. Holden-Day, San Francisco, 1981.

[Bro85] E. Brookner. Phased array radars. Scientific *American*, pages 94–102, February 1985.

[CS91] M.P. Clark and L.L. Scharf. A maximum likelihood estimation technique for spatial-temporal modal analysis. In Proc. 25th *Annu.* Asilomar Conf. Signals, Syst., Comput., volume 1, pages 257–261, 1991.

[CZ69] R.E. Collin and F.J. Zucker, editors. Antenna Theory, volume 1, chapter 5. McGraw-Hill, New York, 1969.

[Dav65] D.E.N. Davies. A transformation between the phasing techniques required for linear and circular aerial arrays. Proc. IEE, 112(11):2041–2045, November 1965.

[Dav79] P.J. Davies. Circulant matrices. Wiley, New York, 1979.

[Dav83] D.E.N. Davies. The Handbook of Antenna Design, volume 2, chapter 12. A.W. Rudge, K. Milne, A.D. Olver, and P. Knight (Eds.), Peter Peregrinus, London, 1983.

[DD92] E. Doron and M. Doron. Coherent wideband array processing. In Proc. IEEE Int. Conf. Acoust., Speech, Signal Processing, volume 2, pages 497–500, 1992.

[FW91] B. Friedlander and A.J. Weiss. Direction finding in the presence of mutual coupling. IEEE Trans. Antennas Propagat., 39(3):273–284, March 1991.

[FW92] B. Friedlander and A.J. Weiss. Direction finding using spatial smoothing with interpolated arrays. IEEE Trans. Aerosp. Electron. Syst., 28(2):574–587, April 1992.

[GD83] J.R.F. Guy and D.E.N. Davies. UHF circular array incorporating open-loop null steering for communications. Proc. IEE, 130, pts. F and H(1):67–77, February 1983.

[Gup65] R.P. Gupta. Asymptotic theory for principal component analysis in the complex case. J. Indian Stat. Assoc., 3:97–106, 1965.

[Hay83] S.S. Haykin. Communication Systems. Wiley, New York, 1983.

[Hay85] S.S. Haykin. Array Signal Processing, chapter 4. S.S. Haykin Ed., Prentice-Hall, New Jersey, 1985.

[HS90] Y. Hua and T.K. Sarkar. Matrix pencil method for estimating parameters of exponentially damped undamped sinusoids in noise. IEEE Trans. Acoust., Speech, Signal Processing, 36(5):814–824, May 1990.

[Hua92] Y. Hua. Estimating two-dimensional frequencies by matrix enhancement and matrix pencil. IEEE Trans. on Signal Processing, 40(9):2267–2280, September 1992.

[JF85] D.J. Jeffries and D.R. Farrier. Asymptotic results for eigenvector methods. J. Indian Stat. Assoc., 132 pt. F(7):589–594, June 1985.

[KAR83] S.Y. Kung, K.S. Arun, and B.D. Rao. State-space and singular-value decomposition-based approximation methods for the harmonic retrieval problem. J. Opt. *Soc.* Amer., 73(12):1799–1811, December 1983.

[KB86] M. Kaveh and A.J. Barabell. The statistical performance of the MUSIC and minimum-norm algorithms in resolving plane waves in noise. IEEE Trans. Acoust., Speech, Signal Processing, 34:331–341, April 1986.

[KT82] R. Kumaresan and D.W. Tufts. Estimation of frequencies of multiple sinusoids: making linear prediction perform like maximum likelihood. Proc. IEEE, 70:975–989, September 1982.

[KT83] R. Kumaresan and D.W. Tufts. Estimating the angles of arrival of multiple plane waves. IEEE Trans. Aerosp. Electron. Syst., 19:134–139, January 1983.

[LCD67] I.D. Longstaff, P.E.K. Chow, and D.E.N. Davies. Directional properties of circular arrays. Proc. IEE, 114, June 1967.

[LV90] F. Li and R.J. Vaccaro. Unified analysis of DOA estimation algorithms in array signal processing. In 2nd *Int'l.* Workshop on SVD and Signal Processing, volume 25, pages 147–169, 1990.

[Ma74] M.T. Ma. Theory and Application of Antenna Arrays. Wiley, New York, 1974.

[MZ92] C.P. Mathews and M.D Zoltowski. Direction finding with circular arrays via phase mode excitation and Root-MUSIC. In Proc. IEEE AP-S Int. Symposium, volume 2, pages 1019–1022, 1992.

[MZ93a] C.P. Mathews and M.D. Zoltowski. Eigenstructure techniques for 2D angle estimation with uniform circular arrays. submitted *to* IEEE Trans. on Signal Processing, March 1993.

[MZ93b] C.P. Mathews and M.D. Zoltowski. Performance analysis of the UCA-ESPRIT algorithm for circular ring arrays. submitted to IEEE Trans. on Signal Processing, August 1993.

[OVK91] B. Ottersten, M. Viberg, and T. Kailath. Performance analysis of the total least squares ESPRIT algorithm. IEEE Trans. on Signal Processing, 39:1122–1135, May 1991.

[Pil89] S.U. Pillai. Array Signal Processing. Springer-Verlag, New York, 1989.

[Pis73] V.F. Pisarenko. The retrieval of harmonics from a covariance function. Geophys. J. Roy. Astronom. *Soc.*, 33:347–366, 1973.

[PK89a] S.U. Pillai and B.H. Kwon. Forward/backward spatial smoothing techniques for coherent signal identification. IEEE Trans. Acoust., Speech, Signal Processing, 37(1):8–15, January 1989.

[PK89b] S.U. Pillai and B.H. Kwon. Performance analysis of MUSIC-type high resolution estimators for direction finding in correlated and coherent scenes. IEEE Trans. Acoust., Speech, Signal Processing, 37(8):1176–1189, August 1989.

[PRK86] A. Paulraj, R. Roy, and T. Kailath. A subspace rotation approach to signal parameter estimation. Proc. IEEE, 74:1044–1045, July 1'986.

[RD82] T. Rahim and D.E.N. Davies. Effect of directional elements on the directional response of circular antenna arrays. Proc. IEE, 129, pt. H(1):180–22, February 1982.

[RH89a] B.D. Rao and K.V.S. Hari. Performance analysis of ESPRIT and TAM in determining the direction of arrival of plane waves in noise. IEEE Trans. Acoust., Speech, Signal Processing, 37(12):1990–1995, December 1989.

[RH89b] B.D. Rao and K.V.S. Hari. Performance analysis of Root-MUSIC. IEEE Trans. Acoust., Speech, Signal Processing, 37(12):1939–1949, December 1989.

[RK89] R. Roy and T. Kailath. ESPRIT-Estimation of signal parameters via rotational invariance techniques. IEEE Trans. Acoust., Speech, *Signal* Processing, 37(7):984–995, July 1989.

[RW92] C. Roller and W. Wasylkiwskyj. Effects of mutual coupling on super-resolution DF in linear arrays. In Proc. IEEE Int. Conf. Acoust., Speech, Signal Processing, volume 5, pages 257–260, 1992.

[Sch86] R.O. Schmidt. Multiple emitter location and signal parameter estimation. IEEE Trans. Antennas Propagat., 34(3):276–280, March 1986.

[Sen88] J. Sensi, Jr. The AEGIS System, chapter 3. E.Brookner (Ed.), Artech House, Boston, 1988.

[SK88] A.K. Shaw and R. Kumaresan. Some structured matrix approximation problems. In Proc. IEEE Int. Conf. Acoust., Speech, Signal Processing, volume 4, pages 2324–2327, 1988.

[SK93] A.L. Swindlehurst and T. Kailath. Azimuth/Elevation direction finding using regular array geometries. IEEE Trans. Aerosp. Electron. Syst., 29(1):145–156, January 1993.

[SN89] P. Stoica and A. Nehorai. MUSIC, Maximum likelihood and Cramer-Rao bound. IEEE Trans. Acoust., Speech, Signal Processing, 37(5):720–741, May 1989.

[SN90] P. Stoica and A. Nehorai. Performance study of conditional and unconditional direction-of-arrival estimation. IEEE Trans. Acoust., Speech, Signal Processing, 38(10):1783–1795, October 1990.

[SN91] P. Stoica and A. Nehorai. Comparative performance of elernent-space and beam-space MUSIC estimators. Circuits, Syst. and Signal Processing, 10(3):285–292, 1991.

[SS65] C.O. Stearns and A.C. Stewart. An investigation of concentric ring antennas with low sidelobes. IEEE Trans. Antennas Propagat., pages 856–863, November 1965.

[SS91] P. Stoica and T. Soderstrom. On spectral and root forms of sinusoidal frequency estimators. In Proc. IEEE Int. Conf. Acoust., *Speech,* Signal Processing, pages 3257–3260, 1991.

[Swi92] A. Swindlehurst. DOA identifiability for rotationally invariant arrays. IEEE Trans. Acoust., Speech, Signal Processing, 40(7):1825–1828, July 1992.

[SWK85] T.J. Shan, M. Wax, and T. Kailath. On spatial smoothing for estimation of coherent signals. IEEE Trans. Acoust., Speech, Signal Processing, 33:806–811, August 1985.

[TH92] A.H. Tewfik and W. Hong. On the application of uniform linear array bearing estimation techniques to uniform circular arrays. IEEE Trans. on Signal Processing, 40(4):1008–1011, April 1992.

[THN61] J.D. Tillman, C.E. Hickman, and H.P. Neff. The theory of a single ring circular array. Trans. Amer. *Inst. Electr.* Engrs., 80, pt. 1:110, 1961.

[VO91] M. Viberg and B. Ottersten. Sensor array processing based on subspace fitting. IEEE Trans. on Signal Processing, 39:1110–1121, May 1991.

[WK85] M. Wax and T. Kailath. Detection of signals by information theoretic criteria. IEEE Trans. Acoust., Speech, Signal Processing, pages 387–392, April 1985.

[YB92] S.F. Yau and Y. Bresler. A compact Cramer-Rao bound expression for parametric estimation of superimposed signals. IEEE Trans. on Signal Processing, 40(5):1226–1230, May 1992.

[ZK92] M.D. Zoltowski and G.M. Kautz. Performanceanalysis ofeigenstructure based DOA estimators employing conjugate centro-symmetric beamformers. In Proc. 6th SSAP Workshop on Statistical Signal *and* Array Processing, pages 384–387, October 1992.

[ZKS93] M.D. Zoltowski, G.M. Kautz, and S.D. Silverstein. Beamspace Root-MUSIC. IEEE Trans. on Signal Processing, 41(1):344–364, January 1993.

[ZM92] M.D. Zoltowski and C.P. Mathews. Direction finding with uniform circular arrays via phase mode excitation and Beamspace Root-MUSIC. In Proc. IEEE Int. Conf. Acoust., Speech, Signal Processing, volume 5, pages 245–248, 1992.

[ZS89] M.D. Zoltowski and D. Stavrinides. Sensor array signal. processing via a Procrustes rotations based eigenanalysis of the ESPRIT data pencil. IEEE Trans. Acoust., Speech, Signal Processing, 37(6):832–861, June 1989.

APPENDICES

Appendix A: Phase Mode Excitation of Circular Arrays/Apertures: Expressions for Far-Field Patterns

Expressions for the far-field patterns resulting from phase mode excitation of continuous circular apertures and uniform circular arrays are derived below. The expressions involve Bessel functions of the first kind. The integral representation of the Bessel function is useful: We have $J_m(x) = \frac{1}{2\pi}\int_0^{2\pi} e^{j(x\sin\theta - m\theta)}\,d\theta$. Making a simple substitution yields the following equivalent definition:

$$j^m J_m(x) = \frac{1}{2\pi}\int_0^{2\pi} e^{j(x\cos\theta + m\theta)}\,d\theta \qquad [A.1]$$

The above equation will be employed in the far-field pattern derivations below.

A.1 Far-Field Pattern for a Continuous Circular Aperture

The far-field pattern resulting from excitation of a continuous circular aperture with phase mode m is

$$f_m^c(\theta) = f_m^c(\zeta,\phi) = \frac{1}{2\pi}\int_0^{2\pi} e^{jm\gamma} e^{j\zeta\cos(\phi-\gamma)}\,d\gamma, \qquad [A.2]$$

where $\zeta = k_0 r \sin\theta$. Making the substitution $\gamma' = \gamma - \theta$ yields

$$f_m^c(\theta) = \frac{1}{2\pi}\int_0^{2\pi} e^{j[\zeta\cos\gamma' + m(\gamma'+\phi)]}\,d\gamma'.$$

The desired result $f_m^c(\theta) = j^m J_m(\zeta) e^{jm\phi}$ now follows from Equation A.1.

A.2 Far-Field Pattern for a Uniform Circular Array

The far-field pattern resulting from excitation of an N element UCA with phase mode m is

$$f_m^s(\theta) = f_m^s(\zeta,\phi) = \frac{1}{N}\sum_{n=0}^{N-1} e^{jm\gamma_n} e^{j\zeta\cos(\phi-\gamma_n)}, \qquad [A.3]$$

where $\gamma_n = 2\pi n/N$ specifies the array element locations. The summand in the above equation can be expressed as an integral using the sifting property of the delta function. We have

$$f_m^s(\theta) = \frac{1}{N}\sum_{n=0}^{N-1}\int_0^{2\pi} e^{jm\gamma} e^{j\zeta\cos(\phi-\gamma)}\delta(\gamma-\gamma_n)\,d\gamma = \int_0^{2\pi} e^{j[\zeta\cos(\phi-\gamma)+m\gamma]} g(\gamma)\,d\gamma, \qquad [A.4]$$

where $g(\gamma) = \frac{1}{N}\sum_{n=0}^{N-1}\delta(\gamma-\gamma_n)$ is an impulse train with impulses at the array element locations. The function $g(\gamma)$ is periodic with period $2\pi/N$ and can hence be expressed as a Fourier series. The Fourier series expansion for $g(\gamma)$ is

$$g(\gamma) = \frac{1}{2\pi}\sum_{q=-\infty}^{\infty} e^{jqN\gamma}.$$

Substituting in Equation A.4, we obtain

$$f_m^s(\boldsymbol{\theta}) = \sum_{q=-\infty}^{\infty}\frac{1}{2\pi}\int_0^{2\pi} e^{j[\zeta\cos(\phi-\gamma)+(m+qN)\gamma]}\,d\gamma.$$

The integral above is similar to that in Equation A.2. As before, making the substitution $\gamma' = \gamma - \phi$ yields

$$\begin{aligned} f_m^s(\boldsymbol{\theta}) &= \sum_{q=-\infty}^{\infty} j^{m+qN}J_{m+qN}(\zeta)e^{j(m+qN)\phi} \\ &= j^m J_m(\zeta)e^{jm\phi} + \sum_{q=-\infty,q\neq 0}^{\infty} j^{m+qN}J_{m+qN}(\zeta)e^{j(m+qN)\phi} \end{aligned}$$

The terms above corresponding to negative values of q can be grouped into a separate infinite summation. When the mode order m is positive and satisfies $m < N$, these terms give rise to Bessel functions of negative orders. Employing the property $J_{-m}(\zeta) = (-1)^m J_m(\zeta)$ of Bessel functions yields the desired result

$$f_m^s(\boldsymbol{\theta}) = j^m J_m(\zeta)e^{jm\phi} + \sum_{q=1}^{\infty}\left(j^g J_g(\zeta)e^{-jg\phi} + j^h J_h(\zeta)e^{jh\phi}\right), \qquad [A.5]$$

where $g = Nq - m$ and $h = Nq + m$. It is easy to see that the expression above holds even when the mode order m is negative and satisfies $|m| < N$. The expression for the UCA far-field pattern above is thus valid for mode orders $|m| < N$. We note that for a UCA of N elements, all phase mode orders $m + kN$, for arbitrary integers k, are identical. This is easily seen from Equation 3.8.

Appendix B: Phase Mode Excitation Based Pattern Synthesis for UCAs

Phase mode excitation can be employed to synthesize attractive directional patterns for UCAs as described below. The UCA far-field pattern $f(\theta,\$)$ is a function of the elevation 8, and the azimuth ϕ. The azimuthal pattern corresponding to a given elevation angle 8 is denoted $f(\phi;8)$. Phase mode excitation caa be employed to synthesize a desirable azimuthal pattern $f(\phi;8)$ at a given elevation 8. The synthesized pattern $f(\phi;\theta)$ could be real-valued; this leads to a reduction in computational complexity of the Beamspace MUSIC aalgorithm as described in Section **2.6.2.** The far-field patterns $f(\phi;8)$ synthesized via phase mode excitation are trigonometric polynomials in ϕ. This allows Root-MUSIC to be employed to perform the search in azimuth for sources at a given elevation as discussed in Section 4.2.1.

Given the parameters k_0 and r, the maximum mode M and the: number of array elements N are chosen according to the guidelines of Sections **3.3.1** and **3.3.2.** We will assume that M and N are chosen such that the UCA far-field patterns corresponding to modes m $\in [-M,M]$ are given by Equation **3.12.** The beamforming weight vector $\mathbf{w}_m^H$ of Equation **3.8** excites the UCA with phase mode m. For pattern synthesis with the UCA, all the modes m $\in [-M, M]$ are simultaneously excited, with the excitation coefficient for mode m being c_m. The beamforming weight vector employed is thus

$$\mathbf{w}^H = \sum_{m=-M}^{M} c_m \mathbf{w}_m^H. \qquad \text{[B.1]}$$

From Equation **3.12** we see that the resulting far-field pattern is

$$f(\theta,\phi) \approx \sum_{m=-M}^{M} c_m j^{|m|} J_{|m|}(k_0 r \sin\theta) e^{jm\phi} = k_m(\theta) e^{jm\phi}, \qquad \text{[B.2]}$$

where $k_m(\theta) = c_m j^{|m|} J_{|m|}(k_0 r \sin\theta)$. The pattern $f(\phi;8)$ at the elevation θ is a trigonometric polynomial. The desired pattern $f(\phi;8)$ is synthesized by appropriate choice of the coefficients $k_m(\theta)$ of the trigonometric polynomial. The excitation coefficients c_m are chosen to provide the desired values of $k_m(\theta)$. It is clear from Equation **B.2** that the entire pattern is real-valued if $c_{-m} = c_m$ (this makes $k_{-m}(\theta) = k_m(\theta)$).

The example below illustrates sinc-type azimuthal pattern synthesis for the UCA in the array plane (elevation $0 = \pi/2$). Synthesis of sinc-type patterns (similar to ULA far-field patterns) with UCAs was considered by Davies in [Dav83]. In practice, sinc-type patterns are not very useful because of the high side-lobe levels. The pattern synthesis procedure can however be employed to synthesize attractive patterns with low side-lobe levels. For sinc-type pattern azimuthal pattern synthesis at $\theta = \pi/2$, the required excitation coefficients are $c_m = 1/j^{|m|}J_{|m|}(k_0 r)$. This yields $k_m(\theta) = J_{|m|}(k_0 r \sin\theta)/J_{|m|}(k_0 r)$, and we have $k_m(\pi/2) = 1$ for all m. From Equation B.2 we see that the azimuthal pattern in the array plane

$$\mathrm{f}(\phi;\pi/2) = \sum_{\mathrm{m}=-\mathrm{M}}^{\mathrm{M}} e^{jm\phi} = \frac{\sin(2M+1)\phi/2}{\sin\phi/2} \qquad [\mathrm{B.3}]$$

has the desired sinc-type structure. The shape of the azimuthal pattern at other elevation angles is determined by the coefficients $k_m(\theta)$; these patterns will not be sinc shaped. We note that although the sinc-type pattern $\mathrm{f}(\phi;\pi/2)$ above has its maximum at $\phi = 0$, the maximum array gain may occur at an elevation other than $\pi/2$. This is not the case with cophasal excitation, where the maximum gain is always in the 'look' direction.

The mechanism for synthesizing a desired azimuthal pattern at a given elevation was described above. To employ beamspace MUSIC, multiple beam outputs are required. Multiple beam outputs are typically obtained by rotating the entire pattern $\mathrm{f}(\theta,\phi)$ in azimuth. It is clear from Equation B.2 that replacing c_m by $c_m e^{-jm\alpha}$ achieves the desired pattern rotation: the corresponding pattern is $\mathrm{f}(0,\phi-\mathrm{a})$. The matrix W of Equation 4.10 provides pattern rotation for the UCA-RB-MUSIC algorithm. It generates the $M' = 2\mathrm{M}+1$ beams $\mathrm{f}(\zeta,\phi-\mathrm{a};)$ by rotating the basic beam-pattern $\mathrm{f}(\zeta,4)$ in azimuth by the angles $\mathrm{a};=2\pi i/M'$, $i \in [-\mathrm{M},M]$.

Our initial research efforts [ZM92, MZ92] focused on applying ULA techniques with UCAs. Sinc-type pattern synthesis as described above, and the use of Root-MUSIC to perform the azimuthal search at a given elevation were proposed.

Appendix C: Properties of UCA-ESPRIT

C.1 Block Conjugate Structure of the LS Solution

Consider first the noise free case, where the true signal subspace matrices are available. Assume that the least squares solution to Equation 4.34 is $\underline{\boldsymbol{\Psi}} = [\boldsymbol{\Psi}_1^T \vdots \boldsymbol{\Psi}_2^T]^T$. The LS solution is obtained by solving the system $\mathbf{E}^H\mathbf{E}\underline{\boldsymbol{\Psi}} = \mathbf{E}^H\boldsymbol{\Gamma}\mathbf{S}_0$. Substituting for $\mathbf{E}$ from (4.34), this system can be expanded as follows:

$$\begin{bmatrix} \mathbf{S}_{-1}^H \\ \mathbf{S}_{-1}^T\mathbf{D}\tilde{\mathbf{I}} \end{bmatrix} \left[\mathbf{S}_{-1} \vdots \mathbf{D}\tilde{\mathbf{I}}\mathbf{S}_{-1}^*\right] \begin{bmatrix} \boldsymbol{\Psi}_1 \\ \boldsymbol{\Psi}_2 \end{bmatrix} = \begin{bmatrix} \mathbf{S}_{-1}^H \\ \mathbf{S}_{-1}^T\mathbf{D}\tilde{\mathbf{I}} \end{bmatrix} \boldsymbol{\Gamma}\mathbf{S}_0. \qquad [C.1]$$

Equating the upper and lower blocks of the above equation, we obtain

$$\mathbf{S}_{-1}^H[\mathbf{S}_{-1}\boldsymbol{\Psi}_1 + \mathbf{D}\tilde{\mathbf{I}}\mathbf{S}_{-1}^*\boldsymbol{\Psi}_2] = \mathbf{S}_1^H\boldsymbol{\Gamma}\mathbf{S}_0, \text{ and} \qquad [C.2]$$

$$\mathbf{S}_{-1}^T[\mathbf{D}\tilde{\mathbf{I}}\mathbf{S}_{-1}\boldsymbol{\Psi}_1 + \mathbf{S}_{-1}^*\boldsymbol{\Psi}_2] = \mathbf{S}_{-1}^T\mathbf{D}\tilde{\mathbf{I}}\boldsymbol{\Gamma}\mathbf{S}_0 = \mathbf{S}_{-1}^T\boldsymbol{\Gamma}\mathbf{S}_0^*. \qquad [C.3]$$

The property $\mathbf{D}\tilde{\mathbf{I}}\boldsymbol{\Gamma}\mathbf{S}_0 = \boldsymbol{\Gamma}\mathbf{S}_0^*$ that was used in the final equality above can be established by multiplying Equation 4.33 by $\mathbf{D}\tilde{\mathbf{I}}$. Now, the right hand sides of Equations C.2 and C.3 are conjugates, and the left hand sides are therefore conjugates as well. We thus have $\boldsymbol{\Psi}_2 = \boldsymbol{\Psi}_1^*$, and the LS solution $\underline{\boldsymbol{\Psi}}$ has block conjugate structure as expected.

All that is required for the proof to carry over to the case where signal subspace estimates are employed is to show that $\mathbf{D}\tilde{\mathbf{I}}\boldsymbol{\Gamma}\hat{\mathbf{S}}_0 = \boldsymbol{\Gamma}\hat{\mathbf{S}}_0^*$. This relationship was shown to hold in the noise free case: We have $\mathbf{D}\tilde{\mathbf{I}}_{M_e}\boldsymbol{\Gamma}\mathbf{S}_0 = \boldsymbol{\Gamma}\mathbf{S}_0^*$. The subscript M_e denotes the dimension of the reverse permutation matrix. Substituting $\mathbf{S}_0 = \boldsymbol{\Delta}_0\mathbf{C}_o\mathbf{W}\mathbf{S}$ and using the property $\tilde{\mathbf{I}}_{M'}\mathbf{W} = \mathbf{W}^*$ and the fact that $\mathbf{S}$ is real-valued establishes the following: $\mathbf{D}\tilde{\mathbf{I}}_{M_e}\boldsymbol{\Gamma}\boldsymbol{\Delta}_0\mathbf{C}_o = \boldsymbol{\Gamma}\boldsymbol{\Delta}_0\mathbf{C}_o\tilde{\mathbf{I}}_{M'}$. This property is used in the following sequence of manipulations which complete the proof for the case where signal subspace estimates are employed.

$$\begin{aligned} \mathbf{D}\tilde{\mathbf{I}}_{M_e}\boldsymbol{\Gamma}\hat{\mathbf{S}}_0 &= \mathbf{D}\tilde{\mathbf{I}}_{M_e}\boldsymbol{\Gamma}\boldsymbol{\Delta}_0\mathbf{C}_o\mathbf{W}\hat{\mathbf{S}} = \boldsymbol{\Gamma}\boldsymbol{\Delta}_0\mathbf{C}_o\tilde{\mathbf{I}}_{M'}\mathbf{W}\hat{\mathbf{S}} \\ &= \boldsymbol{\Gamma}\boldsymbol{\Delta}_0\mathbf{C}_o\mathbf{W}^*\hat{\mathbf{S}} = \boldsymbol{\Gamma}\hat{\mathbf{S}}_0^*. \end{aligned}$$

We now have $\hat{\Psi}_1 = \hat{\Psi}_2^* = \hat{\Psi}$, and Equation C.2 (written in terms of estimated quantities) thus uniquely specifies the LS solution. The LS solution $\hat{\Psi}$ is obtained by solving the following d × d complex-valued system of equations:

$$\mathbf{B}\hat{\Psi} + \mathbf{C}\hat{\Psi}^* = \mathrm{Q}, \text{ where}$$

$$\mathrm{B} = \hat{\mathbf{S}}_{-1}^H \hat{\mathbf{S}}_{-1}, \mathrm{C} = \hat{\mathbf{S}}_{-1}^H \mathbf{D}\tilde{\mathbf{I}}\hat{\mathbf{S}}_{-1}^*, \text{ and } \mathbf{Q} = \hat{\mathbf{S}}_{-1}^H \mathbf{\Gamma}\hat{\mathbf{S}}_0.$$

Writing in terms of the real and imaginary parts shows that $\hat{\Psi}$ can be obtained by solving the 2d x 2d real-valued system of Equation 4.36.

C.2 **Failure** of UCA-ESPRIT **when** d ≥ M

The system $\hat{\mathbf{E}}\underline{\hat{\Psi}} = \mathbf{\Gamma}\hat{\mathbf{S}}_0$ is underdetermined, and has an infinity of solutions $\underline{\hat{\Psi}}$ when the number of sources d ≥ M. Following the procedure employed in the previous proof, the minimum norm solution $\underline{\hat{\Psi}}_{min} = \hat{\mathbf{E}}^H(\hat{\mathbf{E}}\hat{\mathbf{E}}^H)^{-1}\mathbf{\Gamma}\hat{\mathbf{S}}_0$ can be shown to have block conjugate structure. We now proceed to show that $\eta(\hat{\mathbf{E}}) = \eta(\hat{\mathbf{E}}^H\hat{\mathbf{E}})$ is spanned by block conjugate vectors. Linear combinations of these vectors can be! added to $\underline{\hat{\Psi}}_{min}$ without destroying the block conjugate structure. There is thus no unique block conjugate solution to Equation 4.35 when d ≥ M.

The 2d × 2d matrix E' = $\hat{\mathbf{E}}^H\hat{\mathbf{E}}$ can be written in block form as follows: E' = $\begin{bmatrix} \mathbf{B} & \mathbf{C} \\ \mathbf{C}^* & \mathbf{B}^* \end{bmatrix}$, where B and C are as defined in Equation 4.37. Let $\mathbf{z} = [\mathbf{z}_1^T : \mathbf{z}_2^T]^T$ be a vector in $\eta(\mathbf{E}')$. Setting $\mathbf{E}'\mathbf{z} = \mathbf{0}$ leads to the two equations below:

$$\mathbf{B}\mathbf{z}_1 + \mathbf{C}\mathbf{z}_2 = \mathbf{0}, \text{ and} \qquad [C.4]$$

$$\mathbf{C}^*\mathbf{z}_1 + \mathbf{B}^*\mathbf{z}_2 = \mathbf{0}. \qquad [C.5]$$

Forming (C.4) + (C.5)* and (C.4)* + (C.5) leads to the system

$$\begin{bmatrix} \mathbf{B} & \mathbf{C} \\ \mathbf{C}^* & \mathbf{B}^* \end{bmatrix} \begin{bmatrix} \mathbf{z}_1 + \mathbf{z}_2^* \\ \mathbf{z}_2 + \mathbf{z}_1^* \end{bmatrix} = \mathbf{0}.$$

This system shows that there is a block conjugate vector in $\eta(\mathbf{E}')$ corresponding to the vector $\mathbf{z} \in \eta(\mathbf{E}')$. Thus $\eta(\mathbf{E}') = \eta(\hat{\mathbf{E}})$ can be spanned by block conjugate vectors, and the proof is complete.

Appendix D: Study of Theoretical Estimator Performance

The following easily proved relationships are employed in obtaining expressions for the variances of the element space MUSIC estimators. For brevity, the dependence of the manifold vectors on the DOA is not always shown i.e., $\underline{\mathbf{a}}$ is used in place of $\underline{\mathbf{a}}(\boldsymbol{\beta})$.

$$\begin{aligned} \underline{\mathbf{a}}_u &= \mathbf{D_c}\,\underline{\mathbf{a}}, \text{ and } \underline{\mathbf{a}}_v = \mathbf{D_s}\,\underline{\mathbf{a}}, \text{ where} \\ \mathbf{D_c} &= (jk_0r)\,\mathrm{diag}\{\cos\gamma_0, \ldots, \cos\gamma_{N-1}\}, \text{ and} \\ \mathbf{D_s} &= (jk_0r)\,\mathrm{diag}\{\sin\gamma_0, \ldots, \sin\gamma_{N-1}\}. \end{aligned} \quad [D.1]$$

In the definitions above, $\gamma_i = 2\pi i/N$ is the angular location of the ith antenna element. The following relationships can be established using the above equations:

$$\begin{aligned} \underline{\mathbf{a}}^H\underline{\mathbf{a}}_u &= \underline{\mathbf{a}}^H\underline{\mathbf{a}}_v = 0 \\ \underline{\mathbf{a}}_u^H\underline{\mathbf{a}}_u &= \underline{\mathbf{a}}_v^H\underline{\mathbf{a}}_v = \frac{N(k_0r)^2}{2} \end{aligned} \quad [D.2]$$

Consider the two source locations $\boldsymbol{\beta}_1 = (u_1, v_1)$ and $\boldsymbol{\beta}_2 = (u_2, v_2)$. Let $\boldsymbol{\beta}_d = (u_d, v_d)$ where $u_d = u_2 - u_1$ and $v_d = v_2 - v_1$. The representation of $\boldsymbol{\beta}_d$ in polar coordinates is (τ, u), where $\tau = \sqrt{u_d^2 + v_d^2}$ and $\nu = \tan^{-1}(v_d/u_d)$. The relationship below states that the UCA cophasal beam pattern approximately follows the Bessel function J_0. The relationship is accurate for our purposes because the residual contributions have been made negligible by appropriate choice of N. We have

$$\underline{\mathbf{a}}^H(\boldsymbol{\beta}_1)\underline{\mathbf{a}}(\boldsymbol{\beta}_2) \approx NJ_0(k_0r\tau), \quad [D.3]$$

and the array gain depends only on the distance τ between the locations $\boldsymbol{\beta}_1$ and $\boldsymbol{\beta}_2$. The final relationships to be established are

$$\underline{\mathbf{a}}^H(\boldsymbol{\beta}_1)\underline{\mathbf{a}}_u(\boldsymbol{\beta}_2) \approx -k_0rNJ_1(k_0r\tau)\cos\nu = -\underline{\mathbf{a}}^H(\boldsymbol{\beta}_2)\underline{\mathbf{a}}_u(\boldsymbol{\beta}_1), \text{ and} \quad [D.4]$$

$$\underline{\mathbf{a}}^H(\boldsymbol{\beta}_1)\underline{\mathbf{a}}_v(\boldsymbol{\beta}_2) \approx -k_0rNJ_1(k_0r\tau)\sin\nu = -\underline{\mathbf{a}}^H(\boldsymbol{\beta}_2)\underline{\mathbf{a}}_v(\boldsymbol{\beta}_1). \quad [D.5]$$

An outline of the proof of Equation D.4 is provided below. Equation D.5 can be proved in similar fashion. Using the results in (D.1), we can write $\underline{\mathbf{a}}^H(\boldsymbol{\beta}_1)\underline{\mathbf{a}}_u(\boldsymbol{\beta}_2) =$

$\sum_{n=1}^{N} jk_0 r \cos\gamma_n \, e^{jk_0 r(u_d \cos\gamma_n + v_d \sin\gamma_n)}$. The summation of the exponential terms alone is just the cophasal beampattern of Equation ***D.3.*** The partial derivative of the cophasal pattern with respect to u_d, $\frac{\partial}{\partial u_d} N J_0\left(k_0 r\sqrt{u_d^2 + v_d^2}\right)$, thus evaluates the entire summation. Simplifying and using the property $J_0' = -J_1$ yields the desired result.

D.1 *Element Space MUSIC Estimator Variances*

Expressions for the element space MUSIC estimator variances and covariance are given in Theorem ***5.1.1.*** The variance expressions are in terms of the quantities $\underline{a} = \underline{\mathbf{a}}_u^H \underline{\mathbf{G}}\underline{\mathbf{G}}^H \underline{\mathbf{a}}_u$, $\underline{b} = \underline{\mathbf{a}}_v^H \underline{\mathbf{G}}\underline{\mathbf{G}}^H \underline{\mathbf{a}}_v$ and $\underline{c} = \mathrm{Re}\{\underline{\mathbf{a}}_v^H \underline{\mathbf{G}}\underline{\mathbf{G}}^H \underline{\mathbf{a}}_u\}$. The projection matrix onto the noise subspace can be expressed in terms of the ***DOA*** matrix as follows: $\underline{\mathbf{G}}\underline{\mathbf{G}}^H = I - \underline{\mathbf{A}}\left(\underline{\mathbf{A}}^H \underline{\mathbf{A}}\right)^{-1} \underline{\mathbf{A}}^H$.

Single Source *Case*

For the single source case, we have $\underline{\mathbf{A}} = \underline{\mathbf{a}}$. Using Equation ***D.2,*** we obtain $\underline{a} = \underline{b} = (k_0 r)^2 N/2$ and $\underline{c} = 0$. Substituting the source power p in place of P in Equation ***5.4,*** we find that $\sigma_{\hat{p}} = (1 + 1/N)/(p/\sigma)$. Substituting these results in Theorem ***5.1.1*** yields

$$\begin{aligned} \mathrm{Var}\,(2) = \mathrm{Var}\,(\hat{v}) &= \frac{1 + 1/N}{KN(k_0 r)^2 (p/\sigma)}, \text{ and} \\ \mathrm{Cov}\,(\hat{u}, \hat{v}) &= 0. \end{aligned}$$

Two Source *Case*

Let $\boldsymbol{Q} = (\underline{\mathbf{A}}^H \underline{\mathbf{A}})^{-1}$. Using the result of Equation ***D.3, Q*** can be expressed as follows:

$$\mathbf{Q} = \begin{bmatrix} q & qJ_0(k_0 r\tau) \\ qJ_0(k_0 r\tau) & q \end{bmatrix}, \text{ where} \qquad [D.6]$$

$$q = \frac{1}{N[1 - J_0^2(k_0 r\tau)]}.$$

The simplified expression for $\underline{a}$ in Equation **5.25** is derived below. Expressions for $\underline{b}$ and $\underline{c}$ can be obtained in similar fashion. We have

$$\begin{aligned} \underline{a}(\beta_1) &= \underline{\mathbf{a}}_u^H(\beta_1)[\mathbf{I} - \underline{\mathbf{A}}\mathbf{Q}\underline{\mathbf{A}}^H]\underline{\mathbf{a}}_u(\beta_1) \\ &= N(k_0 r)^2/2 - \left(\underline{\mathbf{a}}_u^H(\beta_1)\underline{\mathbf{A}}\right)\mathbf{Q}\left(\underline{\mathbf{A}}^H\underline{\mathbf{a}}_u(\beta_1)\right) \end{aligned} \qquad [D.7]$$

Using Equations D.2 and D.4, we obtain $\underline{\mathbf{A}}^H\underline{\mathbf{a}}_u(\beta_1) \approx [0 \vdots k_0 r N J_1(k_0 r\tau)\cos\nu]^T$. Substituting in Equation D.7 yields the desired expression

$$\underline{a}(\beta_1) \approx (k_0 r)^2\left[\frac{N}{2} - q\{NJ_1(k_0 r\tau)\cos\nu\}^2\right]. \qquad [D.8]$$

Finally, Equation **5.4** shows that the dependence of $\underline{\rho}$ on the source DOAs is only through the matrix $\mathbf{Q} = (\underline{\mathbf{A}}^H\underline{\mathbf{A}})^{-1}$. It is evident from Equation D.6 that $\mathbf{Q}$ and thus $\underline{\rho}$ depends only on the distance τ

D.2 The Deterministic CRB

From Lemma **5.4.1** it is clear that the dependence of the deterministic CRB on the source DOAs is through the matrix H. We proceed to show that the CRBs are independent of the DOA in the single source case. We also show that the CRBs depend on the source DOAs only through the parameters τ and ν in the two source case.

Single Source Case

Substituting $\underline{\mathbf{a}}$ in place of $\underline{\mathbf{A}}$ in Equation **5.22** and using the results of Equation D.2 yields $\mathrm{H} = \frac{N(k_0 r)^2}{2}\mathbf{I}$. Further, all the elements of the matrix $\mathbf{P}_+$ are identical and equal to the source power **p.** Substituting these results in Equation **5.22** yields the CRB covariance matrix

$$\mathrm{CRB}\,(\hat{u},\hat{v}) = \frac{1}{KN(k_0 r)^2(p/\sigma)}\mathbf{I}.$$

Two Source Case

We have $\mathrm{H} = \mathbf{D}^{\mathrm{H}}\mathbf{D} - \mathbf{D}^H\underline{\mathbf{A}}\mathbf{Q}\underline{\mathbf{A}}^H\mathbf{D}$. The entries of the second matrix in this expression have forms similar to the second term in Equation D.7, and thus depend

only on r and v. The entries of the first matrix $D^H D$ have the form $\underline{\mathbf{a}}_x^H(\boldsymbol{\beta}_i)\underline{\mathbf{a}}_y(\boldsymbol{\beta}_j)$ where x and y could be either u or v, and $i, j \in [1,2]$. Expressions for these terms can be obtained by taking partial derivatives of the cophasal beampattern with respect to u_d and v_d as in the proof of Equation D.4. These terms can also be shown to depend only on τ and v. Thus the matrix H depends on the source DOAs only through τ and ν, and so does the CRB covariance matrix.